Two-dimensional measurements of electronic and ionic processes on silicon surface

Thesis

Kan Nakatsuji

OSAKA UNIVERSITY
GRADUATE SCHOOL OF ENGINEERING SCIENCE
DEPARTMENT OF PHYSICAL SCIENCE
DIVISION OF MATERIALS PHYSICS

1998

Two-dimensional measurements of electronic and ionic processes on silicon surface

Thesis

Kan Nakatsuji

Division of Materials Physics
Department of Physical Science
Graduate School of Engineering Science
Osaka University

January 23, 1998

Abstract

Recent development of display-type spherical mirror analyzer has made it possible to obtain the angular distribution of charged particles emitted from solid surface, which means that two-dimensional measurement of photoelectrons or ions has become practical. In this thesis, two-dimensional measurement has been demonstrated to be effective in investigation of surface science through the studies of three topics on electronic and ionic processes as follows.

In the study of circular dichroism in angular distribution of the photoelectron from Si(001) valence band using circularly-polarized synchrotron radiation at final state energies of 40, 80 and 250eV, all of the obtained photoelectron angular distribution showed apparent circular dichroism in angular distribution. At the final state energy of 40eV, the observed photoelectron angular distribution was understood in terms of one-dimensional density of state, photoemission structure factor and matrix element of the direct transition from the initial state atomic orbital to the free electron-like final state. The origin of circular dichroism in angular distribution of the photoelectron was dominated by the interference of the final state waves in lower binding energies. Comparing obtained photoelectron angular distribution with the distribution of matrix element, we distinguished contributions from $3p_x$ and $3p_y$ orbitals. This suggests a possibility that circular dichroism in angular distribution of the photoelectron provides a new way to determine the initial state symmetry by virtue of the different selection rules in transition from those in the excitation by linearly polarized light. The photoelectron angular distribution patterns strongly depend on the final state energy. At the final state energy of 250eV, photoelectron diffraction effect becomes apparent although some contributions from one-dimensional density of state still exist. At 250eV, the origin of circular dichroism in angular distribution is explained by the rotation of forward focusing peaks, which is the same as those in the case of core level photoemission.

In the study of surface states on Si(111)-($\sqrt{3} \times \sqrt{3}$)R30° -Ag surface, the obtained photoelectron angular distributions showed mirror symmetry, which correspond to the surface atomic structure of well known honeycomb chained trimer model. Some surface states observed between Fermi level and the binding energy of 1.7eV are in reasonable agreement with a previous report of one-dimensional angle-resolved photoelectron spectroscopy. Comparing the photoelectron intensity angular distribution with the calculated matrix element for the linearly polarized light, we have confirmed the initial state characters of these surface states. A metallic surface state was revealed to be *in-plane* Ag $5p$ orbital. The characters of the other resonances were confirmed to be p_z or s and *in-plane* p orbitals.

In the study of adsorption and desorption processes of Cl on Si(001) and (111) surfaces by electron stimulated desorption and laser induced ion desorption, the adsorption behavior of Cl showed an influence of interaction among the created surface dipoles, especially on the (001) surface. The angular distribution of the desorbed ion indicated the adsorption at the dangling bond and bridge sites on the (001) surface. The desorption mechanism of Cl^+ was revealed to be an Auger stimulated process via the excitation of the Cl $3s$ and $2p$ core hole. Furthermore, a strong evidence was found for the discrete surface dipole model from the kinetic energy distribution of desorbed ions.

Acronyms

AES	Auger electron spectroscopy
ARIPES	angle-resolved inverse photoemission spectroscopy
ARPES	angle-resolved photoelectron spectroscopy
ARUPS	angle-resolved ultra-violet photoelectron spectroscopy
ASID (ASD)	Auger stimulated ion desorption
BZ	Brillouin zone
CCW	counterclockwise
CDAD	circular dichroism in angular distribution
CFS	constant final state spectroscopy
CW	clockwise
DIET	desorption induced by electronic transition
EELS	electron energy loss spectroscopy
E_f	energy of the final state
ESD	electron stimulated desorption
ESDIAD	electron stimulated desorption ion angular distribution
EXAFS	extended X-ray absorption fine structure
LCAO	linear combination of atomic orbitals
LCP	left circularly polarized (light)
LEED	low energy electron diffraction
LID	laser induced (ion) desorption
MCP	multi-channel plate
ML	mono-layer
1D-DOS	one-dimensional density of state
PEAD	photoelectron angular distribution
PES	photoelectron spectroscopy
PSD	photon stimulated desorption
RCP	right circularly polarized (light)
SBZ	surface Brillouin zone
SR	synchrotron radiation
STM	scanning tunneling microscopy
2D	two-dimensional
TOF	time of flight
UHV	ultra high vacuum
UPS	ultra-violet photoelectron spectroscopy
VBM	valence band maximum
XESD	X-ray induced electron stimulated desorption
XPS	X-ray photoelectron spectroscopy

Contents

Chapter 1

Introduction

1.1 Preface

Investigation of solid surface has been an important part in condensed matter physics for the past thirty years, and made rapid progress with development of vacuum technology. Solid surface has different characters from those of bulk because of two-dimensional (2D) periodicity, which leads to an appearance of new type phenomena localized at the surface. Silicon surface has attracted much attention as a typical semiconductor surface and has been extensively investigated[1]. It is generally known that the atoms in the surface layer change their positions to realize lower free energy of the system, which is so-called "surface reconstruction". Especially, the semiconductor surface such as Si surface is unstabilized due to the existence of numerous dangling bonds so that it has various "reconstructed" surfaces even if it is a clean surface. In the case that the adsorbates such as alkali metals or noble metals exist on the surface, complex reconstructions occur depending on the amount of adsorbates and substrate temperature.

To understand these reconstructed surfaces, it is essential to know atomic geometry and electronic structure of the surface. A lot of studies have been done by theoretical and experimental approaches such as low energy electron diffraction (LEED), electron energy loss spectroscopy (EELS), ion scattering spectroscopy(ISS), X-ray diffraction (XRD), photoelectron diffraction (PED), scanning tunneling microscopy (STM), and so on. In contrast to most of these experimental methods for atomic structure analysis, photoelectron spectroscopy (PES) is a powerful tool to directly obtain information on electronic structure of the surface. Particularly, angle-resolved photoelectron spectroscopy (ARPES) using photons of several tens of eV is effective to investigate the surface band structure because the emission angle of such photoelectron has a one-to-one correspondence to the wave vector of the initial state. Although most of the measurement have been done by one-dimensional

detection (by means of polar angle scanning) of the photoelectron along a certain azimuthal angle of the sample, two-dimensional measurement can completely resolve two-dimensional band structure of the surface.

Si surface is active due to a lot of dangling bonds which remain even after reconstruction. Si surface is a proper field of adsorption and desorption of various atoms and gas molecules. In various ion desorption processes, the process by electron and photon irradiation is a non-thermal process and has a close relation with the electronic structure of the surface. Since the emission angle of the ion bears the information on adsorption site, and furthermore, the emission angle dependence of the kinetic energy distribution of the ion is expected to reflect the potential distribution in the vicinity of the surface, two-dimensional measurement is desirable rather than one-dimensional one.

1.2 Two-dimensional (2D) measurement

In this thesis, two-dimensional (2D) measurements of photoelectron angular distribution (PEAD) as well as ion angular distribution are performed. Here, "2D measurement" is defined as the measurement of angular distribution of photoelectron and ion without moving detector or sample. To facilitate such a measurement, we used a display-type spherical mirror analyzer[2]. This analyzer can simultaneously measure the kinetic energy and emission angle of charged particles without any angular distortion.

There are several merits in this type of 2D measurement. although details will be described in chapter 2, the most superior point is a very short acquisition time compared to the conventional 2D measurement by means of one-dimensional measurement. In the measurement of PEAD, one can obtain 2D PEAD at one time by 2D measurement. We can easily obtain enough information to discuss the whole band structure in the case of measuring photoelectron with kinetic energy of several tens of eV.

The purpose of this thesis is to investigate three following topics on electronic and ionic processes by using 2D measurement. The usefulness of 2D measurement in studies of surface will be revealed through these investigations.

1.3 Circular dichroism in angular distribution (CDAD) of valence band photoelectron from Si(001) surface

Circular dichroism in angular distribution (CDAD) of photoelectron is asymmetry of PEAD between the incidence of circularly polarized light with opposite polarization. In the case of photoelectron spectroscopy on solid surface, nonzero CDAD has been observed in the emission from π–band of graphite using photon energies of 20–40eV[3]. 2D PEAD on 1T-TaS_2 excited by circularly polarized light was calculated within dipole transition model which also showed apparent CDAD[4]. On the other hand, 2D CDAD in valence band excitation with photons of 30eV has been calculated on Si(001) surface by Solterbeck *et al.* based on highly accurate one-step model[7] which considers multiple scattering of photoelectrons. Regarding the scattering effect, Osterwalder *et al.*[5] has reported that 2D PEAD patterns from energy-integrated valence band excited by unpolarized light with the photon energy of $\geq$1000eV and several tens of eV are very similar to those from near-lying core level and from atomic orbital constituting the valence band, respectively, with considering scattering effects in the final state. Recently, Daimon *et al.* has found CDAD in 2D measurement of core-level photoelectron of Si(001) surface with its kinetic energies of 150 to 450eV [6]. This CDAD was explained by the rotation of the forward focusing peaks due to the angular momentum of outgoing photoelectrons. However, the evidence of 2D CDAD in valence band excitation has not been proved so far.

The aim of this study is to reveal the origin of CDAD of valence band photoelectron from Si(001) surface at different kinetic energies with using circularly polarized synchrotron radiation. For such a purpose, practical measurement of 2D PEAD is essential. We adopted Si(001) surface to compare the experimental 2D PEAD with the previous theoretical work[7]. To make the effect of photoelectron diffraction clear, the measurement was carried out at final state energies of 40, 80 and 250eV. 250eV is comparable to the final state energy in the above mentioned core level emission from Si(001) surface, which will make it possible to discuss the difference between emission from core level and valence band.

1.4 2D photoelectron spectroscopy (PES) of surface states of Si(111)-($\sqrt{3} \times \sqrt{3}$)R30° -Ag surface

Si(111)-($\sqrt{3} \times \sqrt{3}$)R30° -Ag surface has attracted much attention as a typical system of semiconductor–metal interface, and has been investigated by various experimental and theoretical works. Recently, a reliable model of atomic structure has been established which is the so-called Honeycomb Chained Trimer (HCT) model[8]. This model suggests saturation coverage of 1ML resulting in a semiconductive character of this surface. As to the electronic structure, several ARPES studies has revealed the existence of three surface states between Fermi level and binding energy of 2eV[9, 10]. However, the symmetry as well as the origin of those bands have not fully been discussed.

The purpose of this study is to manifest the symmetry of the surface states of this surface using linearly polarized synchrotron radiation. It has been known from very recent ARPES study that the metallic band around the $\bar{\Gamma}$ point of the second Brillouin zone plays an important role in the surface electric conductance[10]. The understanding of the origin of this band is very important.

2D ARPES using linearly polarized light has been suggested to be useful to discuss the initial state symmetry[11]. In this study, this method of determining initial state symmetry has been applied to the discussion of the origin of surface states.

1.5 Adsorption and desorption processes of Cl on Si(001) and (111) surface

The initial stage of dry etching process on chlorinated silicon surface has been inclusively studied since selective excitation is expected on this surface leading to the atomic scale manufacturing. From selective excitation point of view, investigation of the mechanism of ion desorption induced by electron or laser (photon) irradiation seems to be also an interesting matter. On the other hand, adsorption of Cl is expected to form surface dipole layer because of large electronegativity of Cl. Since this layer changes the potential distribution in vicinity of surface, the outgoing ion will be strongly influenced in its kinetic energy, and that is also an attractive subject on this surface.

In this study, the above mentioned problems are revealed by using electron stimulated desorption (ESD) and laser induced ion desorption (LID). In addition, the adsorption process will be investigated by Auger electron spectroscopy (AES) and low energy electron diffraction (LEED). The adsorption site of Cl will be also studied by measuring ion angular

distribution in 2D measurement. It is necessary on this surface to finish all these measurements as soon as possible because of relatively high ionization cross section of Cl atom. In this sense, display-type spherical mirror analyzer is useful, since all the measurements can be carried out without moving the sample.

1.6 Organization of this thesis

Before stepping into the individual topics, the methods and apparatus of the research will be described in chapter 2. The principles of photoelectron spectroscopy as well as ion desorption induced by electronic transition will be briefly described. The details of the two-dimensional detector which was commonly used in the measurements are explained. Chapter 3 and 4 handle the two dimensional measurements of PEAD. In chapter 3, the first experimental evidence of CDAD from Si(001) valence band is presented. The origin of the observed CDAD and the kinetic energy dependence of PEAD will be discussed. In chapter 4, surface states on Si(111)-($\sqrt{3} \times \sqrt{3}$)R30° -Ag surface are investigated. The electronic structure derived from PEAD at various binding energies and the symmetry of each surface state will be discussed. In chapter 5, desorption process by ESD and LID from Cl adsorbed Si surface is studied. Not only desorption mechanism and the escape process of the ion from the vicinity of the surface, but also the adsorption process of Cl will be discussed. Finally, significant information obtained from the three topics is summarized in chapter 6.

References

[1] R. I. G. Uhrberg and G. V. Hansson, Critical Reviews in Solid State and Materials Sciences **17** (1991) 133, and references therein.

[2] H. Daimon and S. Ino, Rev. Sci. Instrum., **61** (1990) 57. H. Nishimoto, H. Daimon, S. Suga, Y. Tezuka, S. Ino, I. Kato, F. Zenitani and H. Soezima, Rev. Sci. Instrum. **64** (1993) 28.

[3] G. Schönhense, C. Westphal, J. Bansmann and M. Getzlaff, Europhys. Lett., **17** (1992) 727.

[4] T. Matsushita, H. Nishimoto, T. Okuda, T. Nakatani, H. Daimon, S. Suga, H. Namba, T. Ohta, Y. Kagoshima, T. Miyahara, J. Electron Spectrosc. Relat. Phenom. **78** (1996) 489. T. Matsushita, S. Imada, H. Daimon, T. Okuda, K. Yamaguchi, H. Miyagi and S. Suga, Phys. Rev.**B56** (1997) 7687.

[5] J. Osterwalder, A. Stuck, T. Greber, P. Aebi, L. Schlapbach and S. Hüfner, Proc. 10th Int. Conf. on VUV Rad. Phys. (1992) and references therein.

[6] H. Daimon, T. Nakatani, S. Imada, S. Suga, Y. Kagoshima and T. Miyahara, Jpn. J. Appl. Phys. **32** (1993) L1480. H. Daimon, T. Nakatani, S. Imada and S. Suga, Rev. Sci. Instrum. **66** (1995) 1510. H. Daimon, T. Nakatani, S. Imada and S. Suga, J. Electron Spectrosc. Relat. Phenom.**76** (1995) 55.

[7] C.-H. Solterbeck, W. Schattke and C. S. Fadley, Surf. Sci. **357–358** (1996) 245.

[8] M. Katayama, R. S. Williams, M. Kato E. Nomura and M. Aono, Phys. Rev. Lett.**66** (1991) 2762.

[9] L. S. O. Johansson, E. Landemark, C. J. Karlsson and R. I. G. Uhrberg, Phys. Rev. Lett.**63** (1989) 2092.

[10] Y. Nakajima, S. Takeda, T. Nagao, S. Hasegawa and X. Tong, Phys. Rev.**B56** (1997) 6782.

[11] H. Daimon, S. Imada, H. Nishimoto and S. Suga, J. Electron Spectrosc. Relat. Phenom., **76** (1995) 487.

Chapter 2

Methods and apparatus of research

2.1 Photoelectron spectroscopy (PES)

Figure 2.1 is a schematic drawing of the energy diagram of *photoelectric effect*. The origin of the electron energy axis is the bottom of the valence band. $E_{\rm i}$, $\rm E_F$, $E_{\rm vac}$ and $E_{\rm f}$ are the energies of the initial state, Fermi level, vacuum level and the final state, respectively. When a photon of energy $h\nu$ is absorbed in the solid, the electron at $E_{\rm i}$ is excited to $E_{\rm f}$. If $E_{\rm f}$ is higher than $E_{\rm vac}$, the electron can escape from the solid as a *photoelectron* with a kinetic energy ($E_{\rm K}$) determined by

$$E_{\rm K} = E_{\rm f} - E_{\rm vac} \quad , \tag{2.1}$$

which is well-known Einstein relation (Einstein 1905). The energy conservation rule requires the relationship

$$E_{\rm f} = E_{\rm i} + h\nu \tag{2.2}$$

Therefore, using ϕ as a work function and $E_{\rm B}$ as a binding energy with respect to $\rm E_F$, eq.(2.1) is rewritten as

$$E_{\rm K} = h\nu - \phi - E_{\rm B} \tag{2.3}$$

This equation is a basis of *photoelectron spectroscopy* which indicates that we can obtain information of $E_{\rm B}$ from the observation of the photoelectron with $E_{\rm K}$ when $h\nu$ and ϕ values are known.

The process of emission of the photoelectron is usually described by three step model as shown in Fig.2.2.

step 1: Optical transition from the initial state to the final state within dipole transition approximation. Here, typical transition time is in the order of 10^{-15}s as referred in the Frank-Condon principle. In addition, this transition is direct transition which conserves the momentum during the transition.

step 2: Migration of the photoelectron to the surface. Some electrons lose a part of their kinetic energy during the migration and become secondary electrons. The characteristic length of this migration is called mean free path, and will be introduced later.

step 3 Emission from the surface climbing up the surface potential.

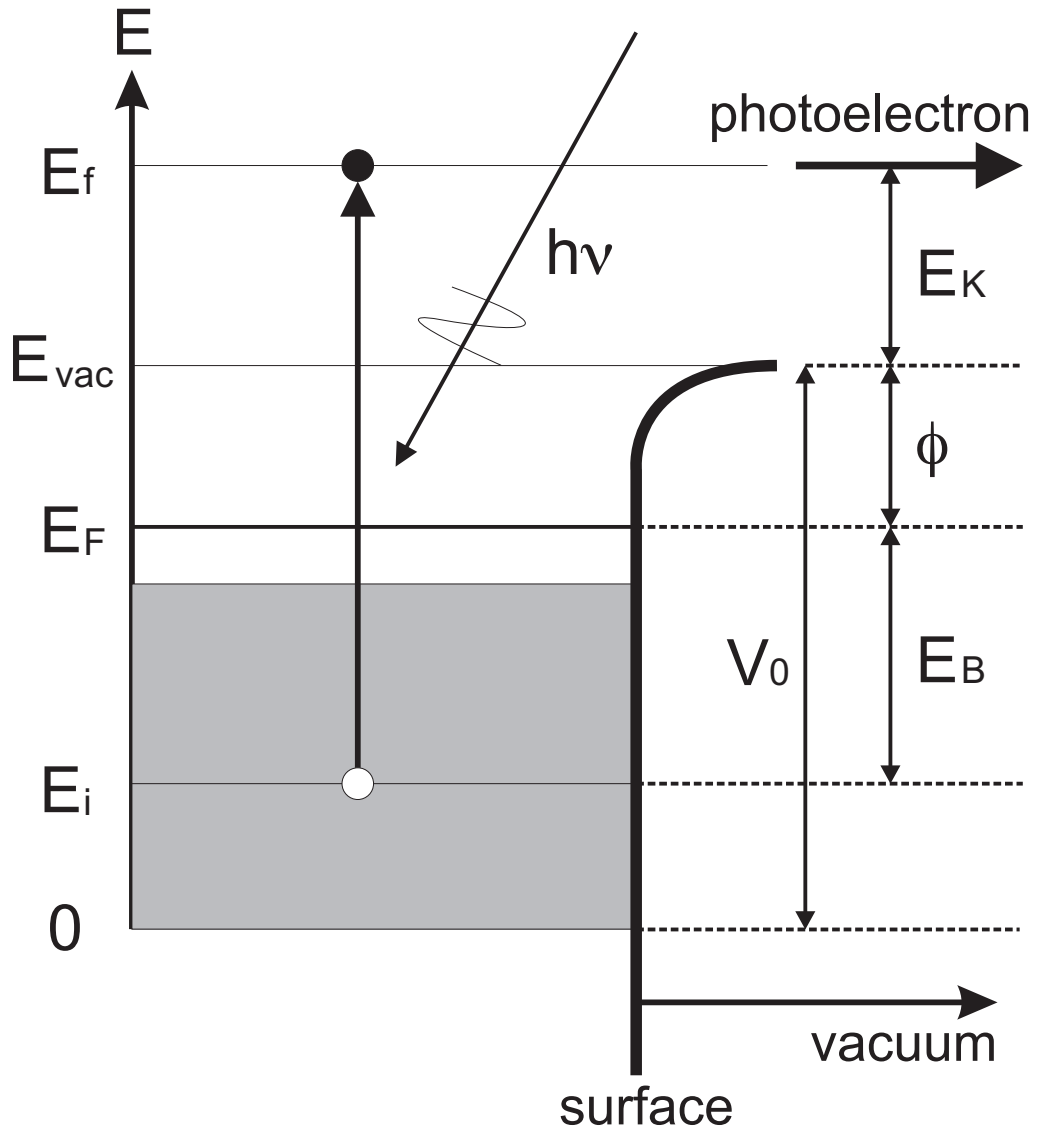

Figure 2.1 Schematic drawing of the energy diagram of photoelectric effect. The origin of energy axis is the bottom of the valence band. Each energy level, E_i, E_F, E_{vac} and E_f correspond to the initial state level, Fermi level, vacuum level and the final state level. The kinetic energy of the photoelectron (E_K), the work function (ϕ), the inner potential (V_0) and the binding energy (E_B) relative to E_F are indicated on the right.

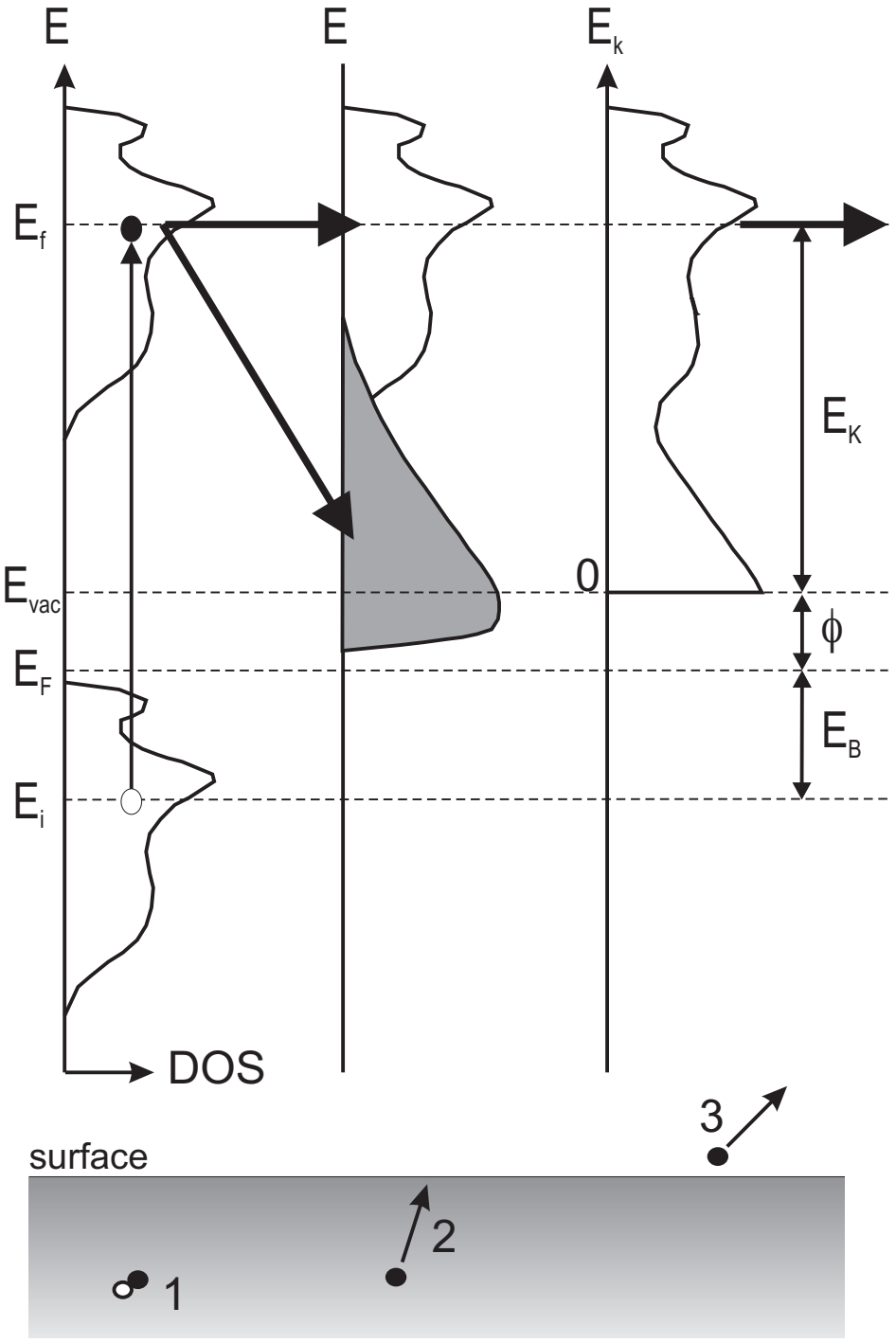

Figure 2.2 Three step model for the emission of the photoelectron. The bottom figure shows a motion of photoelectron in real space; step 1.optical transition to the final state creating a photoelectron, step 2.migration to the surface, step 3. transmission through the surface into the vacuum. Upper part shows energy distribution curves each of which corresponds to each step. The excited photoelectron lose a part of its kinetic energy by inelastic scattering during migration to the surface, resulting in a contribution of the secondary electron (hatched area) in step 2.

As seen in the figure, when we observe the kinetic energy distribution of photoelectron, we can directly obtain the binding energy distribution of the density of states (DOS) of the solid, assuming that the final state is free electron-like. In this sense, photoelectron spectroscopy (PES) is one of the most powerful tool to investigate the electronic structure of solids.

Surface sensitivity of PES is not determined by the penetration depth of the light which is in the order of ∼1000Å at the photon energy region of ultra-violet but by the escape depth of the excited photoelectron. Figure 2.3 shows a universal curve of the mean free path of the electron in solids which depends on its kinetic energy[1]. This curve is known to be not so sensitive to material characters such as metal or semiconductor except for the extremely low energy region. The electron lose a part of its energy by many body effects such as electron-phonon scattering, excitation of plasmon, excitation of electron-hole pair and so on which leads a small mean free path (∼5-6Å) around $E_{\rm K}$ of several tens of eV. These processes usually contribute to the energy distribution curve of secondary electron. In the core level spectrum, they create satellite structures at higher binding energy of the main peak. At smaller $E_{\rm K}$ of a few tens of eV, the mean free path increases because these inelastic scattering processes mentioned above cannot be excited. In larger $E_{\rm K}$ region, on the other hand, the mean free path increases again since the cross section of these processes decreases. This universal curve indicates that the escape depth of the photoelectron in usual kinetic energy region is at most a few tens of Å, which corresponds to almost 10 atomic layers, suggesting that PES is a rather surface sensitive method.

2.2 Angle-resolved photoelectron spectroscopy (ARPES)

Principle of ARPES Generally, the most suitable quantum number is the wave vector $\vec{k}$ to describe electronic states of solids. A certain electronic state is described by its wave vector and energy as ($\vec{k}_{\rm i}$, $E_{\rm i}$) whose dispersion is directly obtained from angle dependence of photoelectron spectra. As mentioned in the last section, PES is rather surface sensitive especially in UPS photon energy region, $h\nu$ 100eV. In this energy region, it can probe only a few atomic layers from the surface, and the dispersion of the surface state could easily be obtained as follows within three step model.

Suppose that the initial state and the final state are described as ($\vec{k}_{\rm i}$, $E_{\rm i}$) and ($\vec{k}_{\rm f}$, $E_{\rm f}$), respectively. $\vec{k}_{\rm i}$ can be replaced by $\vec{k}_{\rm i}+n\vec{G}$ in the Bloch condition, where $\vec{G}$ is the reciprocal lattice vector and n is integer. In a direct optical transition, the momentum and energy conservation rules are written as

$$\vec{k}_{\rm f} = \vec{k}_{\rm i} + n\vec{G} + \vec{q} \tag{2.4}$$

$$E_{\rm f} = E_{\rm i} + h\nu \ , \tag{2.5}$$

where $\vec{q}$ is the wave vector of the incident light. Here, $\vec{q}$ can be neglected in UPS region

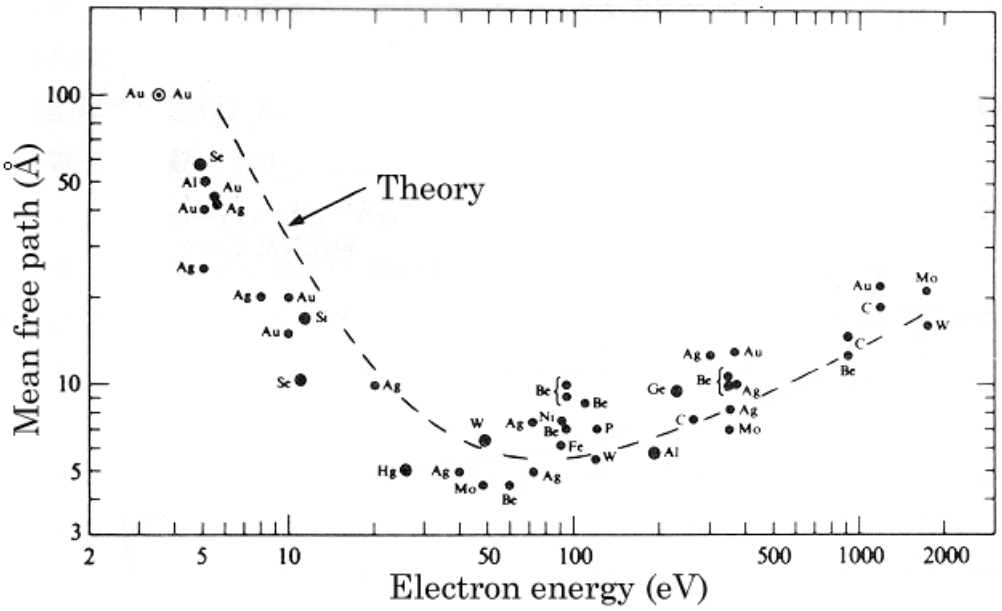

Figure 2.3 "Universal curve" of the mean free path of the electron in solids (Ref.[1], modified). The mean free path has its minimum around the electron energy of several tens of eV, where it corresponds to one atomic layer.

since $|\vec{q}|$ is much smaller than $|\vec{k}_{\rm i}|$, which is in the order of Brillouin zone. Then eq.(2.4) is rewritten as

$$\vec{k}_{\rm f} = \vec{k}_{\rm i} + n\vec{G} \tag{2.6}$$

The photoelectron transmits the surface as shown in Fig.2.4 where the momentum perpendicular to the surface changes because of the inner potential V_0 indicated in Fig.2.1. Fortunately, periodicity parallel to the surface still remains so that the conservation of momentum parallel to the surface is maintained, which is enough condition to investigate surface states described by ($\vec{k}_{\rm i\parallel}$, $E_{\rm i}$). Therefore,

$$\vec{k}_{\parallel} = \vec{k}_{\rm f\parallel} + n\vec{G}_{\parallel} \ , \tag{2.7}$$

where $\vec{k}_{\parallel}$ is a parallel momentum component of emitted photoelectron which is approximately a free electron, and $\vec{G}_{\parallel}$ is the reciprocal lattice vector parallel to the surface. If there is a surface superlattice, $\vec{G}_{\parallel}$ includes its reciprocal lattice vector. This equation also means Bragg's diffraction by surface lattice, which is so-called Umklapp process. From eqs.(2.6) and (2.7),

$$\vec{k}_{\rm i\parallel} = \vec{k}_{\parallel} + n\vec{G}_{\parallel} \tag{2.8}$$

Using kinetic energy $E_{\rm K}$ which is described in eq.(2.3) and the emission angle $\theta_{\rm e}$ of emitted photoelectron, $|\vec{k}_{\rm i\parallel}|$ is written as

$$|\vec{k}_{\rm i\parallel}| = (\sqrt{2{\rm m}E_{\rm K}}\sin\theta_{\rm e})/\hbar + n\vec{G}_{\parallel} \tag{2.9}$$

$$= 0.512\sqrt{h\nu - \phi - E_{\rm B}}\sin\theta_{\rm e} + n\vec{G}_{\parallel} \ , \tag{2.10}$$

considering eq. (2.6). Here, the unit of the wave vector and the energy are [Å^{-1}] and [eV], respectively. This equation suggests that the wave number of the initial state parallel to the surface is directly provided by the photoelectron emission angle.

Although $\vec{k}_{\perp} \neq \vec{k}_{\rm f\perp}$, there is one way to determine the dispersion perpendicular to the surface. Suppose that the final state ($\vec{k}_{\rm f}$, $E_{\rm f}$) is a free electron whose dispersion is parabolic as shown in Fig.2.5, which means

$$|\vec{k}_{\rm f}| = \sqrt{2{\rm m}E_{\rm f}}/\hbar \tag{2.11}$$

Using inner potential of the solid, this assumption leads to

$$|\vec{k}_{\rm i\perp}| = \sqrt{2{\rm m}(E_{\rm K}\cos^2\theta_{\rm e} + V_0)}/\hbar \tag{2.12}$$

In the condition of $\theta_{\rm e} = 0$,

$$|\vec{k}_{\rm i\perp}| = 0.512\sqrt{h\nu - \phi - E_{\rm B} + V_0} \ , \tag{2.13}$$

which indicates that the wave number perpendicular to the surface depends on the photon energy by collecting perpendicularly emitted photoelectron. This kind of experiment can be carried out using photon energy tunable light source, i.e., synchrotron radiation.

In this way, one can obtain the whole energy dispersion of solid by *angle resolved photoelectron spectroscopy* (ARPES).

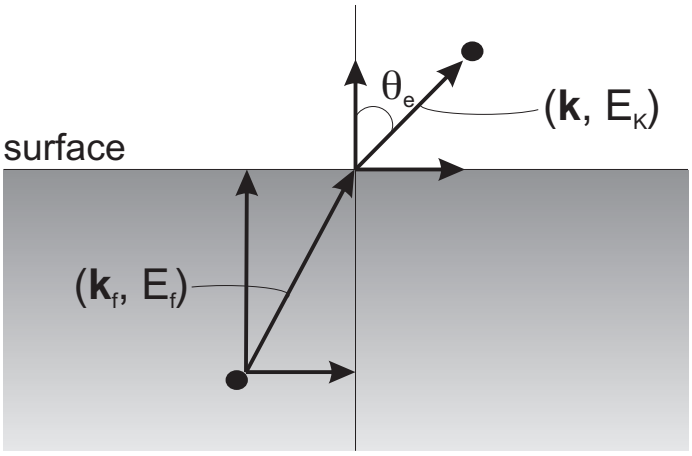

Figure 2.4 Refraction effect for the outgoing photoelectron at the surface. Momentum parallel to the surface is conserved.

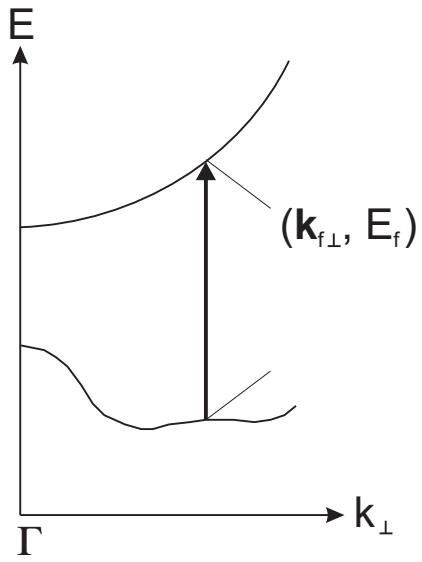

Figure 2.5 Schematic energy dispersion along $k_\perp$ direction and direct transition to the final state which has approximately a parabolic dispersion.

Polarization dependence To describe the photoemission process in detail, a one step model is employed which has the final state of direct transition including transport process to the surface. The differential cross section for the photoelectron emission is given by a *golden rule* as

$$\frac{d\sigma}{d\Omega}(E_{\mathrm{K}}, \vec{k}, h\nu, \vec{A}) \propto \sqrt{E_{\mathrm{K}}} \sum_{\mathrm{i}} |\langle \Psi_{\vec{k}}| \ \vec{p} \cdot \vec{A} + \vec{A} \cdot \vec{p} \ |i\rangle|^2 \ \delta(h\nu - E_{\mathrm{K}} - \phi - E_{\mathrm{B}}) \ , \qquad (2.14)$$

where $\vec{A}$ is a vector potential of electromagnetic field of the incident light and $\vec{p}$ is the momentum operator. Delta function indicates energy conservation rule. Utilizing the dipole approximation, this equation can be developed to a more simple description as

$$I(\vec{k}) \propto |\langle \Psi_{\vec{k}}| \hat{\epsilon} \cdot \vec{r} \ |i\rangle|^2 \ \delta(h\nu - E_{\mathrm{K}} - \phi - E_{\mathrm{B}}) \ , \qquad (2.15)$$

where $I_{\vec{k}}$ is a photoelectron intensity at $\vec{k}$, $\hat{\epsilon}$ is a unit polarization vector of the incident light and $\vec{r} = r\hat{r}$ is a position vector. The contents in the bracket is the matrix element from which transition selection rule is derived. Figure 2.6 shows an experimental geometry using linearly polarized light. Suppose that the polarization vector $\hat{\epsilon}$ is fixed horizontally and the photoelectron is collected in a mirror plane of the crystal. Since the final state $|\Psi_{\vec{k}}\rangle$ is approximately a plane wave at far from the surface, it always has *even* parity with respect to the mirror plane. Here, we think about two conditions; one is a configuration that the mirror plane is parallel to $\hat{\epsilon}$ while another is vertical realized by 90° in-plane rotation of the sample. The latter and the former are so-called $A_\perp$ and $A_\parallel$ configurations, respectively. In $A_\parallel$ configuration, the parity of transition operator in the matrix element is *even* with respect to the mirror plane so that the transition from the initial state with *even* parity is allowed while *odd* parity state is forbidden. On the other hand, in $A_\perp$ configuration, the operator has *odd* parity which leads to an allowed transition only from the initial state of *odd* parity.

In this way, we can distinguish the symmetry of the initial state systematically. Such a method has become general in these days using synchrotron light source[2].

2.3 2D PES

We can investigate an electronic band structure of solids by means of ARPES as mentioned in the last section. It is usual in ARPES measurement to fix the scanning direction of the polar angle θ (i.e., fixed azimuthal angle ϕ) considering the symmetry of the crystal, and measure the spectrum at each polar angle θ. We can obtain enough information about the energy dispersion along the high symmetry line and discuss most of the properties of the system. However, this method is still insufficient to know the whole electronic structure, especially when we want to know an anisotropy of the band structure in the whole k-space. For example, to explain character such as superconductivity of high-$\mathrm{T_c}$ materials, the electrical conduction at the surface, or charge density wave (CDW) of layer

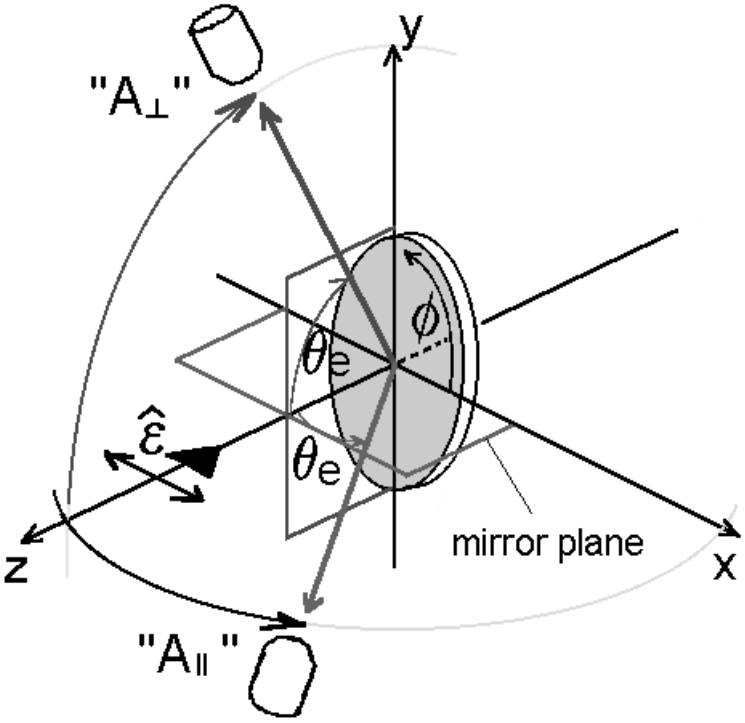

Figure 2.6 Experimental geometry of "polarization dependent" ARPES. The photoelectron is detected in the mirror plane of the crystal. $A_{\parallel}$ is a geometry that $\hat{\varepsilon}$ and the mirror plane are in the same plane, while they are in different planes which cross perpendicularly in $A_{\perp}$ geometry.

compounds, it is very important to know the shape of the Fermi surface. It is possible to obtain such information by carrying out ARPES measurement as usual at all emission angles within hemisphere, but it is not so convenient because it takes enormous time for measurement. If one can measure the photoelectron at whole emission angles at the same time, the measuring time will be considerably shortened. Then the shape of a certain band in the k-space, or in other words, two-dimensional cross section of the band structure will be easily visible when E_{K} of the photoelectron is selected. This is the very important point in which *two-dimensional photoelectron spectroscopy* (2D PES) surpasses conventional one-dimensional ARPES. When linearly polarized light source as synchrotron radiation is used, the 2D PES facilitates to distinguish the symmetry of the initial state.

2.3.1 Principle of 2D PES

General expression of photoelectron angular distribution (PEAD) from valence band, which can be experimentally measured by 2D PES, is briefly reviewed. Since 2D PEAD represents a constant energy surface, the initial states which satisfy the energy conservation rule will show a distribution on the k_x-k_y plane which is called one-dimensional density of states (1D-DOS). It includes the projection of the states along $k_\perp$ direction as well. Using 1D-DOS, PEAD as a function of the direction of the outgoing photoelectron $(\theta_{\vec{k}}, \phi_{\vec{k}})$ can be expressed as

$$I(\theta_{\vec{k}}, \phi_{\vec{k}}) \propto D^1(\vec{k}_\parallel) |\langle f|\hat{\epsilon}\cdot\vec{r}|i\rangle|^2 \ , \tag{2.16}$$

where $D^1(\vec{k}_\parallel)$ is 1D-DOS, $|f\rangle$ is the final state, $\hat{\epsilon}\cdot\vec{r}$ is the operator for dipole transition, and $|i\rangle$ is the initial state. In the case of semiconductor in this thesis, it is sufficient to express $|i\rangle$ by LCAO approximation, as is often the case of other materials such as ionic solids or layer compounds. $|i\rangle$ is an eigen function in Bloch state with the wave vector $\vec{q}$. In the tight binding approximation, it is described as

$$|i\rangle = \frac{1}{\sqrt{N}} \sum_j \sum_{i,\nu} e^{i\vec{q}\cdot(\vec{R}_j+\vec{\tau}_i)} \ a_{i\nu}\phi_{i\nu}(\vec{r}-\vec{R}_j-\vec{\tau}_i) \ , \tag{2.17}$$

where $\vec{R}_j$ is the origin of j-th unit cell, $\vec{\tau}_i$ is a position vector of the i-th atom in the unit cell. $\phi_{i\nu}(\vec{r}-\vec{R}_j-\vec{\tau}_i)$ is an atomic function of the ν-th atomic orbital of the i-th atom, $a_{i\nu}$ is LCAO coefficient of each atomic function, and $e^{i\vec{q}\cdot(\vec{R}_j+\vec{\tau}_i)}$ is a phase factor. On the other hand, $|f\rangle$ is assumed to be free electron-like outside the muffin-tin potential which also satisfies the Bloch theorem and is described using partial wave expansion as

$$|f(r,\theta,\phi)\rangle = 4\pi \sum_{l',m'} (i)^{l'} e^{-i\delta_{l'}} Y^*_{l'm'}(\theta_{\vec{k}}, \phi_{\vec{k}}) Y_{l'm'}(\theta,\phi) R_{E_{\mathrm{K}},l'}(r) \ , \tag{2.18}$$

where $\delta_{l'}$ is a phase shift of the l' wave, $Y_{lm}(\theta,\phi)$ is a spherical harmonic[3] and $R_{E_{\mathrm{K}},l'}(r)$ is the radial part. Defining

$$M \equiv \langle f|\hat{\epsilon}\cdot\vec{r}|i\rangle \qquad \text{and} \tag{2.19}$$

$$A_{i\nu} \equiv \langle f|\hat{\epsilon}\cdot\vec{r}|\phi_{i\nu}(\vec{r})\rangle \ , \tag{2.20}$$

M is rewritten as

$$M = \sum_{\vec{G}} \delta_{\vec{k}-\vec{q},\vec{G}} \sum_{i,\nu} a_{i\nu} e^{-i\vec{G}\cdot\vec{\tau}_i} A_{i\nu} \quad , \tag{2.21}$$

where δ is a δ-function and $\vec{G}$ is reciprocal lattice vector[4]. Assuming that the initial state consists of only ν-th atomic orbital, the term $A_{i\nu}$ can be pulled out of the summation. Therefore, M is the product of two terms and described as

$$\begin{aligned} M &= M_A M_C \\ M_A &\equiv \langle f|\hat{\epsilon}\cdot\vec{r}|\phi_\nu(\vec{r})\rangle \qquad (2.22) \\ M_C &\equiv \sum_{\vec{G}} \delta_{\vec{k}-\vec{q},\vec{G}} \sum_i a_i e^{-i\vec{G}\cdot\vec{\tau}_i} \qquad (2.23) \end{aligned}$$

M_A is the matrix element of dipole transition from the atomic orbital and M_C consists of coefficients of LCAO eigenfunction which is called photoemission structure factor[4]. $|M_C|^2$ determines the intensity distribution through Brillouin zones (BZ). For instance in the case of the π-band of graphite, the distribution of $|M_C|^2$ is calculated as shown in Fig.2.7[4]. Note that nth BZ corresponds to the BZ whose Γ point is denoted as Γ_n.

Consequently, eq.(2.16) is rewritten as

$$I(\theta_{\vec{k}}, \phi_{\vec{k}}) \propto D^1(\vec{k}_\parallel)|M_A|^2|M_C|^2 \tag{2.24}$$

Thus, the angular distributions of 1D-DOS, $|M_A|^2$ and $|M_C|^2$ are the three factors which contribute to PEAD.

The term $|M_A|^2$ Using a radial function $R_{nl}(r)$ and a spherical harmonic $Y_{lm}(\theta,\phi)$, the initial real atomic orbital is written as

$$\phi_{nl\xi}(r,\theta,\phi) = R_{nl}(r) \sum_m b(m) Y_{lm}(\theta,\phi) \quad , \tag{2.25}$$

where n, l, m are principal, azimuthal and magnetic quantum number, respectively, and $b(m)$'s are the coefficients to form real atomic orbitals such as p_x, p_y, and so on, which are indexed by ξ. The dipole transition operator $\hat{\epsilon}\cdot\vec{r}$ is rewritten as

$$\hat{\epsilon}\cdot\vec{r} = \epsilon_x(\frac{x}{r}) + \epsilon_y(\frac{y}{r}) + \epsilon_z(\frac{z}{r}) \tag{2.26}$$

$$\begin{aligned} \frac{x}{r} &= \sin\theta\cos\phi = (\frac{2\pi}{3})^{\frac{1}{2}}(-Y_{11} + Y_{1-1}) \\ \frac{y}{r} &= \sin\theta\sin\phi = i(\frac{2\pi}{3})^{\frac{1}{2}}(Y_{11} + Y_{1-1}) \qquad (2.27) \\ \frac{z}{r} &= \cos\theta = (\frac{4\pi}{3})^{\frac{1}{2}} Y_{10} \quad , \end{aligned}$$

where ϵ_x, ϵ_y and ϵ_z are the x, y and z components of $\hat{\epsilon}$. Using Gaunt coefficients[5] with considering the dipole transition selection rule, $\Delta l = \pm 1$ and $\Delta m = \pm 1 \text{or} 0$, M_A is described

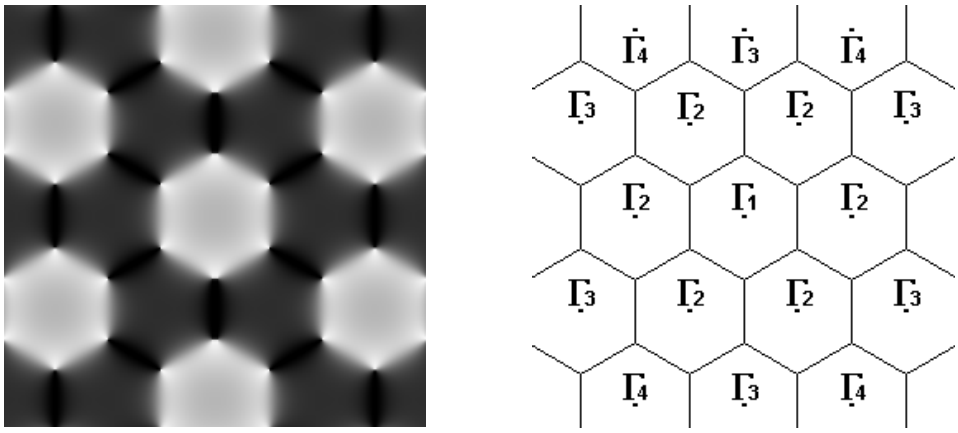

Figure 2.7 The distribution of $|M_C|^2$ for π-band of graphite (Ref.[4]). Hexagonal Brillouin zones (BZs) are also shown. Note that *n*-th BZ corresponds to the hexagonal BZ whose Γ point is denoted as Γ_n. The intensities of the 1st and 3rd BZs are much larger than those of 2nd and 4th BZs.

as[6]

$$
\begin{aligned}
M_A &= \langle f|\ \hat{\epsilon}\cdot\vec{r}\ |\phi_{nl\xi}\rangle \\
&= 8^{\frac{1}{2}}\pi\sum_{l'm} b(m)(-i)^{l'}e^{i\delta_{l'}}R_{l'}(E_{\rm K}) \\
&\quad\times\Big[\epsilon_x\Big\{-Y_{l',m+1}(\theta_{\vec{k}},\phi_{\vec{k}})C^1(l',m+1,l,m)+Y_{l',m-1}(\theta_{\vec{k}},\phi_{\vec{k}})C^1(l',m-1,l,m)\Big\} \\
&\quad+i\epsilon_y\Big\{Y_{l',m+1}(\theta_{\vec{k}},\phi_{\vec{k}})C^1(l',m+1,l,m)+Y_{l',m-1}(\theta_{\vec{k}},\phi_{\vec{k}})C^1(l',m-1,l,m)\Big\} \\
&\quad+2^{\frac{1}{2}}\epsilon_z Y_{l',m}(\theta_{\vec{k}},\phi_{\vec{k}})C^1(l',m,l,m)\Big]\ , \qquad (2.28)
\end{aligned}
$$

where $R_{l'}(E_{\rm K})$ is the radial matrix elements.

In the case of s-orbital as the initial state, the squared M_A is written as

$$|M_A|^2 = 4\pi R_1^2(E_{\rm K})|\hat{\epsilon}\cdot\hat{k}|^2\ , \qquad (2.29)$$

where $\hat{k}$ is a unit wave vector in the direction $(\theta_{\vec{k}},\phi_{\vec{k}})$.

On the other hand in the cases of the initial state except for s-orbital,

$$|M_A|^2 = |(-1)^{l-1}(e^{i\delta_{l-1}}X_{l-1,\xi}+e^{i\delta_{l+1}}X_{l+1,\xi})|^2\ , \qquad (2.30)$$

where $\delta_{l\pm1}$ are the phase shifts of continuum orbital and $X_{l\pm1,\xi}$ are the quantities uniquely determined by $\phi_{nl\xi}$[6]. For example, as for $3p_x$ orbital, which is one of the four orbitals ($3s$, $3p_{x,y,z}$) constituting Si(001) valence band, $X_{l\pm1,3p_x}$ are written as

$$
\begin{aligned}
X_{l-1,3p_x} &= 2\sqrt{\frac{\pi}{3}}R_s\epsilon_x \qquad (2.31)\\
X_{l+1,3p_x} &= -2\sqrt{\frac{\pi}{3}}R_d\{(3x^2-r^2)\epsilon_x+3xy\epsilon_y+zx\epsilon_z\}\times r^{-2}\ , \qquad (2.32)
\end{aligned}
$$

where R_s and R_d are the radial matrix elements for s and d orbitals. $X_{l\pm1,\xi}$ values for other orbitals can be written down in the same way, and are summarized in Ref.[6]. The values of the phase shift ($\delta_{l\pm1}$) and the radial matrix element ($R_{l\pm1}$) for various $h\nu$'s and materials are also carried.

In this way, it is possible to calculate the angular distribution of the term $|M_A|^2$, which are shown in Fig.2.8. In the figure, x and y axes of orthogonal right handed coordinate system are along horizontal and vertical directions within the page, respectively. z axis is perpendicular to these axes. The incident light which is polarized horizontally (i.e., $\hat{\epsilon}=(1,0,0)$) propagates along the $-z$ direction. (a), (b), (c) and (d) correspond to the full hemispherical angular distribution of $|M_A|^2$ from s, p_x, p_y and p_z orbitals, respectively. In these images, there exist characteristic features. For s and p_z orbitals, the intensity distribution along the vertical central line is completely suppressed, whereas there is a large intensity along that line for the p_x orbital. The intensity along both horizontal and vertical central lines disappears in the image from p_y orbital. These characters of $|M_A|^2$ distribution considerably influence the total photoelectron intensity distribution i.e., PEAD, which is the product of 1D-DOS, $|M_A|^2$ and $|M_C|^2$ as introduced in eq.(2.24). This

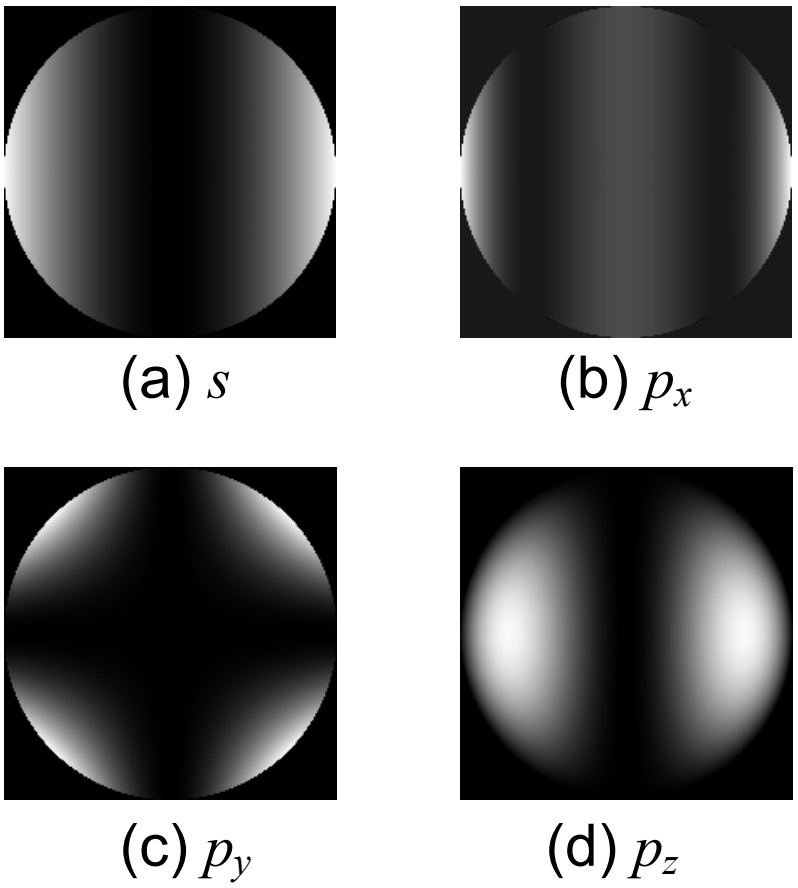

Figure 2.8 Calculated angular distribution of $|M_A|^2$ for the initial state; (a) s orbital, (b) p_x orbital, (c) p_y orbital, (d) p_z orbital. The circumference of each image corresponds to the polar angle of 90°. The right handed coordinate system and the polarization of the incident light are also indicated.

is why 2D PES is effective to investigate the initial state symmetry. These treatments can be slightly modified and applied to the case of photoelectron distribution excited by circularly polarized light.

2.3.2 Apparatus

In order to carry out the 2D measurement, it is necessary to use a special analyzer which can simultaneously analyze the kinetic energy E_{K} and the emission angle $(\theta_{\vec{k}}, \phi_{\vec{k}})$ of charged particles. Eastman *et al.* established such kind of 2D analyzer for the first time[7] which applies elliptical electric field. Some measurement have been done using this analyzer [8, 9, 10]. However, the obtained 2D image has a large angular distortion which makes it difficult to interpret the electronic structure. Even if it is corrected by ray tracing considering the orbital of the photoelectron in the analyzer, the polar acceptance angle is limited.

On the other hand, the 2D analyzer which has been developed by us [11] and used for all the measurements in this thesis can collect the charged particles in the full hemispherical acceptance angle without angular distortion in principle. A schematic drawing of this analyzer which is called *display-type spherical mirror analyzer* is shown in Fig.2.9. This analyzer utilizes a spherical electric field between the outer sphere (a) and the main grid (b). The diameter of (b) is a half of (a). The charged particle which is excited by SR light or laser from behind the outer sphere or the electron from the electron gun (k) leaves the sample (c) and follows linear uniform motion between (c) and (b), which are usually connected to the ground level. Then, it follows Kepler's second law in a spherical electric field between (b) and (a), and again linear uniform motion between (b) and (d) which is the focusing point, aperture. Only the charged particle which has the kinetic energy E_{K} determined by the supplied voltage to (a) comes to the aperture with exactly the same incident angle as the departure angle at (c). The sufficient diameter of the aperture hole is 1mm because that of the excitation area on the sample is limited within 1mm. Consequently, the particle amplified by a coupled MCP (e) hits the fluorescent screen (f) where the fluorescence is recognized as a signal. The two dimensional distribution of the signal is recorded by CCD camera outside the vacuum. This analyzer can analyze either negatively or positively charged particles by switching the polarity of the supplied voltage to (a), which means 2D PES, LEED, AES and ESDIAD measurements are available simultaneously using the same sample, which is the most important in the surface analysis.

The energy resolution, which is almost 1% of the pass energy(=E_{K}), is determined by obstacle rings (g) as a low-pass filter and retarding grid (h) as a high-pass filter. Obstacle rings are lined up along the envelope surface of the orbitals of the charged particle in various emission angles and cut off the particles with too high kinetic energy. The voltage added to retarding grid can be selected with requirement. (i) are guard rings, which correct the disorder of spherical electric field. The high voltage added to (e) and (f) are usually around

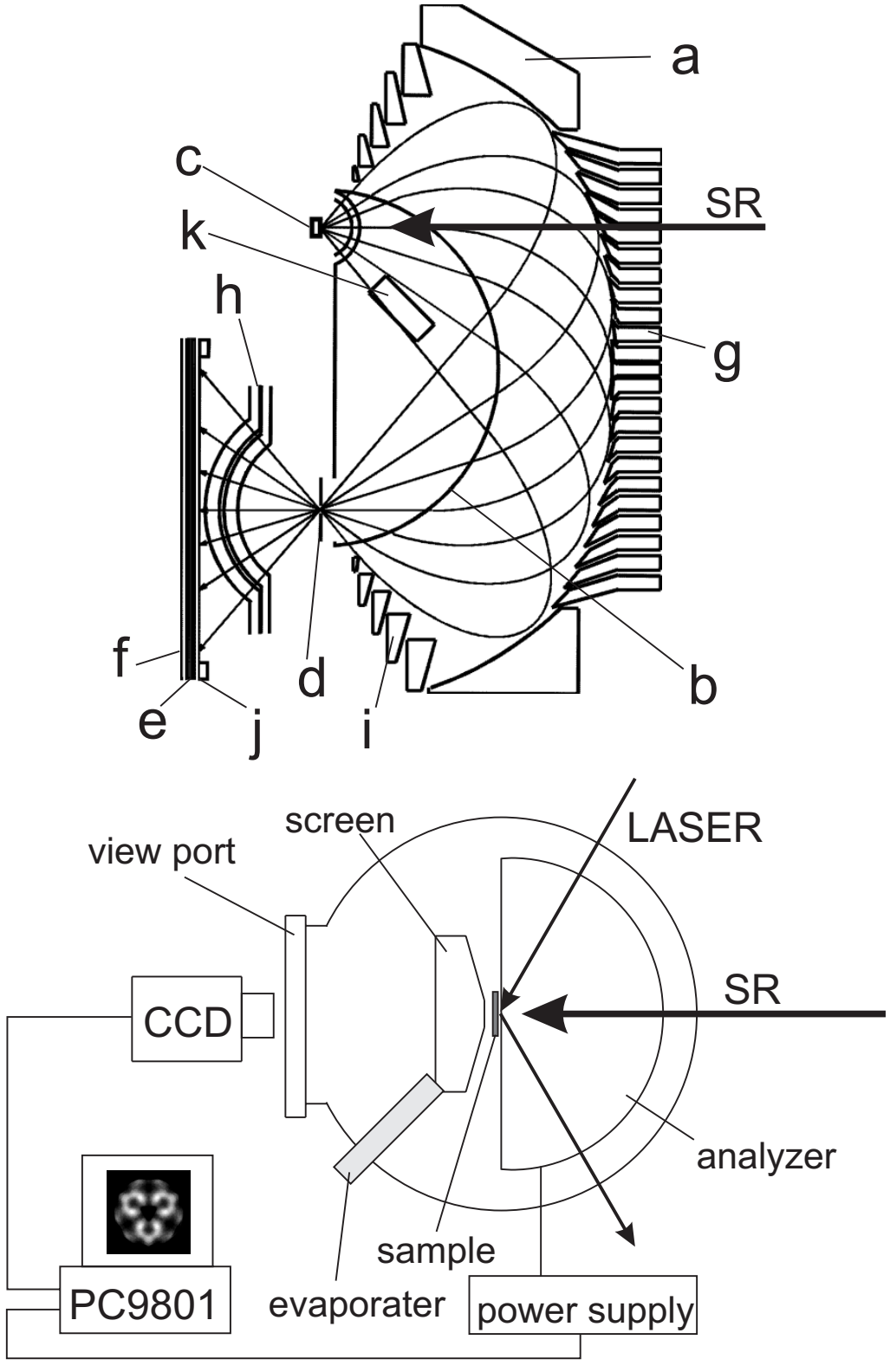

Figure 2.9 Schematic drawing of the side view of "display-type spherical mirror analyzer" (upper) and the plan view of the UHV chamber equipped with this analyzer (lower).

1.6kV between two MCP, and 3kV between the second MCP and the screen. To avoid the penetration of these high voltage field, the plane grid (j) is connected to the ground level, or is -9V added to collect positive particle efficiently when the ion is analyzed.

The angle resolution is determined by the accuracy of the shape of the grids. At the retarding grid, the lens effect also affect the resolution, which is within $\pm 2^\circ$.

In this thesis, three types of analyzer were used for the measuring. Each of which has a slight difference in the acceptance angle and the resolution of higher energy side of E_{K} . The proto-type was used for ESD measurement in chapter 5, which has the acceptance of 40° at most, and the energy resolution determined by the obstacle ring is 1% of the pass energy. In chapter 3 and LID measurement in chapter 5, the second type with 50° acceptance and the energy resolution of 0.5% was used. The third type used in chapter 4 has a larger acceptance angle of 60° .

The incident angle of electron from the electron gun in each type of analyzer is fixed at 45° . In ESD measurement in chapter 5, the current of the electron was less than 1μA to avoid thermal effects and acceleration of Cl desorption.

To measure the flight time of the ion in ESD study, the fluorescent should have a very short decay time which is realized by using a fluorescent substance called P47. However, the luminescence becomes very weak compared to a usual one so that the PIAS system (HAMAMATSU Co., Ltd.) which can collect the signal in photon counting region was used.

2D data processing The data processing is carried out as follows.

- *angle integrated spectrum* Total intensity within the whole 2D plane is collected as scanning the pass energy.

- *angle resolved spectrum* The total intensity in the individual windows which have been appointed beforehand is collected simultaneously as scanning the pass energy.

- *2D PEAD* The signal is counted at each pixels in the whole 2D plane (256×256 pixels in total) until the contrast of the image improves. The pass energy of the analyzer is fixed at a certain energy. It takes typically 20min to obtain each image. Two types of image are needed to obtain a 2D data for one E_{K} , which are "signal" (Sg) and "transmittance" (Trm). Trm image represents the angular distribution of transmittance of the analyzer, and it is obtained by in-plane(ϕ) rotation of the sample considering the symmetry of the crystal. For example, in the case of the crystal with 4-fold rotational symmetry, the sum of the images at each 3° from $\phi = 0^\circ$ to 87° would be sufficient. Another way to take Trm image is to take Sg image of secondary electrons at the same E_{K} but using a different photon energy[9] since the transmittance of the analyzer depends on the pass energy. Dividing Sg by Trm results in a correct data. To obtain PEAD in k-space, the data should be projected to a sphere as schematized in Fig.2.10(a). The acceptance angle θ_{a} is a known value which can be estimated from LEED pattern.

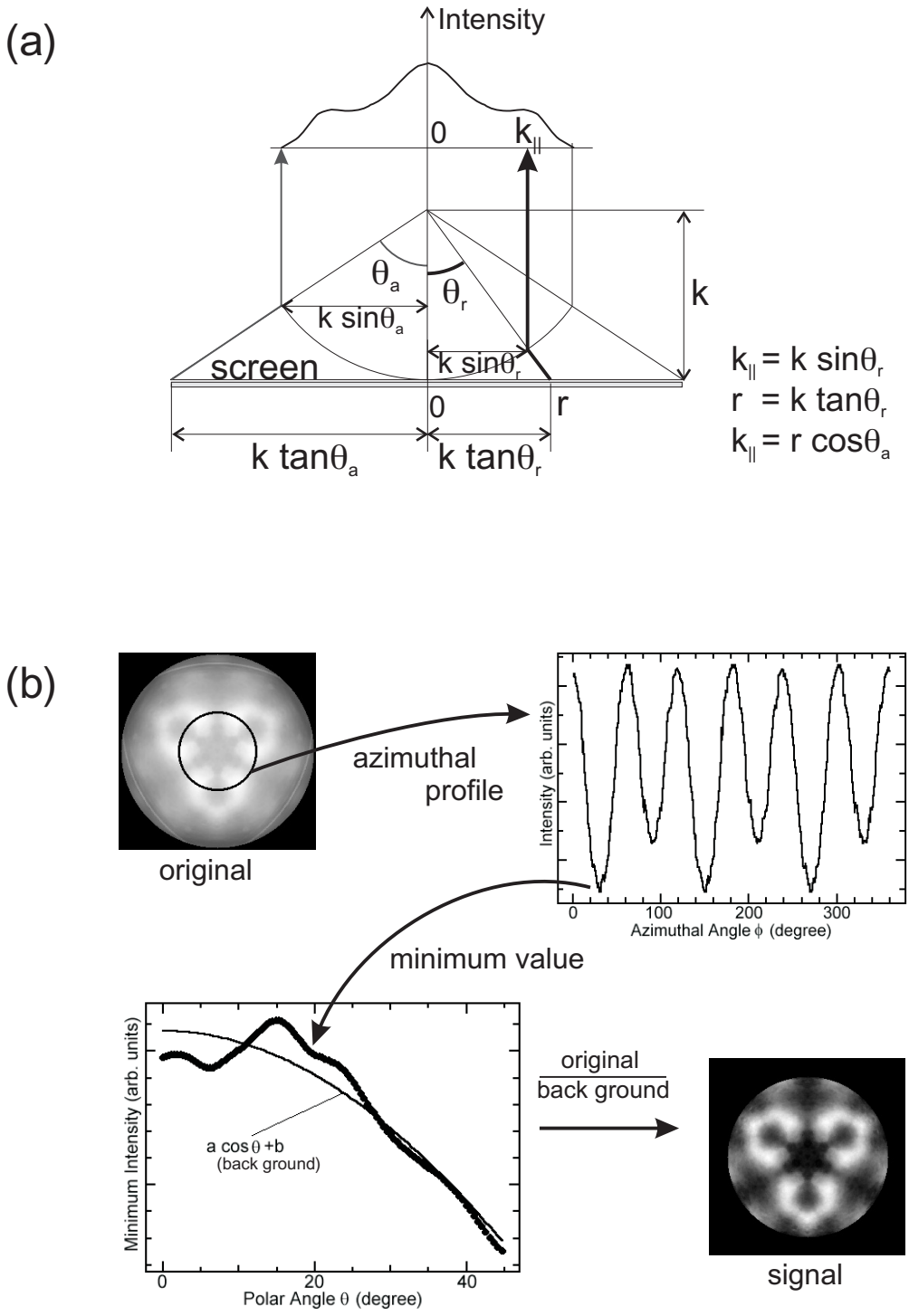

Figure 2.10 (a) 2D image data conversion into *k*-space. θ_a is a known value estimated from LEED pattern so that the intensity at r on the screen is converted into that at $k_{||} = r(\cos\theta_a)$ in the *k*-space. (b) The way of background subtraction.The background level is estimated by fitting minimum intensities of azimuthal scan at each polar angle to cosθ. Dividing the original image by fitted values gives a new image with contributrion only from "signals".

- *Background subtraction* As is often the case after applying rotational or mirror symmetry operation to the image, the background level originating from secondary electron is so high that it is hard to distinguish the states included in the image. In such a case, it is effective to subtract the background as below, which is also shown in Fig.2.10(b). This process is based on the assumption that the escape probability of the secondary electron from the surface depends only on its mean free path normal to the surface. That is, the intensity distribution of the background for polar angle θ is proportional to $\cos\theta$. The procedure is; 1. getting azimuthal profile of the "original" image at each polar angle, 2. plotting the minimum value of each azimuthal scan for the polar angle, and fitting its profile to $\cos\theta$ by least squares method to obtain "background", 3. and finally, dividing the "original" image by "background", which gives "signal" image.

2.4 Synchrotron Radiation (SR)

Recently, photoelectron spectroscopy using synchrotron radiation has got a great progress. Compared to the usual light source such as He discharged lamp or X-ray source, synchrotron radiation has much advantage in the intensity and linearity. The most superior points are that one can use completely linearly polarized (or circularly polarized) light and also variable photon energies on demand. In this thesis, synchrotron radiation was used in all the measurements of PES as a cooperated user. In the following, each of the light source will be briefly introduced.

AR NE1B and PF BL28A in KEK In chapter 3, the beamline NE1B at 6.5GeV accumulation ring (AR) and the beamline 28A at 2.5GeV photon factory (PF) ring in High Energy Accelerator Research Organization in Tsukuba were used as a circularly polarized light source in XPS and UPS region, respectively. These beamlines are equipped with the insertion devices named the elliptical multipole wiggler, EMPW#NE1 and EMPW#28, respectively, and the "dragon" type monochrometer optics which cover the photon energy range of 240eV-1.5keV and 5-300eV, respectively[12, 13].

Each insertion device consists of a combinations of horizontal and vertical permanent magnets made of NdFeB alloy. The number of the period, N, and the period length, λ_u are 21 and 16cm at NE1, respectively, while they are 12 and 16cm at BL28, respectively [14, 13]. The horizontal magnets are arranged with phase difference of $\lambda_u/4$ magnetic period which is the same as vertical ones, as shown in Fig.2.11. The electron traces helical orbital when it travels along this magnetic field which leads to the radiation of circularly polarized light. The polarity is switched by changing the relative position of horizontal and vertical magnet arrays to an optical axis by $\pm\lambda_u/4$. Each insertion device was operated in helical undulator mode in the experiments in this thesis, and the wavelength of the

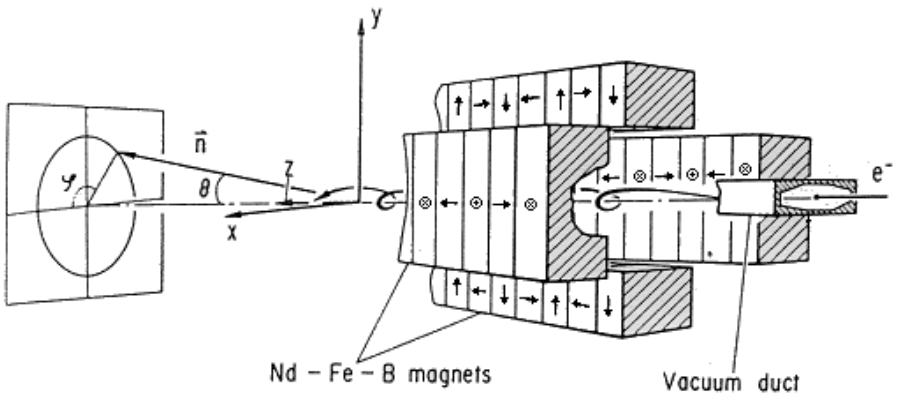

Figure 2.11 Schematic drawing of the insertion device (Ref. [14]). Arrows represent the magnetization direction of each magnets.

radiation is expressed as

$$\lambda_n = \frac{\lambda_{\mathrm{u}}}{2n\gamma^2}(1 + \frac{K^2}{2}) \ , \tag{2.33}$$

where K is the deflection parameter which characterize the insertion device and is related to the strength of magnetic field derived from the gap length of the magnets across each other. n and γ represent the harmonic order and the electron energy in the rest mass units. In this thesis, only the first harmonic peak was used where the circular polarization is expected to be almost 95% even at after the monochrometer. Using the above equation, one can obtain a required photon energy by changing the gap length of the insertion device. In the experiment at PF BL28A, the photon energy at a few % below the peak energy was used since rather larger polarization can be obtained. The beam current measured at the post mirror was in the order of 100pA at both beam lines.

BL4 at SOR-RING In chapter 4, the beamline 4 at 500MeV SOR-RING in ISSP was used as a linearly polarized vacuum ultra-violet (VUV) light source[15]. The beamline is equipped with a bending magnet and the plane grating monochrometer(PGM) optics which covers 20-200eV photon energies. In this thesis, photon energy of 32eV was used since one can obtain the best performance at this photon energy either in the intensity or the energy resolution.

In each experiment at the three beamlines, the UHV chamber equipped with a display-type spherical mirror analyzer was attached to the end of the beamline so as to realize the normal incidence of the light to the sample.

2.5 CDAD

The original meaning of circular dichroism is a different absorption coefficient between left and right circularly polarized (LCP and RCP, respectively) light. This phenomenon is always observed for chiral materials and circularly polarizing plate is one of the application. In this thesis, circular dichroism in angular distribution (CDAD) of the photoelectron is investigated which is in brief an asymmetry of the PEAD caused by the incidence of LCP and RCP light.

To observe CDAD, chiral target such as a molecule without any rotational center and mirror plane of symmetry, or "chiral" experimental geometry is needed. In other words, CDAD is expected on non-magnetic and non-chiral materials using chiral experimental geometry, in which three directions − light propagation, sample normal and photoelectron collection − are not coplanar as shown in Fig.2.12(a). Using this geometry, nonzero CDAD effects have been observed in several molecular adsorbed surfaces, including C 1s emission from CO/Pd(111)[16] and O 2p emission from O/Gd,Nd,Tb(0001) surfaces[17]. Schönhense *et al.* also used this geometry for the valence band excitation of graphite and found strong

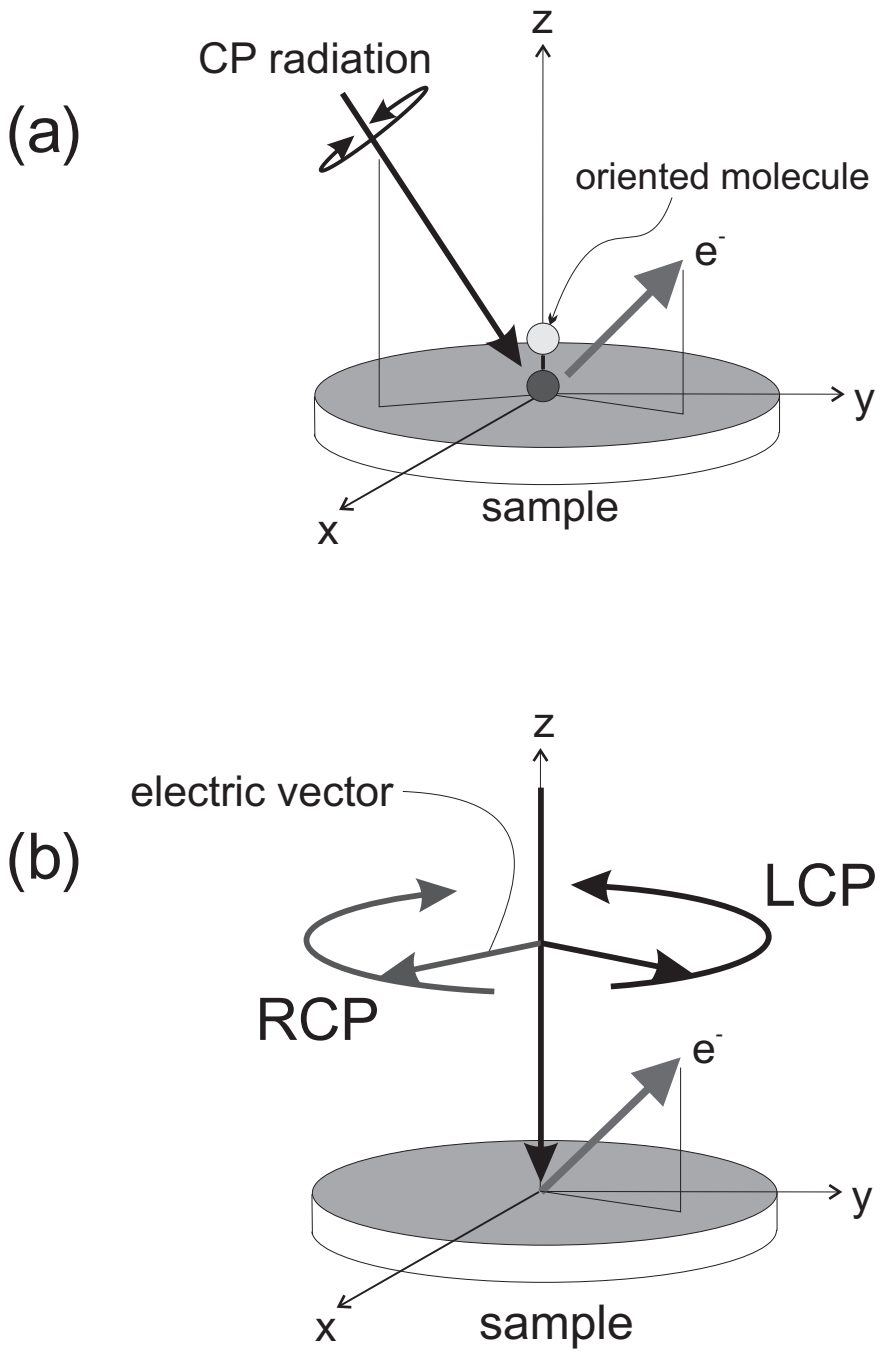

Figure 2.12 Experimental geometry of CDAD measurement. (a):"chiral" geometry where the light propagation, photoelectron collection and sample normal (or orientation of the adsorbate) direction are not coplanar. (b):"non -chiral" geometry where the incident angle of the light is normal direction, which is employed in chapter 3.

CDAD from π-band which is explained by the dipole transition regime of the excitation from atomic p_z orbital[18].

On the other hand, circularly polarized synchrotron radiation has become easy to deal with due to the recent development of insertion devices, which leads to a new type CDAD found in the 2D measurement in core level excitation of non-magnetic and non-chiral Si(001) surface[19].This type CDAD was found in "non-chiral" geometry where the incident angle of the light was perpendicular to the surface. The incidence of the light in soft X-ray region results in PEAD characterized by the rotation of the forward focusing peaks from mirror planes of the crystal. The rotation direction is opposite due to the polarization, because of the angular momentum of outgoing photoelectrons.

In this thesis, in chapter 3, the same "non-chiral" geometry was adopted as shown in Fig.2.12(b) in order to directly compare the results with those of previous work on core level emission from Si(001). z-axis of the coordinate system corresponds to the normal direction of the sample and the circularly polarized light propagates to $-z$ direction. In this thesis, LCP and RCP are defined as the polarities whose electric vector moves counterclockwise (CCW) and clockwise (CW) on the sample as time goes by. Therefore, the unit polarization vector $\hat{\epsilon}$ is $(1, +i, 0)/\sqrt{2}$ for LCP and $(1, -i, 0)/\sqrt{2}$ for RCP radiation.

2.6 Desorption induced by electronic transition (DIET)

Desorption of the particles from solid surface is one of the most important phenomena to solve kinetics at the surface. The driving force of the desorption is divided roughly into three categories; ion impact, thermal activation, and electronic transition. The desorption of the ion due to the ion impact is applied to the surface analysis, so-called secondary ion mass spectroscopy (SIMS). SIMS uses heavy ions as primary ions so that the desorption occurs by the momentum transfer. The information of stoichiometry in the local area is obtained although it is accompanied by serious surface damage. Thermal desorption (TD) is induced by the lattice vibration which derives from thermal activation. There are several vibrational states in the adsorption potential well of the ground state as shown in Fig.2.13(a). If the system was thermally excited to one of the vibrational states which exceeds the potential barrier E_{d}, the adsorbate could desorb as a neutral. The characteristic quantity of E_{d} at each adsorption site will cause the site selective desorption. The desorption induced by electronic transition (DIET) occurs as a result of electron or photon irradiation to the surface which are called electron stimulated desorption (ESD)[20] and photon stimulated desorption (PSD)[21], respectively. The desorption species in DIET are positive and negative ion, neutral and metastable particles, but in this thesis, positive ion desorption is studied.

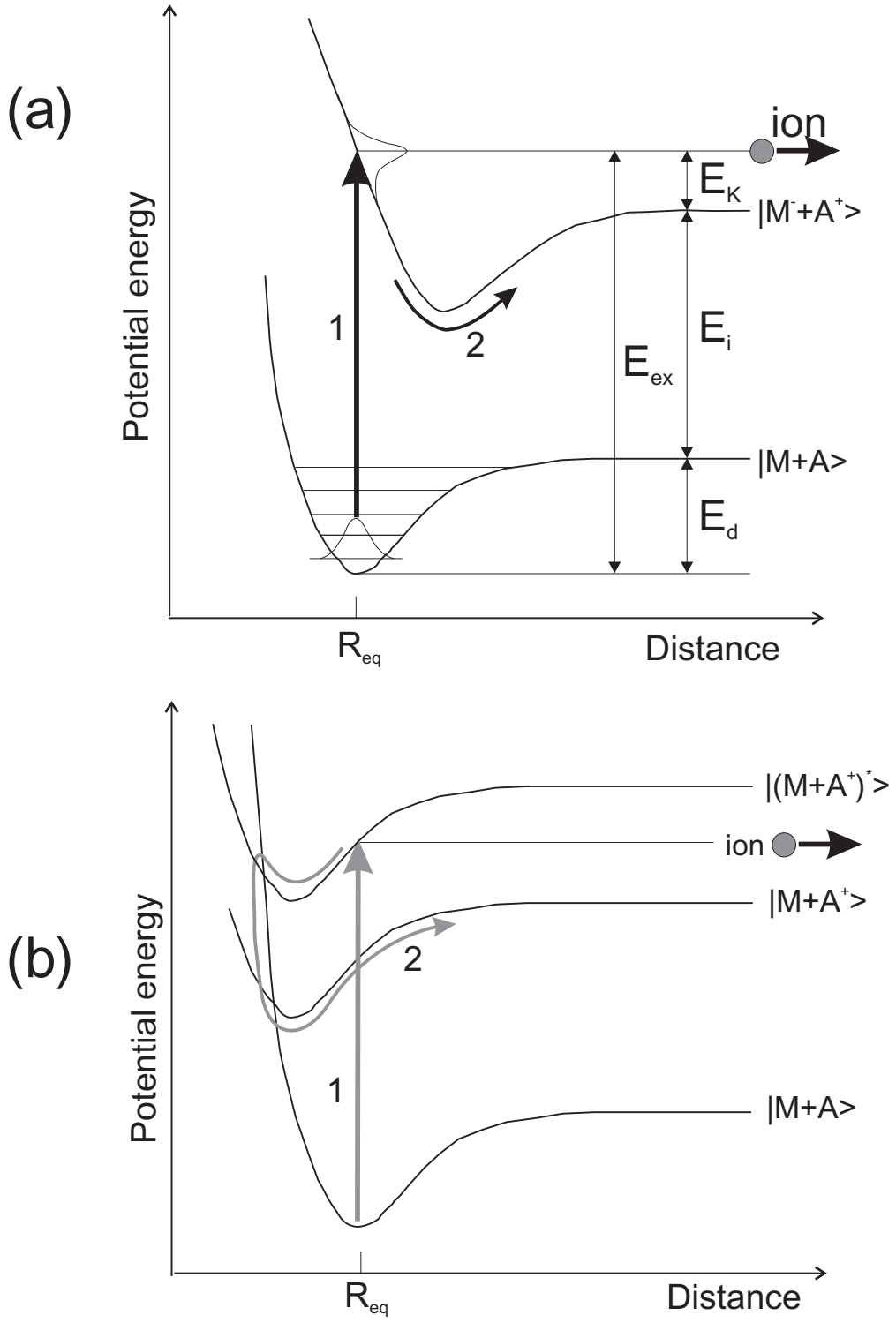

Figure 2.13 Schematic illustration of potential curves for MGR-type desorption. (a) |M+A> is the ground state and the gaussian denotes its wave function. Vibrational states are also represented. Following Franck-Condon excitation of the system by the excitation energy E_{ex} to the ionic state $|M^-+A^+>$ (1), the ion moves along the gradient (2) resulting in the desorption with the kinetic energy E_K. E_d and E_i represent the adsorption energy and ionization energy, respectively. (b) Energy diagram of Antoniewicz bounce. After the excitation (1), the excited particle approaches to the substrate followed by the resonant tunneling to |M+A> and $|M+A^+>$ (2).

2.6.1 Principle of DIET

Figure 2.13(a) represents the schematic potential diagram including the ground state and the excited state which are related to DIET. The adsorbate at the equilibrium position $R_{\rm eq}$ desorbs as a positive ion as follows;
1: Franck-Condon transition to the ionic state within the order of $\sim 10^{-16}$s by the excitation energy of $E_{\rm ex}$.
2: The adsorbate moves along the gradient of the potential curve to the vacuum. If the obtained kinetic energy during the process was larger than the potential barrier, it could desorb with the kinetic energy of $E_{\rm K}$.
This is the well-known MGR(Menzel-Gomer-Redhead) model[22]. Negative ion, neutrals or a metastable particle can also desorb by changing the excited state. If the image force between the created ion and the substrate was taken account, the equilibrium position of the excited state would lie close to the surface. The energy diagram in this case is schematized in Fig.2.13(b). Following the excitation (1), the adsorbate moves towards the surface along the gradient and tunnels to the ground state and the ionic state at the cross points (2), and finally, the positive ion desorbs. This is so-called Antoniewicz bounce[23] which was proposed to explain the desorption of physisorbed species from metal surface.

Here, one should notice that most of the ion deexcites to the ground state or the antibonding state (not shown) during the desorption process since the life time of the ionic state ($\sim 10^{-16}$s) is much shorter than the time which is necessary for the ion to escape from the vicinity of the surface ($\sim 10^{-14} - 10^{-13}$s). This process is called reneutralization which results in the desorption as a neutral.

Since MGR-type mechanism is based on the charge transfer between two bodies, it is suitable to explain the desorption due to valence band excitation.

On the other hand, there is another mechanism called KF model[24] which was suggested to explain O^+ desorption from the ionic solid, TiO_2, following the excitation of Ti $3p$ core hole. Figure 2.14 illustrates the process with three steps.
1. Core hole excitation by the excitation energy.
2. Inter-atomic Auger decay through O $2p$ band within the time scale of $\sim 10^{-15} - 10^{-14}$s.
3. O^+ desorption caused by Coulomb repulsion among two or three holes created.

Franchy and Menzel revealed this mechanism[25], in which the core ionization initiates the desorption, could occur even in the covalent bonded adsorption system, CO/W(100), although intermediate Auger decay is an intra-atomic one within the adsorbate. The Coulomb interaction energy resulting from two holes greater than the half bandwidth is suggested to prevent reductions in the desorption cross section[26] which means the lifetime of the excited state is long enough for the ion to escape from the surface. At present, this Auger relaxation intermediate desorption is generally called *Auger stimulated ion desorption* (ASID) which attracts the interest from the site selectivity point of view[27, 28, 29].

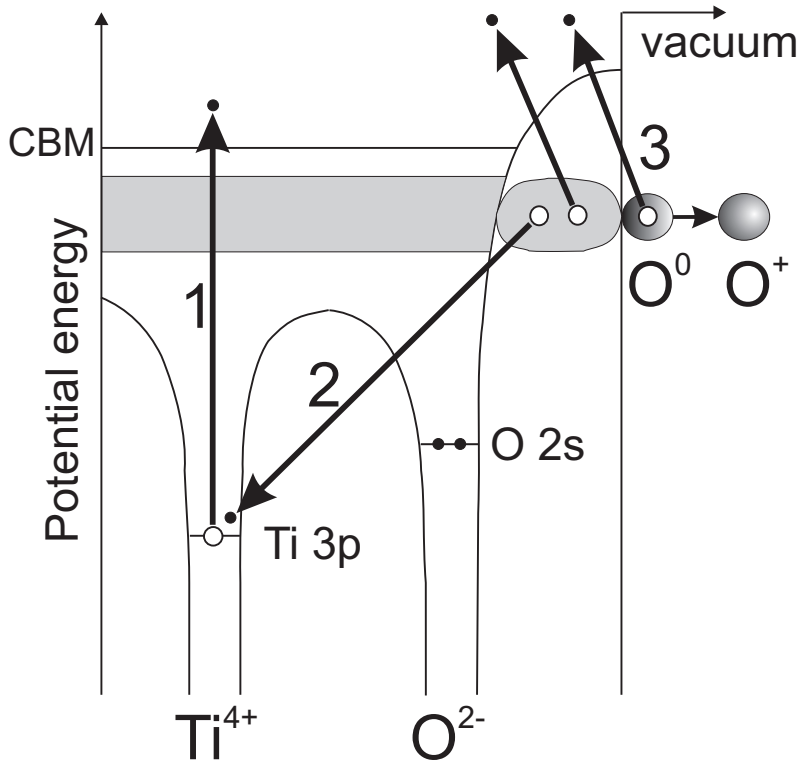

Figure 2.14 Schematic illustration of inter-atomic Auger decay resulting in O^+ ion desorption from the ionic solid, TiO_2, which is so-called KF model. Following the excitation of Ti 3p core hole (1), two or three holes are created by the Auger relaxation (2, 3), and finally O^+ ion desorbs by Coulomb repulsion between the localized holes.

Investigation of the desorption mechanism is usually carried out experimentally by collecting desorbates with varying excitation energies. If there were a threshold corresponding to a certain core hole excitation, one could presume that the desorption mechanism is ASID. However, we have to be careful whether it is really assigned to ASID or not, because there are indirect paths to the ion desorption triggered by the core hole excitation. One of which is called X-ray induced ESD (XESD) where the photoelectron or secondary electron as a result of core hole excitation induces the desorption. This mechanism was first proposed by Jaeger *et al.* [30] on H^+ desorption from multiple NH_3 layers on Ni(110) surface. A usual way to distinguish direct ASID and indirect effects is comparing the ion yield spectrum with that of the total electron yield[28] which is considered to reflect XESD ion. To confirm that the desorption mechanism is ASID, however, it is necessary to detect the coincidence of the excited core electron with the ion desorption, as recently reported on H^+ desorption from condensed $Si(CH_3)_4$[29].

In the case of valence excitation, an indirect process is also suggested, although most of the desorption product is reported to be neutral species from adsorbate/metal substrate system. The mechanism includes three steps, e.g., the excitation of electron-hole pair in the bulk by the incident energy, transport of the created "hot" carriers to the localized adsorption site, and eventual breaking of the unstabilized bond. This hot carrier intermediate desorption is also seen in the gas molecule (or atom)/semiconductor system, such as NO/Si(111)[31] and Cl/Si(111)[32].

Angular distribution of desorbed ion ESD ion angular distribution (ESDIAD) has information of the adsorption site from which the ion desorbs. The desorption process consists of two steps; excitation to the ionic state and successive motion to the vacuum. Therefore, the total cross section of the desorption would be the product of the transition probability and the survival probability near the surface. Assuming that the vibrational wavefunction of the ground state is a three dimensional Gaussian, the transition probability has its maximum in the direction of chemical bond[33] which means that the desorption direction corresponds to the bond direction of the adsorbate as shown in Fig.2.15(a). However, the desorption angle is affected by the final state effect, which contains the image potential and reneutralization effects.

Image potential of the desorbing ion acts as a long-range Coulombic attractive force ($\propto -\frac{1}{z}$) which reduces only the momentum perpendicular to the surface of the ion. Figure 2.15(b) shows such a situation where $\theta_{\rm i}$, $\theta_{\rm f}$, z_0 and $V_{\rm i}(z_0)$ are the initial bond angle, the affected emission angle, the distance between the initial ion position and the image plane, and the image potential at z_0, respectively. Clinton estimated the change of the emission angle of the ion from a metallic surface[33] and derived the relationship between $\theta_{\rm i}$ and $\theta_{\rm f}$ as

$$\begin{aligned} \cos\theta_{\rm f} &= \left\{(1+\delta)\cos{\theta_{\rm i}}^2 - \delta\right\}^{\frac{1}{2}} \\ \delta &= V_{\rm i}(z_0)/E_{\rm K} \ , \end{aligned} \tag{2.34}$$

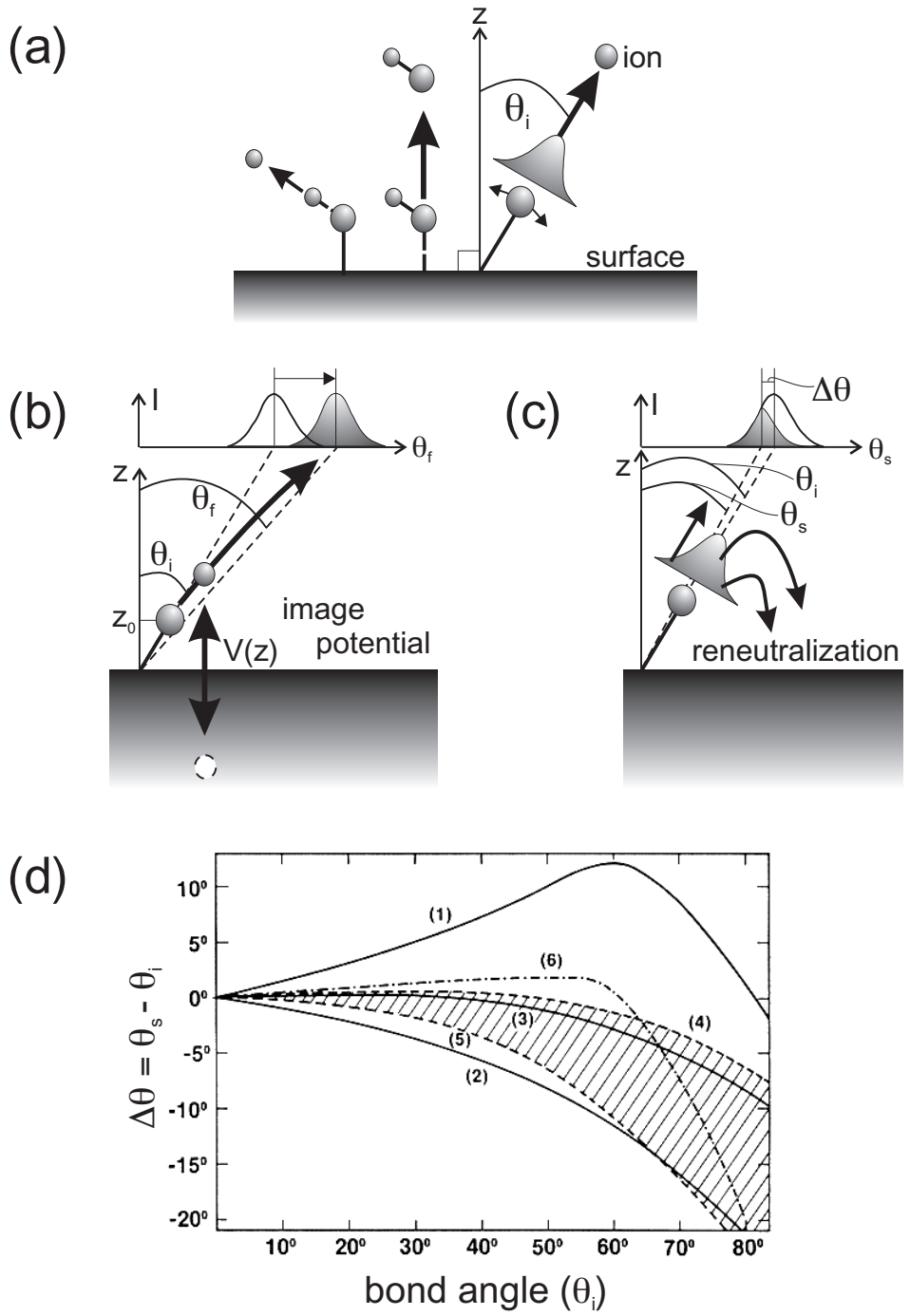

Figure 2.15 Principle of ESDIAD. (a):The initial bond angle (θ_i) is basically conserved. (b): θ_i is quenched to the larger angle θ_f by the attractive image force. (c): The reneutralization results in the smaller observation angle θ_s. (d): Total variation angle $\Delta\theta$ due to (b) and (c) with respect to θ_i (Ref. 34, modified). The curve 1 and 2 are the individual contribution from (b) and (c), respectively. The curve 6 is a simple sum of the curve 1 and 2. Curve 3 represents the situation in which δ (appeared in eq.(2.34)) corresponds 0.2. The practical variation angles are involved in the hatched area between curve 4 ($\delta=\infty$) and 5 ($\delta=0$). If θ_i is smaller than 40° , $\Delta\theta$ is so small that one can investigate the geometry of the adsorbate system using ESDIAD.

where E_K is an initial kinetic energy of the ion. This equation suggests that the larger the bond angle is, the greater the effect of the image potential becomes so that the observed angle of the ion (θ_s) shifts away from the normal direction.

Another final state effect, reneutralization, is represented by the recapture rate which has in a conceptual form as a function of the distance from the surface

$$R(z) = A\exp(-az) \quad , \tag{2.35}$$

where A and a are constants. Considering this equation, it is hard to desorb for the ions which is rather near the surface in the spatial distribution of 3D Gaussian so that θ_s shifts toward normal direction as shown in Fig.2.15(c).

The above two final state effects, which are competitive as to the variation of the observation angle $\Delta\theta(= \theta_s - \theta_i)$, were both taken account in the calculation[34] and the result of which is shown in Fig.2.15(d). The figure indicates that $\Delta\theta$ is comparable to the general angle resolution of the analyzer for θ_i 40° , while for larger θ_i, one has to take care for the final state effects. This result suggests that the initial bond angle is directly reflected to the observed desorption angle in most of the system, which recommends ESDIAD for one of the tools to determine the atomic scale geometry of the adsorbate system.

2.6.2 Laser induced desorption (LID)

Laser induced desorption (LID) can be defined as PSD using laser. There is an interesting phenomenon so-called laser ablation, in which the target solid becomes plasma in a local area due to the high power of laser leading to the desorption of ions, atoms, molecules, clusters, etc. Laser ablation, whose early stage is suggested to be the core hole excitation even if the target is a metal surface[35], has been paid much attention in these days because of the application to laser MBE method to make an artificial lattice. But the topics to study in this thesis is a completely non-thermal process, namely, DIET, and it is important to prevent thermal effects in spite of the high power of laser. In the case of Ge surface, the threshold laser fluence for visible plasma formation was reported to be $\sim$650mJ/cm^2[36] so that the fluence less than a few hundreds mJ/cm^2 is expected to be enough to avoid thermal process. Actually, the evidence of non-thermal reaction is found in Cl/Si(111) system below 150mJ/cm^2[32].

In present, the available wave length to generate by laser is limited within the range of ultra-violet to infrared light. Although most of the investigations have been reported on the valence band excitation resulting in the neutral desorbates, some papers report on the ion desorption. One of them is NO^+ desorption from Pt(111) surface[37] where neutral NO is created as a result of valence excitation by one photon process followed by the ionization in the vicinity of the surface due to two photon process. Ge^+ desorption from Ge surface is also suggested which follows four photon process[36], and the early stage of the ablation of Sr metal is reported to be the excitation using four photons as mentioned above[35]. If

these facts represented core hole excitation, the nonresonant multiphoton ionization cross section should have sufficiently large value. This problem will be discussed in detail in chapter 5.

References

[1] A. Zangwill, *Physics at surfaces, Cambridge University Press* (1988).

[2] R. I. G. Uhrberg and G. V. Hansson, Critical Reviews in Solid State and Materials Sciences **17** (1991) 133.

[3] $Y_{lm}(\theta,\phi) \equiv (-1)^{\frac{m+|m|}{2}} \left\{ \frac{1}{\sqrt{2\pi}} \sqrt{\frac{2l+1}{2} \frac{(l-|m|)!}{(l+|m|)!}} P_l^{|m|}(\cos\theta) e^{im\phi} \right\}$, where $P_l^{|m|}(\cos\theta)$ is an associated Legendre function.

[4] H. Daimon, S. Imada, H. Nishimoto and S. Suga, J. Electron Spectrosc. Relat. Phenom. **76** (1995) 487.

[5] $C^k(l',m',l,m) = \sqrt{\frac{4\pi}{2k+1}} \iint Y_{l',m'} Y_{k,m'-m} Y_{lm} \sin\theta d\theta d\phi$.

[6] S. M. Goldberg, C. S. Fadley and S. Kono, J. Electron Spectrosc. Relat. Phenom. **21** (1981) 285.

[7] D. E. Eastman, J. J. Donelon, N. C. Hien and F. J. Himpsel, Nucl. Instrum. Methods, **172** (1980) 327.

[8] A. Santoni, L. J. Terminello, F. J. Himpsel and T. Takahashi, Appl. Phys. **A52** (1991) 299.

[9] F. J. Himpsel, P. Heimann and D. E. Eastman, Phys. Rev. **B24** (1981) 2003.

[10] F. J. Himpsel, L. J. Terminello, D. A. Lapiano-Smith, E. A. Eklund and J. J. Barton, Phys. Rev. Lett. **68** (1992) 3611.

[11] H. Daimon and S. Ino, Rev. Sci. Instrum., **61** (1990) 57. H. Nishimoto, H. Daimon, S. Suga, Y. Tezuka, S. Ino, I. Kato, F. Zenitani and H. Soezima, Rev. Sci. Instrum. **64** (1993) 28.

[12] H. Kawata, T. Miyahara, S. Yamamoto, T. Shioya, H. Kitamura, S. Sato, S. Asaoka, N. Kanaya, A. Iida, A. Mikuni, M. Sato, T. Iwazumi, Y. Kitajima and M. Ando, Rev. Sci. Instrum. **60** (1989) 1885.

[13] Y. Kagoshima, S. Muto, T. Miyahara, T. Koide, S. Yamamoto and H. Kitamura, Rev. Sci. Instrum. **63** (1992) 1289.

[14] S. Yamamoto, T. Shioya, S. Sasaki and H. Kitamura, Rev. Sci. Instrum. **60** (1989) 1834.

[15] *Activity report of synchrotron radiation laboratory 1995, The Institute for Solid State Physics, the university of Tokyo* (1996) 14.

[16] C. Westphal, J. Bansmann, M. Getzlaff and G. Schönhense, Phys. Rev. Lett.**63** (1989) 151.

[17] M. Getzlaff, J. Paul, J. Bansman, Ch. Ostertag, G. H. Fecher and G. Schönhense, Surf. Sci.**352** (1996) 123.

[18] G. Schönhense, C. Westphal, J. Bansmann and M. Getzlaff, Europhys. Lett. **17** (1992) 727.

[19] H. Daimon, T. Nakatani, S. Imada, S. Suga, Y. Kagoshima and T. Miyahara, Jpn. J. Appl. Phys. **32** (1993) L1480.

[20] R. D. Ramsier and J. T. Yates, Jr., Surf. Sci.Rep. **121** (1991) 243.

[21] V. Rehn and R. A. Rosenberg, *Synchrotron Radiation Research: Advances in Surface and Interface Science, Volume 1: Techniques,* edited by R. Z. Bachrach., Plenum Press, New York (1992) 327.

[22] D. Menzel and R. Gomer, J. Chem. Phys. **41** (1964) 3311. P. A. Redhead, Can. J. Phys. **42** (1964) 886.

[23] P. R. Antoniewicz, Phys. Rev.**B21** (1980) 3811.

[24] M. L. Knotek and P. J. Feibelman, Phys. Rev. Lett.**40** (1978) 964.

[25] R. Franchy and D. Menzel, Phys. Rev. Lett.**43** (1979) 865.

[26] D. E. Ramaker, C. T. White and J. S. Murday, Phys. Lett. **A89** (1982) 211.

[27] K. Mochiji, I. Ochiai, S. Yamamoto and S. Takatani, Surf. Sci.**311** (1994) L677.

[28] N. Ueno, K. Kamiya, Y. Harada, M. C. K. Tinone, T. Sekitani and K. Tanaka, Optoelectron., Devices Technol. **11** (1996) 91.

[29] K. Mase, M. Nagasono, S. Tanaka, T. Urisu and S. Nagaoka, Surf. Sci.**377-379** (1997) 376.

[30] R. Jaeger, J. Stöhr and t. Kendelewicz, Phys. Rev.**B28** (1983) 1145.

[31] Z. C. Ying and W. Ho, J. Chem. Phys. **93** (1990) 9089.

[32] C. Paulsen-Boaz, W. L. O'Brien and T. Rhodin, J. Vac. Sci. Technol. **B10** (1992) 216. T. N. Rhodin, C. Paulsen-Boaz and W. L. O'Brien, Surf. Sci.**283** (1993) 109.

[33] W. L. Clinton, Phys. Rev. Lett.**39** (1977) 965. W. L. Clinton, M. A. Esrick and W. S. Sacks, Phys. Rev.**B31** (1985) 7550.

[34] Z. Misković, J. Vukanić and T. E. Madey, Surf. Sci.**169** (1986) 405.

[35] H. Nishikawa, M. Kanai, T. Kawai and S. Kawai, Jpn. J. Appl. Phys. **33** (1994) L1090.

[36] J. Solis, F. Vega, C. N. Afonso, E. Georgiou, D. Charalambidis and C. Fotakis, J. Appl. Phys. **74** (1993) 4271.

[37] K. Mase, S. Mizuno, M. Yamada, I. Doi, T. Katsumi, S. Watanabe, Y. Achiba and Y. Murata, J. Chem. Phys. **91** (1989) 590.

Chapter 3

CDAD of photoelectron from Si(001) valence band

3.1 Backgrounds

Recently, photoelectron spectroscopy using circularly polarized light has attracted much attention because it can provide new electronic and structural information of solid. One interesting phenomenon is circular dichroism in angular distribution (CDAD) of photoelectrons which is an asymmetry of photoelectron angular distribution (PEAD) observed by the incidence of left and right circularly polarized (LCP and RCP, respectively) light. CDAD of photoelectrons on non-magnetic and non-chiral materials is expected only by using "chiral" experimental geometry shown in Fig.2-12(a). Schönhense *et al.*[1] has reported CDAD for the first time on graphite using this chiral geometry. Using photon energies of 20–40eV, they found strong CDAD from π–band along $\bar{\Gamma}$ -$\bar{\mathrm{M}}$ line. They explained this CDAD using dipole transition model from atomic p_z orbital.

The CDAD using "non-chiral" geometry shown in Fig.2-12(b) was found for the first time by Daimon *et al.*[2] in 2D measurement in core-level excitation of Si(001) surface with photons in XPS region. This new type CDAD was explained by the rotation of the forward focusing peaks due to the angular momentum of outgoing photoelectrons. Multiple scattering calculation by Kaduwela *et al.*[3] well reproduced the experimental results quantitatively. Rennert *et al.*[4] derived relations for the total intensity and the dichroism in accordance with the symmetry of Si(001) surface. Their calculation also showed a good correspondence with the experimental results.

These experimental and theoretical CDAD have no relation to the magnetic circular dichroism (MCD), since the contribution from both Si $2p_{1/2}$ and $2p_{3/2}$ states, which are derived from spin-orbit interaction, were considered together.

On the other hand, two-dimensional (2D) CDAD in valence band excitation with photons in UPS region has been predicted using "non-chiral" geometry by Matsushita *et al.* on 1T-TaS_2[5]. They employed free-electron-like final state in their calculation. 2D CDAD was also calculated by Solterbeck *et al.* on Si(001) surface based on highly accurate one-

step model[6]. Their method considered multiple scattering of photoelectrons which is important as a final state effect in this energy region.

One purpose of this chapter is to study the origin of 2D CDAD of the photoelectron from Si(001) valence band. The experimental results are interpreted based on a general expression of PEAD in eq.(2.24) which does not include any scattering effects of the photoelectron. Next, the results are compared with the calculation by highly accurate one-step model which includes photoelectron diffraction effects.

Osterwalder *et al.*[7] have reported the photoelectron diffraction effect in the angular distribution of the photoelectron from energy-integrated valence band with the kinetic energies of $\geq$1000eV and several tens of eV. They suggested that PEAD patterns in these high and low $E_{\rm K}$ regions are very similar to those from near-lying core level and that from the atomic orbital constituting the valence band, respectively, with considering scattering effects in the final state. Another purpose of this chapter is to investigate such a scattering effect in 2D CDAD by comparing those in the XPS and UPS regimes.

3.2 Experimental procedure

In general, the strength of photoelectron diffraction effect depends on the kinetic energy of the photoelectron. To investigate such a dependence as well as CDAD itself, the experiment was performed using synchrotron radiation in XPS region at beamline NE-1B of Accumulation Ring and UPS region at beamline 28A (in helical undulator mode) of Photon Factory at High Energy Accelerator Research Organization in Tsukuba. A chamber equipped with a display-type spherical mirror analyzer [8] was attached to the end of the beamline. All the measurements were done using this analyzer in Ultra-High Vacuum (UHV) at room temperature.

The circularly polarized light in XPS ($\sim$250eV) and UPS (20eV$-$90eV) region was incident perpendicular to the Si(001) surface. Here, circular polarity is defined by the rotation direction of the polarization vector ($\hat{\varepsilon}$) on the sample surface, i.e., $\hat{\varepsilon}$ of LCP and RCP light rotates counterclockwise (CCW) and clockwise(CW) on the sample viewed from the light source, respectively. This experimental geometry has been already introduced in Fig.2-12.

The sample was Si(001) wafer (n-type, 2-3Ωcm) cut into a size of $15\times3\times0.5$mm^3. The clean surface was obtained by the repetition of resistive heating up to 1250C$^\circ$ for several seconds. After that, 2×1 double domain LEED pattern was observed.

In the measurement of photoelectron, the acceptance angle was almost $\pm45^\circ$ from the normal direction of the sample surface. The energy and the angular resolutions were about 1% of the kinetic energy and $\pm2^\circ$, respectively.

Photoelectron Angular Distribution (PEAD) was obtained at kinetic energy of 246eV in XPS region, while in UPS region it was obtained at several binding energies relative to the valence band maximum (VBM). The angle-integrated valence band spectrum at hν = 40eV

is shown in Fig.3.1 in which the binding energies to measure PEAD are noted. Here, VBM lying at 1.9eV above the bulk peak[9] was determined from the spectrum obtained at hν=21.2eV. The photoelectron was collected in constant final state spectroscopy (CFS) mode. The final state energies were 40eV and 80eV from VBM to compare with the theoretical work. At each photon energy in CFS mode, the gap value of the insertion device was chosen to maximize the degree of circular polarization.

3.3 Results and discussion

3.3.1 UPS region

$E_{\rm f}$=40eV

Figures 3.2(a) to (e) show PEAD from the valence band at the binding energies of (a)0.8eV, (b)1.4eV, (c)1.9eV, (d)3.0eV and (e)4.5eV, respectively. Upper and lower panels are for the LCP and RCP light, respectively. The lack of the intensity around the upper right corner of RCP images, especially in (e), is due to the shade of the electron gun which is mounted inside the analyzer.

In the figures, we can evidently see CDAD, but the characteristic features are completely different from those observed in the XPS regime as shown later. In Figs.3.2(a) to (c), intense areas on the left and right sides denoted as A in (a) rotate CCW for LCP and CW for RCP light from the $\bar{\Gamma}$ –$\bar{\rm J}'$ line, while those at the top and the bottom denoted as B in (b) show opposite rotational direction from the $\bar{\Gamma}$ –$\bar{\rm J}$ line. In Fig.3.2(b), the peak denoted as C which has opposite rotational direction to B is also observed. Intensity distributions around the four $\bar{\rm K}$ points of the two polarization images in Figs.3.2(d) and (e), which are denoted as F and G in (d), seem to be realized by mirror symmetry operation with respect to the $\bar{\Gamma}$ –$\bar{\rm J}$ line. Note that CDAD scarcely appears along the $\bar{\Gamma}$ –$\bar{\rm J}$ and the $\bar{\Gamma}$ –$\bar{\rm J}'$ lines of each image. This is not contradictory to the experimental "non-chiral" geometry along these high symmetry lines which are included in the mirror plane of Si(001) surface[4].

In (a) and (b), PEADs seem to have two-fold rotational symmetry despite of double domain 2×1 surface. This implies that a spatial part of the surface might be single domain. It is not unreal considering relatively small spot size of the incident light on the sample in the present experiment than that of the electron in LEED observation. Another possibility is a slight contribution from the remained linear polarity of the incident light due to the optics of vertical dispersion. If the initial state had p_z character, the intensity along the vertical central line in the PEAD would be weak as described in chapter 2.

From the general expression of PEAD as a function of the direction $(\theta_{\vec{k}}, \phi_{\vec{k}})$, we have already shown the equation (2.24) in chapter 2 including the distributions of 1D-DOS, $|M_A|^2$ and $|M_C|^2$, which are the three factors contributing to PEAD.

Figures 3.3(a) to (e) show the distributions of bulk 1D-DOS corresponding to Figs.3.2(a) to (e), respectively. Most of the intensity distributions in Fig.3.2 are considered to be con-

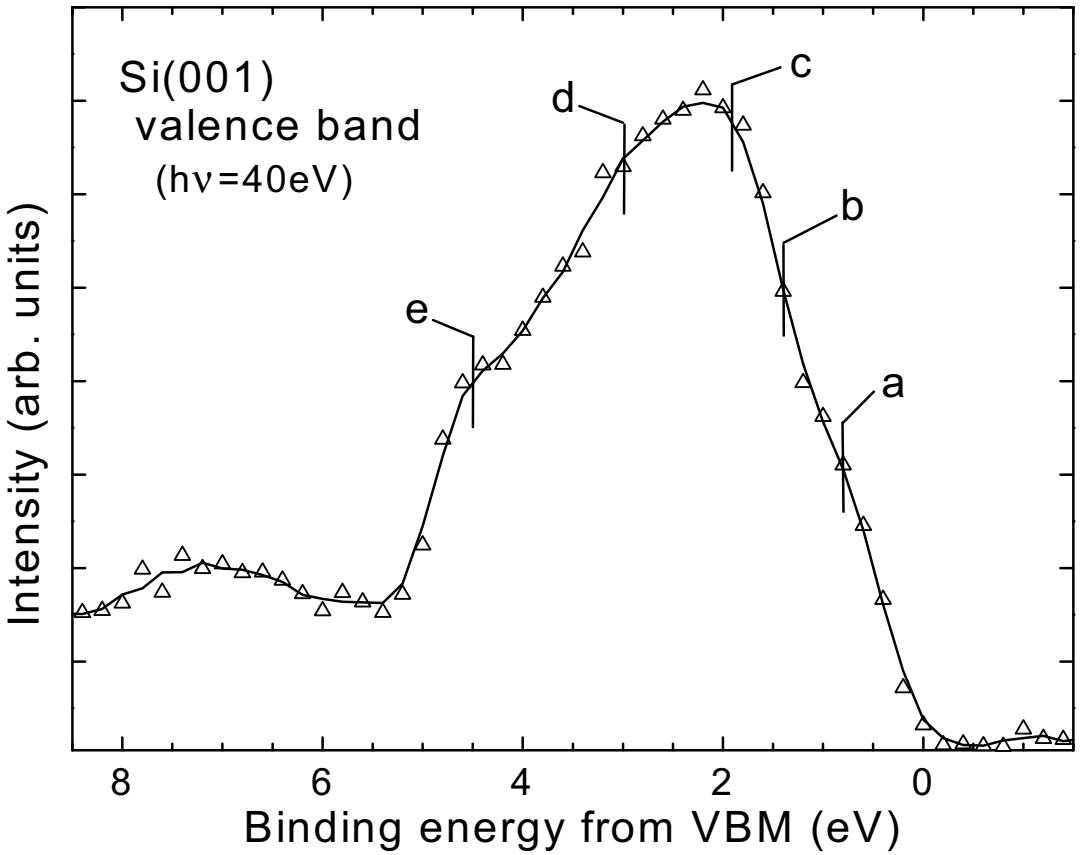

Figure 3.1 Angle-integrated spectrum of Si(001) valence band at hν=40eV. The origin of the binding energy is the valence band maximum (VBM). Binding energies of a: 0.8eV, b: 1.4eV, c: 1.9eV, d: 3.0eV, e: 4.5eV are the initial state energies at which PEAD measurement has been carried out in CFS mode with the final state energy of 40eV.

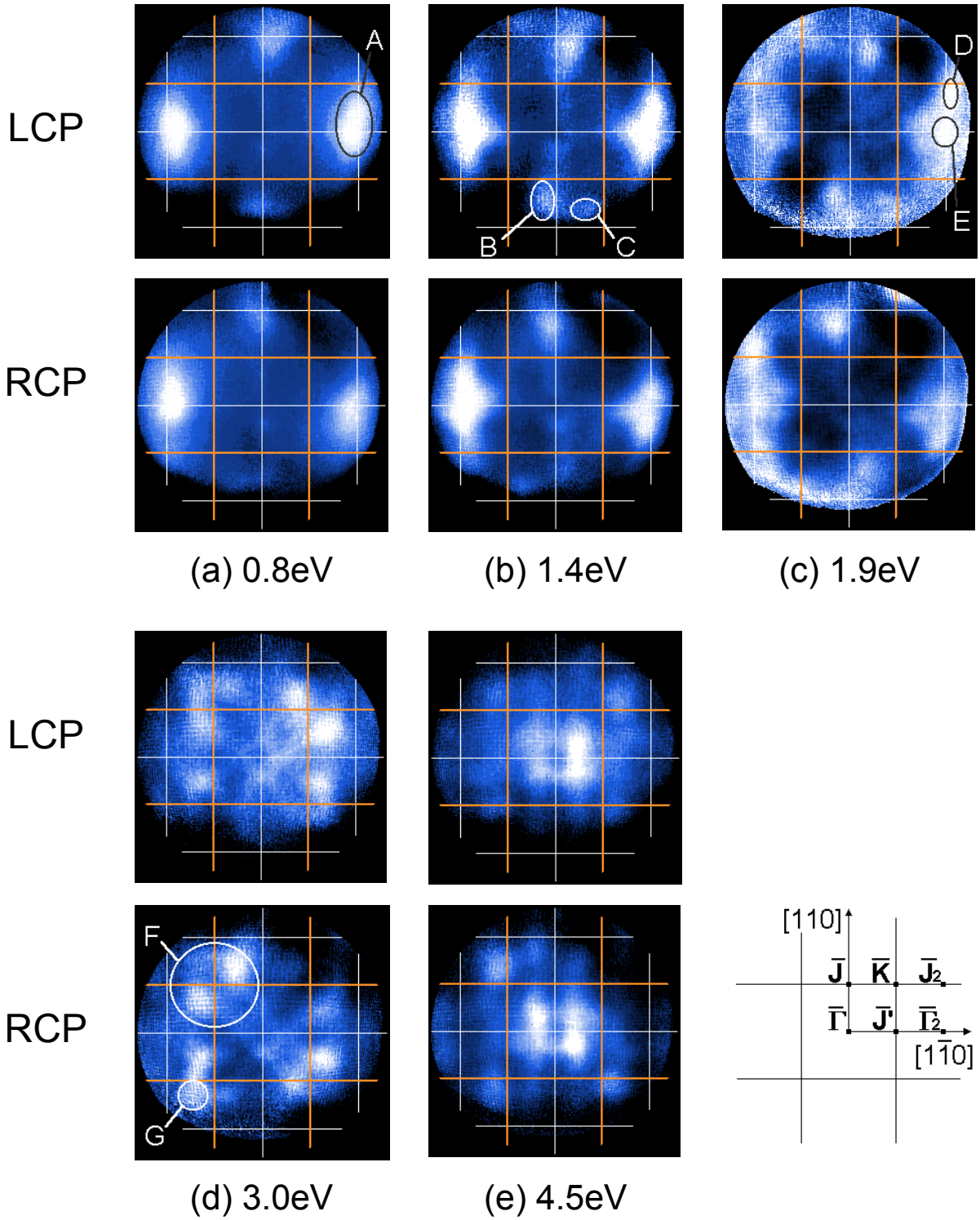

Figure 3.2 2D PEAD for LCP (upper) and RCP (lower) light. The binding energies are; (a) 0.8eV, (b) 1.4eV, (c) 1.9eV, (d) 3.0eV, (e) 4.5eV with respect to VBM. White and orange lines represent the 1×1 reciprocal lattice and 1×1 Brillouin zones, respectively. $\bar{\Gamma}$ - $\bar{J}'$ - $\bar{\Gamma}_2$ direction corresponds to $[1\bar{1}0]$ direction, which is *x*-axis.

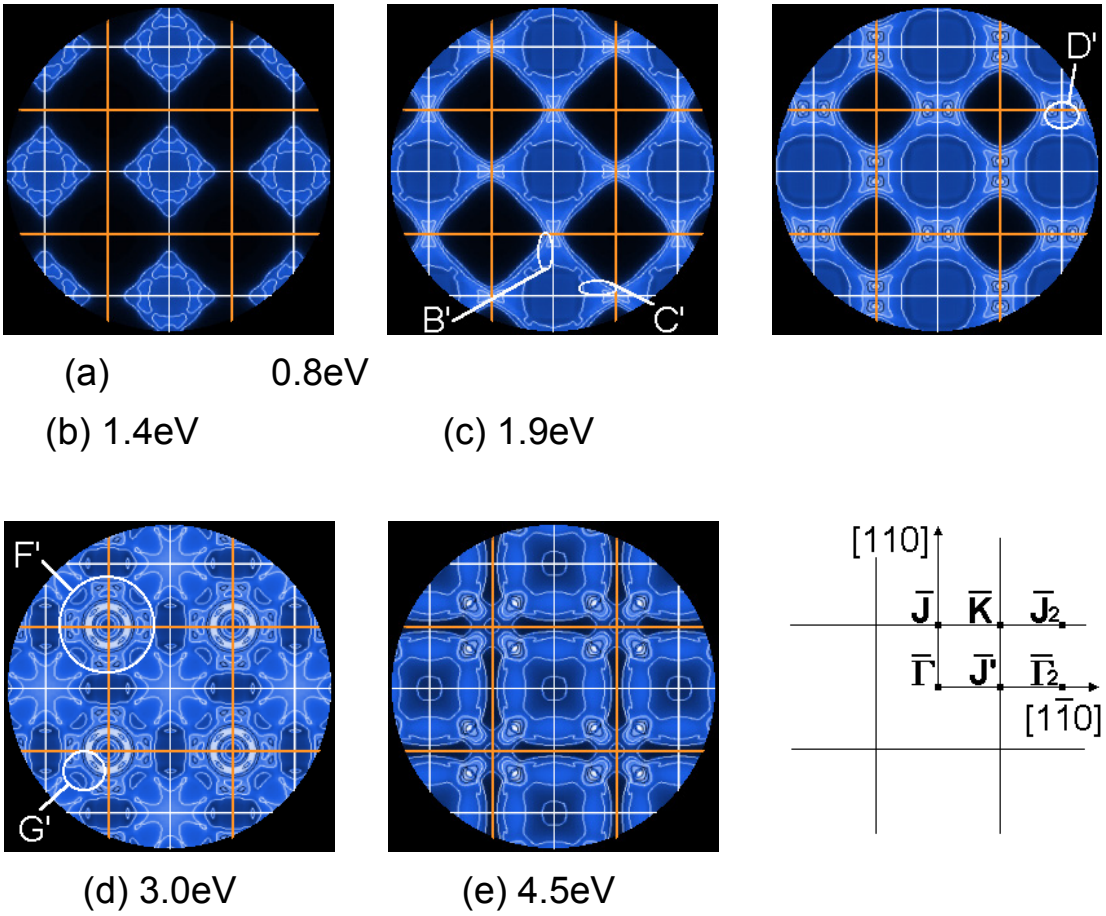

Figure 3.3 1D-DOS distributions at the same binding energies as in Fig.3-2. The white and orange lines are the reciprocal lattice and Brillouin zones of 1×1 unit, respectively. Bright area represents a high density of states.

tributed by bulk photoelectron since most of them occupy the area of bulk 1D-DOS projection shown in Fig.3.3. No distinct evidence of the surface states was observed which should lie in the bulk band gap area. The main features of observed distributions are qualitatively similar to the corresponding 1D-DOS around the $\bar{\Gamma}_2$ points of 2nd Brillouin zones (BZ) in (a) and (b), $\bar{\Gamma}_2$ and $\bar{\mathrm{J}}_2$ points in (c), $\bar{\mathrm{K}}$ points in (d) and (e), respectively. This suggests that the 1D-DOS in eq.(2.24) is reflected to the angular distribution. With regard to (b), B$'$ and C$'$ correspond to B and C in Fig.3.2(b), respectively. In the 1D-DOS, the latter has p_y character, while the former has p_x character. The most intense areas on the left and right sides of Figs.3.2(a) to (c), one of which is denoted as A in (a), are considered to be divided into two parts denoted as D and E in (c). D correspond to D$'$ in Fig.3.3(c) which consist of p_x orbital. In Fig.3.2(c), E seems to sit in almost the same position in the image of opposite polarization, while D seems to rotate CW when the polarity changes from LCP to RCP. Hence, the observed CDAD in A in (a) is presumed to be the contribution from D. The initial state of F and G in Fig.3.2(d) is considered to be contributed from p_x, p_y and p_z orbitals as well as s orbital judging from the corresponding area F$'$ and G$'$ in Fig.3.3(d). The intensity in the first and the third BZs are diminished in Figs.3.2(a), (b) and (c) while that in the second BZs are weak in (e). This kind of feature is characteristic to $|M_C|^2$, hence it could be explained by the photoemission structure factor.

The origin of CDAD Comparing Fig.3.2(b) and Fig.3.3(b) again, one can realize that there are some regions in PEAD where the high 1D-DOS such as B$'$ and C$'$ is not revealed. The observed CDAD seems to be ruled by the angular distribution of $|M_A|^2$. As already mentioned in chapter 2, $|M_A|^2$ is unique to each atomic orbital, which contributes to the LCAO initial state as a base function. $|M_A|^2$ is given by the equations (2.29) and (2.30) for the initial state with s other characters, respectively. Note that eq.(2.30) includes the interference between the $l-1$ and $l+1$ waves. As for $3p_x$, $3p_y$ and $3p_z$ orbitals, which constitute Si(001) valence band together with $3s$ orbital, $X_{l\pm1,\xi}$ in eq.(2.30) are written as

$$X_{l-1,\xi} = 2\sqrt{\frac{\pi}{3}}R_s\epsilon_{x,y,z} \qquad \text{for } \xi = 3p_{x,y,z} \tag{3.1}$$

$$X_{l+1,3p_x} = -2\sqrt{\frac{\pi}{3}}R_d\{(3x^2-r^2)\epsilon_x + 3xy\epsilon_y + 3zx\epsilon_z\}r^{-2} \tag{3.2}$$

$$X_{l+1,3p_y} = -2\sqrt{\frac{\pi}{3}}R_d\{3xy\epsilon_x + (3y^2-r^2)\epsilon_y + 3zx\epsilon_z\}r^{-2} \tag{3.3}$$

$$X_{l+1,3p_z} = -2\sqrt{\frac{\pi}{3}}R_d\{3zx\epsilon_x + 3yz\epsilon_y + (3z^2-r^2)\epsilon_z\}r^{-2} \tag{3.4}$$

where R_s and R_d are the radial matrix elements for the s and d orbitals, and $\epsilon_x, \epsilon_y, \epsilon_z$ are x, y, z components of $\hat{\epsilon}$. For circularly polarized light ($\hat{\epsilon} = (1, \pm i, 0)/\sqrt{2}$), $|M_A|^2$ is expanded as

$$|M_A|^2 = V + W \tag{3.5}$$

$$V \equiv |X_{l-1,\xi}|^2 + |X_{l+1,\xi}|^2 + 2Re[X_{l-1,\xi}]Re[X_{l+1,\xi}]\cos\theta \tag{3.6}$$

$$W \equiv -2Re[X_{l-1,\xi}]Im[X_{l+1,\xi}]\sin\theta \quad (\theta = \delta_{l+1} - \delta_{l-1}) \tag{3.7}$$

The calculated distribution of the term V in eq.(3.6) in the case of $3p_x$ initial orbital is shown in Fig.3.4(a). Here, x axis corresponds to the horizontal axis of each image. $R_{l\pm1}$ and $\delta_{l\pm1}$, which are the incident photon energy dependent values, are quoted from Ref.[10]. This term V does not show CDAD. One can recognize that it is the other term W which changes the sign with the polarity of the light as previously predicted in Refs.[1, 5]. Hence, this term W (CDAD term) is the origin of CDAD in dipole transition, which represents the interference between the two final state waves, $l-1$ and $l+1$. Note that this interference has no relation to the path difference since the surface effects are neglected. The distributions of the term W are shown in Figs.3.4(d) for LCP and (e) for RCP. The situation is similar for $3p_y$ initial orbital, but CDAD does not appear in the case of $3p_z$ and $3s$ orbitals. The terms V for $3p_y$ and $3p_z$, and W(LCP) for $3p_y$ are also shown in Figs.3.4(b), (c) and (f), respectively. In Figs.3.4(g) to (i), the total $|M_A|^2$ angular distributions from each p orbital are presented for LCP light. Note that (g) = (a) + (d). Because the CDAD term W (d) is strong at upper right and lower left corners, the total calculated intensity (g) (V+W) shows the intensity distribution as W (d) modified by V (a). Therefore, in the upper half of (g), the intensity at the right is stronger than that at the left, while in the right half of (g), the upper part is stronger than the lower part. This behavior is the same as that observed in the experimental results shown in the upper panels of Figs.3.2(a) to (c), especially for the distributions denoted as B in (b) and D in (c). The contribution from the $3p_y$ orbital may be also observed since the peak C in (b) exists in the region where $|M_A|^2$ ($3p_x$) is weak and also $|M_A|^2$ ($3p_y$) is strong. The assignments of B, D and C to p_x, p_x and p_y orbitals, respectively, correspond to the characters of B′, D′ and C′ in Fig.3.3(b) and (c). p_z character of these regions of B, D and C is denied because the p_z orbital does not exhibit CDAD itself as shown in Fig.3.4(i). In this way, we can distinguish the component atomic orbital of the initial states comparing the intensity difference among them with Figs.3.4(g), (h) and (i). Hence, we can determine the initial state symmetry using circularly polarized light.

In the case of higher binding energies in Figs.3.2(d) and (e), the p_x character seems to dominantly appear from the point of view that the intensities are strong in the upper right and lower left regions for the LCP light. Another feature is seen in Fig.3.2(d) in which the distribution G is apparent in the upper left and lower right regions for LCP light. These features suggest the initial state character of p_x and p_y, respectively. However, these assignment is contradictory to the actual character of these states as mentioned before, because s and p_z do not show CDAD as shown in Fig.3.4, and in the emission from p_x and p_y components, CDAD would be canceled if they were equally included. CDAD originated from the rotation of forward focusing peak, which was observed in the PEAD of core level photoemission[2], is not likely since G apparently reflects the band structure. The origin of CDAD in this binding energy region is still a matter of controversy.

Comparison with calculated PEAD [11] Figure 3.5 shows the calculated PEAD for LCP light based on highly accurate one-step model on 1×1 ideal surface[6]. The surface is

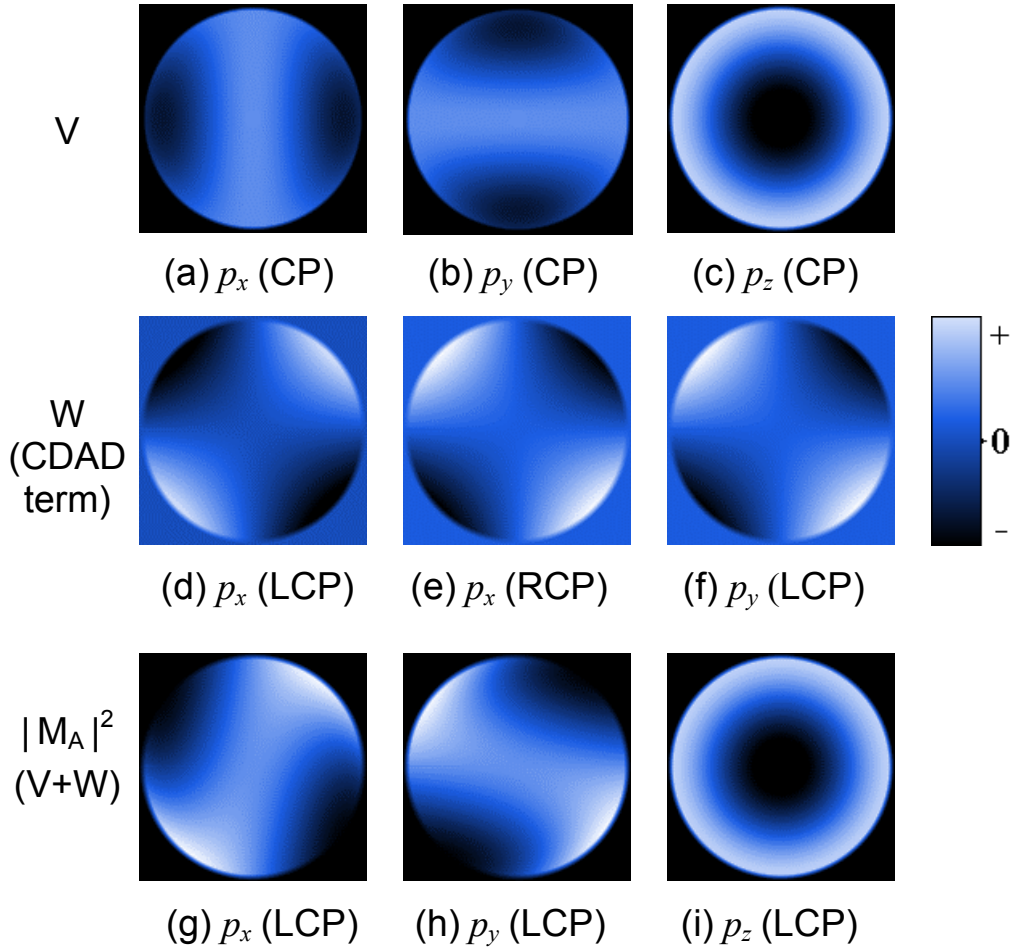

Figure 3.4 Calculated $|M_A|^2$ distributions with each components in eq.(3.5). The term V of eq.(3.6) for circularly polarized (CP) light, i.e., for both LCP and RCP light, and the total value of $|M_A|^2$ for LCP light are shown in (a), (b), (c), and (g), (h), (i), respectively. The initial atomic orbital is p_x for (a) and (g), p_y for (b) and (h), and p_z for (c) and (i). The CDAD term of eq.(3.7) for p_x orbital excited by LCP and RCP light are shown in (d) and (e), respectively, while (f) is that for p_y orbital excited by LCP light. The gray scale is only for (d), (e) and (f). Each image is for hν=40.8eV, and the circumference of the circle corresponds to $\theta_{\vec{k}} = 45°$.

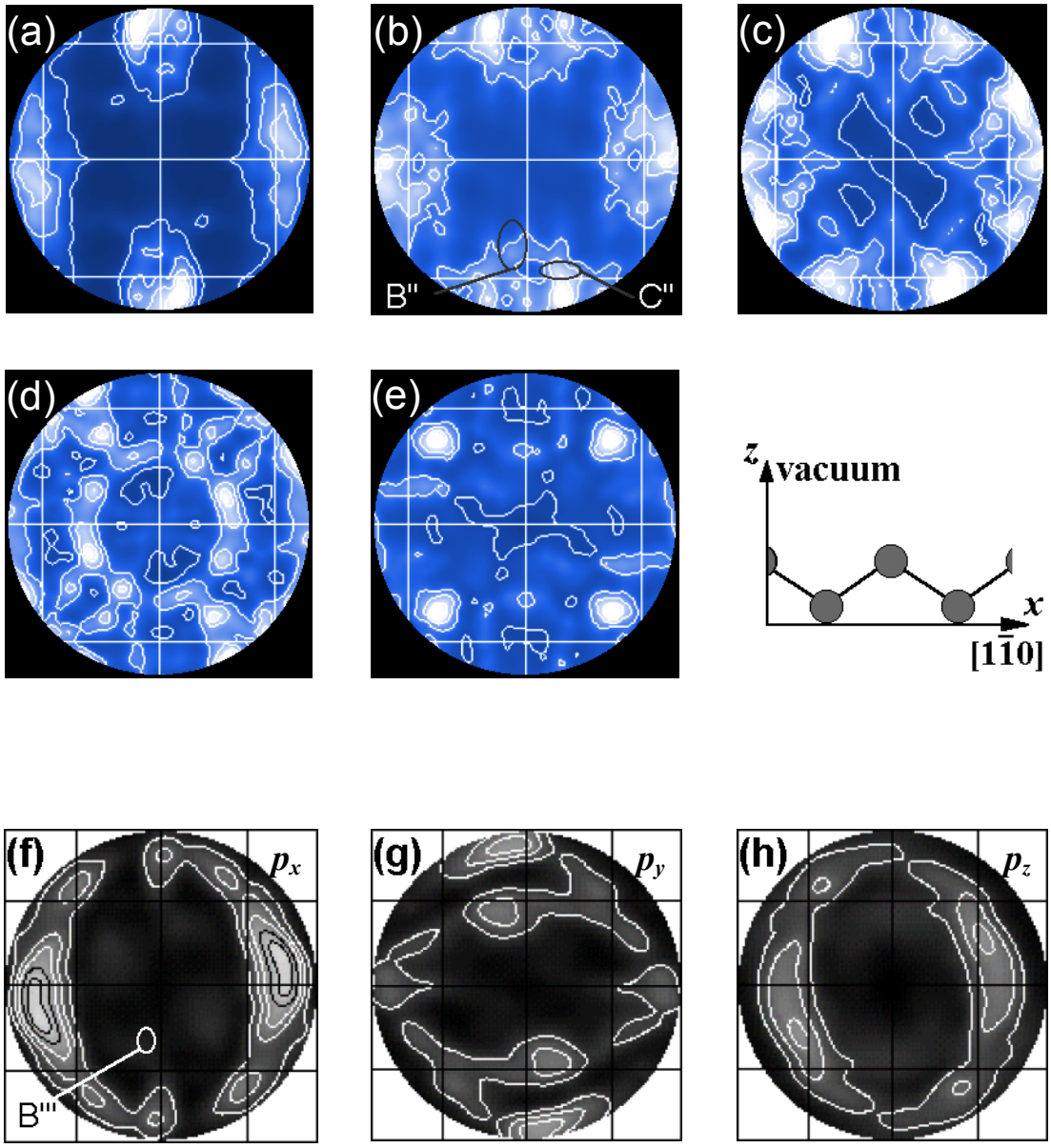

Figure 3.5 Calculated PEAD for LCP light from the ideal surface based on highly accurate one step model. The binding energies of (a) to (e) are the same as that in Figs.3-2(a) to (e), respectively. The matrix elements are also shown for the initial states which are the Bloch sums of p_x, p_y and p_z orbitals in (f), (g) and (h), respectively. The 1×1 reciprocal lattice is denoted by white and black lines in (a) to (e) and (f) to (h), respectively. Note that the included area is wider in the latter than that in the former.

single domain whose first atomic layer has zigzag chain along $[1\bar{1}0]$ (x-)direction as shown in the inset of the figure. The binding energies of (a) to (e) correspond to those in Figs.3.2(a) to (e), respectively. This one-step model[12] employs Green function as an initial state with layer orbital LCAO basis of the uppermost 4 atomic layers, and time-reversed LEED state as a final state so that the multiple scattering effect is considered. The angular distribution in each image show qualitatively good agreement with the corresponding experimental result. This suggests that the observed PEAD can be fully understood by considering photoelectron diffraction effect. However, there are some disagreements for the intensity ratio of the peak B″ and C″ in (a), (b) and (c). The intensity distribution of (e) is also different from Fig.3.2(e) which shows weaker intensities in the first BZ.

To discuss the inconsistency of the angular distributions in (a), (b) and (c), matrix elements ($|\langle f|\hat{\epsilon}\cdot\vec{r}\ |i\rangle|^2$) are considered whose initial states are the Bloch-sums of each atomic orbital within one atomic layer. The contribution from the topmost four layers are considered and the sum is shown in Figs.3.5(f) to (h) for LCP light. In the figure, the angular distribution of p_x (Fig.3.5(f)) as well as p_y (g) can reproduce the experimental results (Figs.3.2(a) to (c)) well, but the contribution from p_x seems to be too small in the region denoted as B‴ to realize the intense area of B in Fig.3.2(b). The intensity distribution in s (not shown here) and p_z indicates strong contribution from photoelectron diffraction since such azimuthal change seen in Fig.3.5(h) cannot occur in the dipole transition model as shown in Fig.3.4(i) for p_z. Considering these facts, the inconsistency between experiment and theory may be induced from the reconstruction on the actual surface, which results in either different photoelectron diffraction effects or different electronic structure.

E_{f}=80eV

Figures 3.6(a) to (d) show PEAD from valence band at binding energies of (a)1.4eV, (b)3.4eV, (c)4.4eV and (d)7.8eV, respectively. Left and right panels are for LCP and RCP light, respectively.

The obtained PEADs show CDAD again, but in a different manner compared to the cases in the final state energy of 40eV. The correspondence with 1D-DOS seems to be not so good. In Fig.3.6(a), however, the intense areas labeled A are observed only around $\bar{\Gamma}$ points of the third BZs which corresponds to 1D-DOS around $\bar{\Gamma}$ points as already presented in Fig.3.3(b). The relatively strong intensities in upper right and lower left regions in LCP image rotate CW resulting in RCP image. This feature is commonly observed in the other binding energies up to 7.8eV in (d), although the area with maximum intensity slightly moves towards the circumference of the image.

The intense area at $\bar{\Gamma}$ point of the third BZ in (a) seems to move towards $\bar{\mathrm{K}}$ point of the first BZ as the binding energy increases up to 4.4eV in (c). This movement is considered to reflect a dispersion from $\bar{\Gamma}$ to $\bar{\mathrm{K}}$ point, which is seen in 1D-DOS in Fig.3.3 as well as in a previous ARPES works[13]. The intensity distribution in the third BZ in Figs.3.6(b) and (c) show a reasonable agreement with 1D-DOS of similar binding energies in Figs.3.3(d)

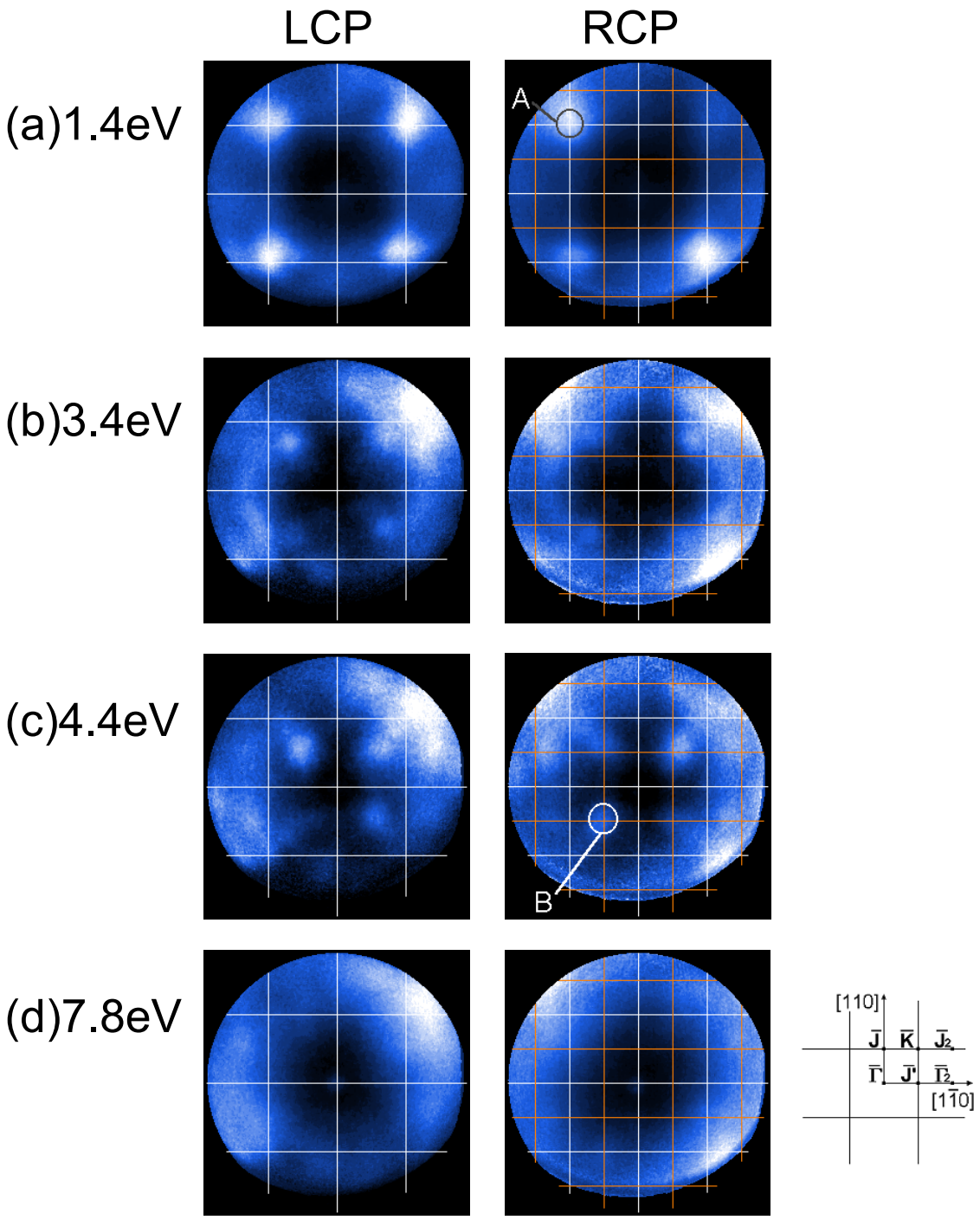

Figure 3.6 Observed 2D PEAD for LCP (left) and RCP (right) light with E_f=80eV. The binding energies are; (a)1.4eV, (b)3.4eV, (c)4.4eV and (d)7.8eV with respect to VBM. The areas surrounded by white and orange lines correspond to the 1×1 reciprocal lattice and Brillouin zone, respectively.

and (e), respectively. In Figs.3.6(b) and (c), the intense peak around $\bar{\mathrm{K}}$ points, one of which is labeled B, exhibit CDAD as a CW rotation of the relatively strong intensities in upper left and lower right by the polarization change from LCP to RCP.

From $|M_A|^2$ distributions in Fig.3.4, the dominant initial state symmetry of the observed areas A and B are expected to be assigned to p_x and p_y orbitals, respectively. (Note that $|M_A|^2$ show almost the same angular distributions by the incident photon energy of around 80eV.) But the actual 1D-DOS in these regions of A and B is the contribution from p_x, p_y, p_z and s orbitals, so that CDAD is not expected to appear because of the same reason as in the case of higher binding energies with E_{f} =40eV. The rotation of forward focusing peaks is not likely to contribute to CDAD since the observed intensity distributions apparently reflect 1D-DOS. The origin of CDAD at this final state energy is still a matter of controversy, and it is needed to compare the experimental results with the theoretical calculation which considers multiple scattering effect.

3.3.2 XPS region

Figure 3.7 shows PEAD from valence band at binding energy of ∼4eV from Fermi level. The kinetic energy of the photoelectron is 246eV and the horizontal axis corresponds to $[1\bar{1}0]$ direction. Upper and lower panels are for LCP and RCP light, respectively. Comparing these two panels, the existence of CDAD is obvious. There are bright intensity distributions which seem to rotate CCW(CW) from horizontal and vertical central lines for LCP(RCP) light. This feature is very similar to the previous CDAD investigations of the photoelectron from Si $2p$ core level as shown in Fig.3.8(a) whose kinetic energy is 250eV. The intensity distribution of the core level emission is explained by the rotation of forward focusing peaks due to the photoelectron with angular momentum, and the rotation angle $\Delta\phi$ is expressed as

$$\Delta\phi = m/k_{\parallel}R_{\parallel} \tag{3.8}$$

where m is the z-component of the angular momentum of the final state, $k_{\parallel}$ and $R_{\parallel}$ are the surface parallel components of the wave number of the photoelectron and the distance between the emitter and the scatterer atoms[2], respectively. In the case of emission from $2p$ core, $m = \pm 2$ are used for LCP and RCP light, respectively, since the transition to such states is dominant considering the Gaunt coefficient. According to this equation, the positions of the rotated forward focusing peaks are plotted by crossed signs in Fig.3.8(b) considering the expected forward focusing directions from the bulk Si emitter as shown in the inset of Fig.3.8 and 4-fold symmetry of the crystal. The reflection effect is also taken into account in these cross patterns assuming that the inner potential is 12eV[15]. In the figure the cross patterns well reproduce the rotation feature of the present result suggesting that this rotational feature is derived from the rotation of forward focusing peaks even if the initial state is delocalized.

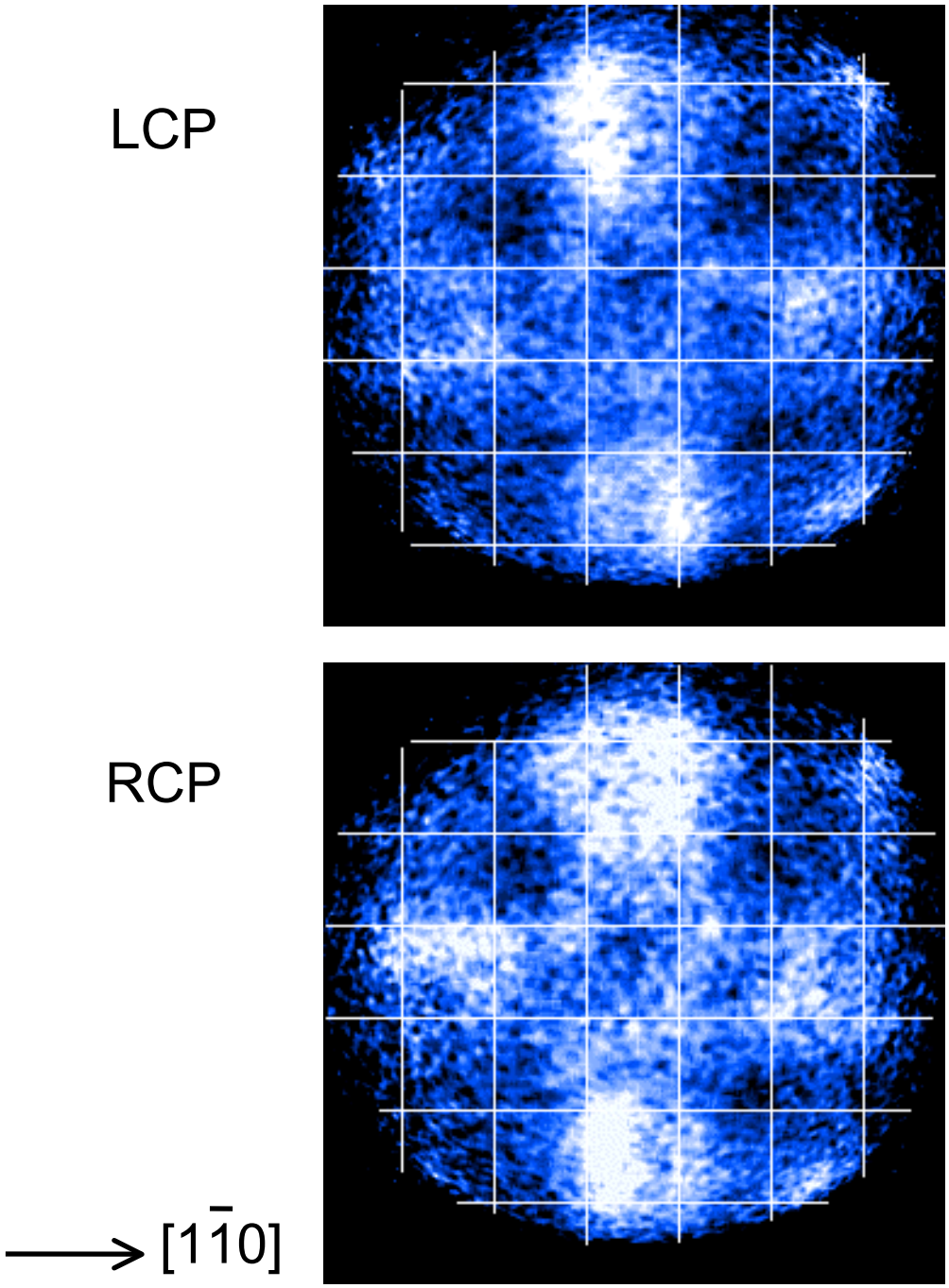

Figure 3.7 2D PEAD for LCP and RCP light in XPS region which shows CDAD. E_K of the photoelectron is 246eV which corresponds to the emission from Si(001) valence band mainly consists of 3*p* states. The horizontal axis is $[1\bar{1}0]$ direction. The mirror planes exist along horizontal and vertical central lines. The white lines represent 1×1 Brillouin zones.

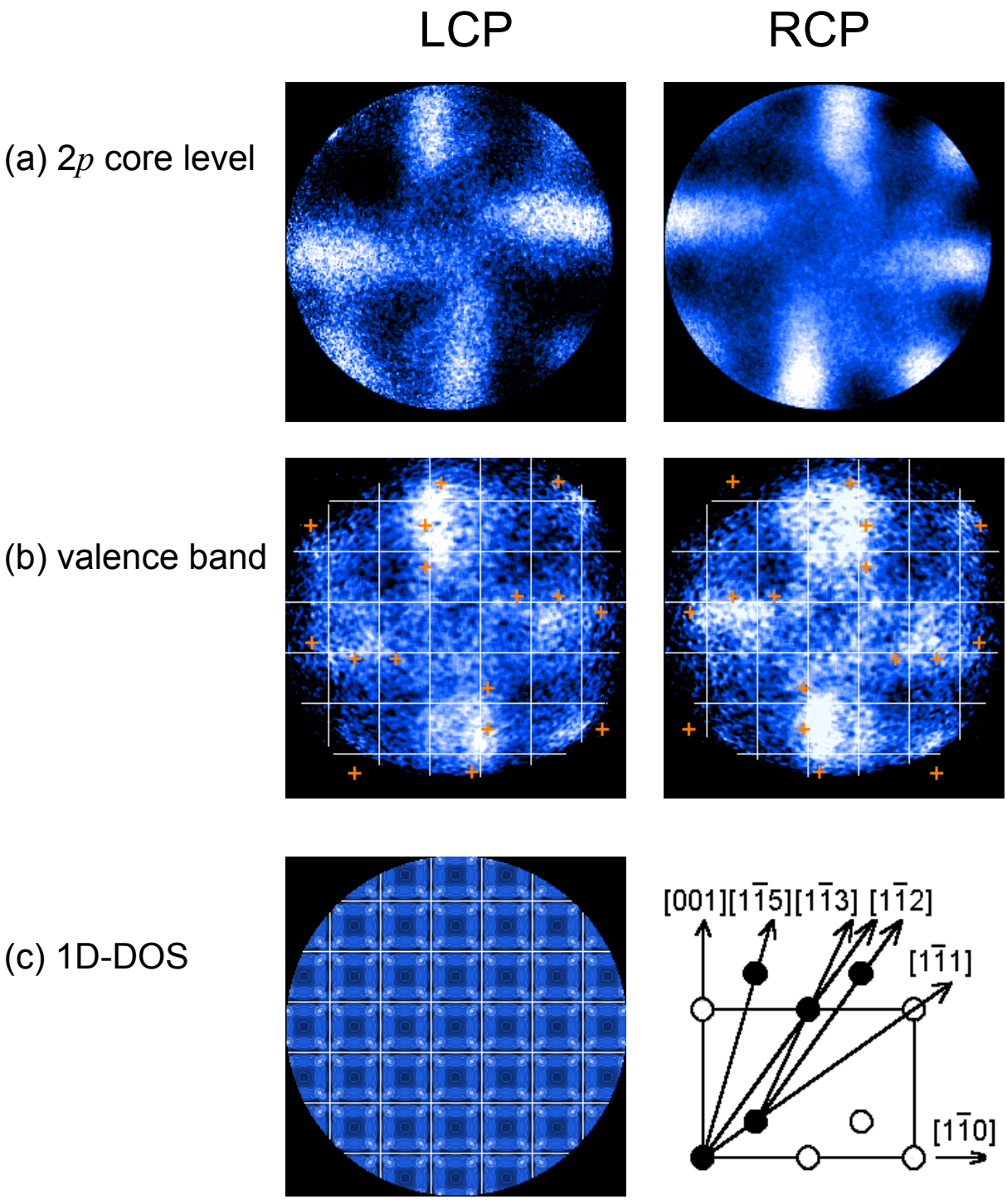

Figure 3.8 Comparison of present data (b) with previously obtained PEAD from 2*p* core (a) and calculated 1D-DOS (c). The cross sectional view of the crystal and the directions of forward focusing peaks to be appear in the case of core excitation are also shown. The rotated forward focusing peaks according to eq.(3.8) are plotted in (b) by orange crossed signs. 1×1 Brillouin zones are denoted by white lines in (b) and (c).

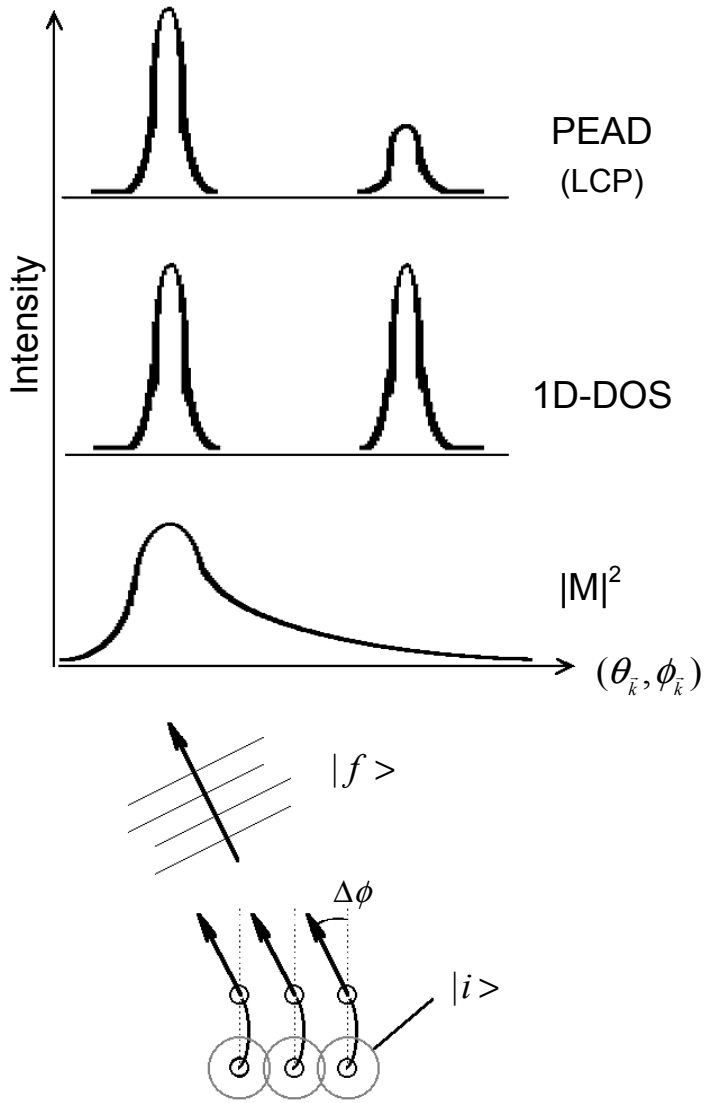

Figure 3.9 A schematic illustration of CDAD appeared in XPS region. The initial state is an atomic orbital at each site which is the base of LCAO description. When there is a scatterer in the direction of outgoing photoelectron, the forward focusing peak rotates resulting in the one-sided angular distribution of the transition matrix element $|M|^2$. Consequently, the contributions from both 1D-DOS and the rotation of forward focusing peak exist in PEAD, which is the product of 1D-DOS and $|M|^2$.

On the other hand, the experimental results have another feature that the intensity distribution exists around the circumference of 1×1 surface Brillouin zones which are represented by white lines in Fig.3.7. This distribution seems to be very similar to the 1D-DOS shown in Fig.3.8(c). $k_{\parallel}$ conservation by direct transition in this high kinetic energy region is possible considering a small wave number of incident photon (0.13Å^{-1}) compared to the size of 1×1 surface Brillouin zone(1.64Å^{-1}).

Therefore, the present result is attributed to the summation of intensity distributions due to not only the direct reflection of 1D-DOS but the rotation of forward focusing peaks. Figure 3.9 is a schematic drawing to understand this situation qualitatively. The initial state is described by LCAO approximation, but each photoelectron can be considered to have the angular momentum originated from each atomic orbital at each site which is the base of LCAO description and is p orbital in the present case. When there is a scatterer in the direction of outgoing photoelectron, the forward focusing direction rotates according to eq.(3.8). The final state far from the surface is considered to be the sum of photoelectron waves from each atomic site although the phase shift among each atomic orbital at different site has to be considered. Hence, the angular distribution of transition matrix element $|M|^2$ becomes one-sided. Since PEAD is the product of 1D-DOS and $|M|^2$ as already mentioned in chapter 2, the resulting angular intensity distribution in the present study seems to be the sum of both 1D-DOS and the rotation of forward focusing peaks.

3.4 Summary

The experimental investigation of 2D CDAD of the photoelectron from Si(001) valence band was presented for the first time at the final state energies of 40, 80 and 250eV. The obtained PEAD showed apparent CDAD at any final state energies and binding energies within the limits of measurement.

The angular distribution at the final state energy of 40eV was understood considering the contributions from one dimensional density of states (1D-DOS), photoemission structure factor ($|M_C|^2$) and matrix element of the direct transition from initial atomic orbital to the free electron-like final state($|M_A|^2$). The observed CDAD can be attributed to the interference of the final state waves in lower binding energies and a new way to determine the initial state symmetry by using circularly polarized light was proposed. Comparing the experimental PEAD with the distribution of $|M_A|^2$, contributions from $3p_x$ and $3p_y$ orbitals were distinguished at lower binding energies. The calculation by highly accurate one-step model showed quantitatively good agreement in the angular distribution except for the opposite intensity ratio of the top and the bottom peaks in lower binding energies. The calculation on the 2×1 reconstructed surface may resolve this inconsistency.

At the final state energy of 80eV, the angular distribution still reflects 1D-DOS although the correspondence was not better than in the case of 40eV. The origin of CDAD in this energy region is still a matter of controversy. The contribution from the forward focusing

peaks dominates PEAD at higher kinetic energy of the photoelectron, and CDAD by the rotation of forward focusing peaks was observed at the final state energy of 250eV with some contribution from 1D-DOS.

References

[1] G. Schönhense, C. Westphal, J. Bansmann and M. Getzlaff, Europhys. Lett. **17** (1992) 727.

[2] H. Daimon, T. Nakatani, S. Imada, S. Suga, Y. Kagoshima and T. Miyahara, Jpn. J. Appl. Phys. **32** (1993) L1480. H. Daimon, T. Nakatani, S. Imada and S. Suga, Rev. Sci. Instrum. **66** (1995) 1510. H. Daimon, T. Nakatani, S. Imada and S. Suga, J. Electron Spectrosc. Relat. Phenom.**76** (1995) 55.

[3] A. P. Kaduwela, H. Xiao, S. Thevuthasan, C. S. Fadley and M. A. Van Hove, Phys. Rev. **B52** (1995) 14927.

[4] P. Rennert, A. Chassé, T. Nakatani, K. Nakatsuji, H. Daimon and S. Suga, J. Phys. Soc. Jpn., **66** (1997) 396.

[5] T. Matsushita, H. Nishimoto, T. Okuda, T. Nakatani, H. Daimon, S. Suga, H. Namba, T. Ohta, Y. Kagoshima, T. Miyahara, J. Electron Spectrosc. Relat. Phenom. **78** (1996) 489. T. Matsushita, S. Imada, H. Daimon, T. Okuda, K. Yamaguchi, H. Miyagi and S. Suga, Phys. Rev.**B56** (1997) 7687.

[6] C.-H. Solterbeck, W. Schattke and C. S. Fadley, Surf. Sci. **357–358** (1996) 245.

[7] J. Osterwalder, A. Stuck, T. Greber, P. Aebi, L. Schlapbach and S. Hüfner, Proc. 10th Int. Conf. on VUV Rad. Phys. (1992) and references therein.

[8] H. Daimon and S. Ino, Rev. Sci. Instrum. **61** (1990) 57. H. Nishimoto, H. Daimon, S. Suga, Y. Tezuka, S. Ino, I. Kato, F. Zenitani and H. Soezima, Rev. Sci. Instrum. **64** (1993) 2857.

[9] H. W. Yeom, *Doctral thesis* (1996).

[10] S. M. Goldberg, C. S. Fadley and S. Kono, J. Electron Spectrosc. Relat. Phenom., **21** (1981) 285.

[11] All the 2D images of 1D-DOS in Fig.3.3, PEAD and matrix elements in Fig.3.5 are calculated by W. Schattke and C.-H. Solterbeck in their collaboration with us.

[12] W. Schattke, Progr. Surf. Sci. **54** (1997) 211.

[13] A. Goldmann, P. Koke and W. Mönch, G. Wolfgarten and J. Pollmann, Surf. Sci.**169** (1986) 438. P. Koke, A. Goldmann, W. Mönch, G. Wolfgarten and J. Pollmann, Surf. Sci.**152/153** (1985) 1001.

[14] H. Daimon, S. Imada, H. Nishimoto and S. Suga, J. Electron Spectrosc. Relat. Phenom., **76** (1995) 487.

[15] Y. Horio and A. Ichimiya, Surf. Sci.**133** (1983) 393.

Chapter 4

2D PES of Si(111)-$(\sqrt{3}\times\sqrt{3})$R30°-Ag surface

4.1 Backgrounds

The atomic and electronic structure of Si(111)-($\sqrt{3}\times\sqrt{3}$)R30°-Ag surface has been investigated through the past two decades by various methods[1]-[5]. Recent works have proposed a reliable atomic structure model called Honeycomb Chained Trimer (HCT) or HCT-1 model (originally proposed by Takahashi *et al.*[5]) by using ion scattering spectroscopy[6]. This model was supported by total-energy calculation[7]. The plan and side views of HCT model are shown in Fig.4.1(a)[6] which includes missing-top-layer Si(111) substrate. The $\sqrt{3}\times\sqrt{3}$ unit cell contains one Si- and one Ag-trimer, which indicates Ag coverage of 1ML and intrinsically semiconductive character of this surface. This model also contains a mirror plane along $[11\bar{2}]$ direction, which is denoted by a dashed line in the figure. A calculated band structure based on HCT model is shown in Fig.4.1(b)[8]. There are several occupied bands lying between Fermi level and the binding energy of 2eV, and a dispersive empty state band which has its minimum at around $\bar{\Gamma}$ point. It is this empty band which determines the position of Fermi level on the actual surface as will be explained later.

Honeycomb arrangement of protrusions was observed in either occupied or unoccupied state STM images[9, 10]. Fig.4.2(a) is an unoccupied-state STM image obtained at +1.2eV bias on the sample[10]. The relationship between this STM topography and HCT model was clearly solved by a theoretical work by Watanabe *et al.*[8]. They suggested that the observed protrusion in STM images represents neither Si nor Ag atom, but corresponds to the center of Ag triangle. This situation is illustrated in Fig.4.2(b).

The electronic structure of this surface has been investigated by several groups using ARPES[11, 12] and ARIPES[14]. Yokotsuka *et al.*[11] found three surface states which lie between Fermi level and binding energy of 4eV with $\sqrt{3}$ periodicity, using He discharged lamp with incident polar angle of 45° . Johansson *et al.*[12] studied ARPES using synchrotron radiation and suggested that there are two surface resonance states and one metallic surface state at around $\bar{\Gamma}$ point of the second $\sqrt{3}\times\sqrt{3}$ surface Brillouin zone (SBZ).

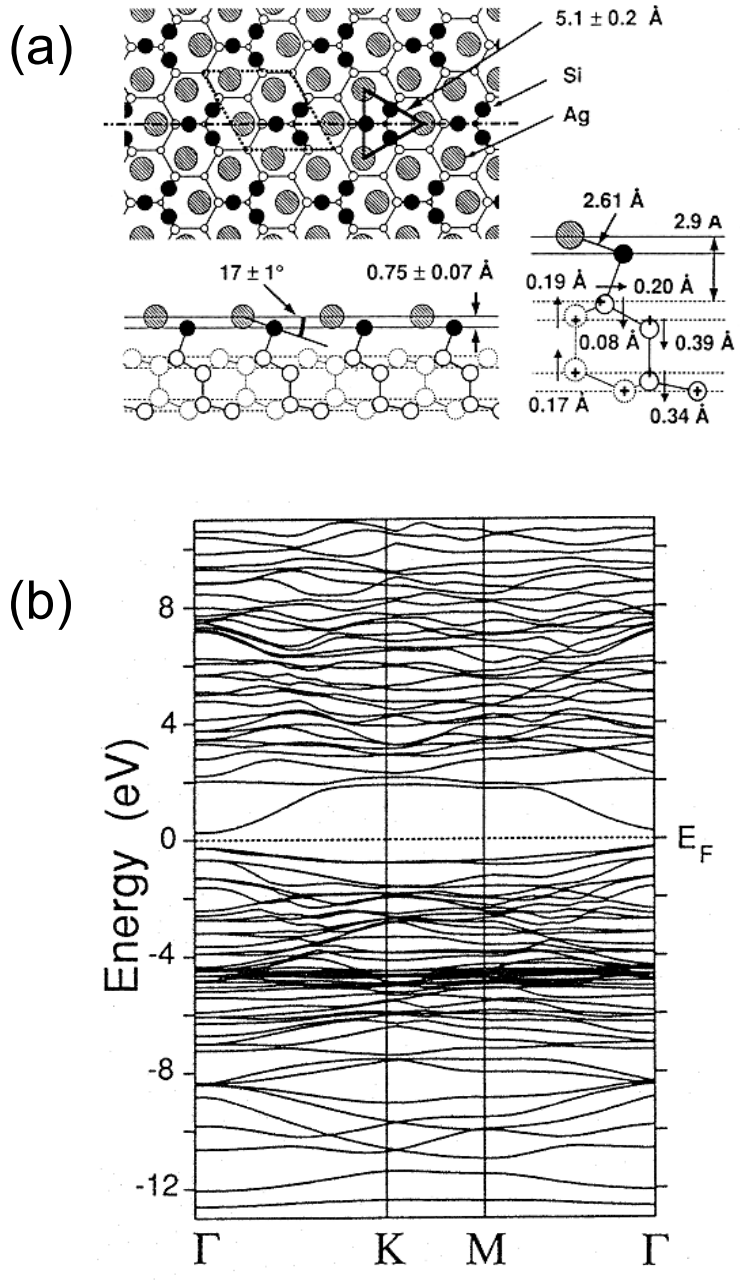

Figure 4.1 (a): Plan and side view of modified Honeycomb-Chained-Trimer (HCT) model (ref. [6]). (b): Band calculation based on HCT model by Watanabe *et al.*(ref. [8]). The lowest empty state band S_1 has its minimum at $\overline{\Gamma}$ point.

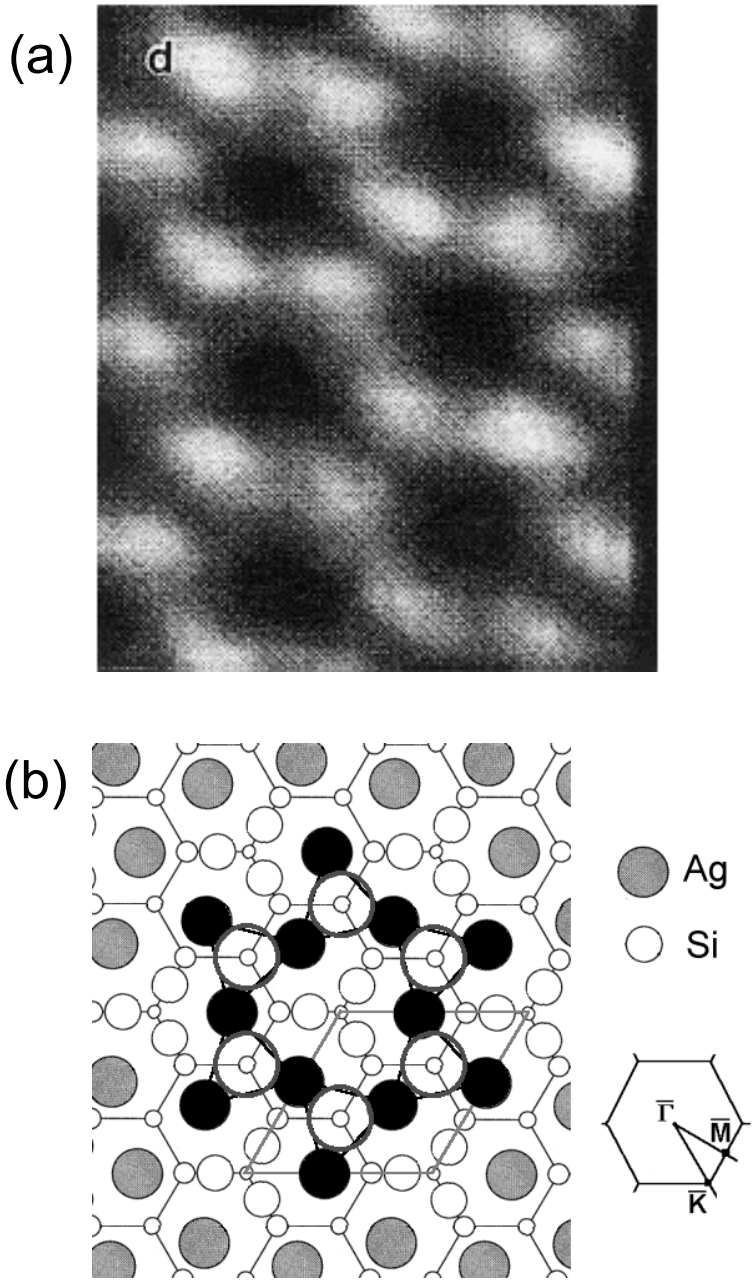

Figure 4.2 (a) Unoccupied state STM image of Si(111)-$\sqrt{3}\times\sqrt{3}$-Ag surface (Ref.[10]). Honeycomb structure of the bright spots is clearly seen. (b) The relationship between the STM image and HCT model. Black circles denote Ag atoms. Small triangles of these Ag atoms form distorted hexagon. Only the center of each triangle, where the density of state is large, is observed by STM which contributes to a "honeycomb" image in (a). A $\sqrt{3}\times\sqrt{3}$ unit cell is also indicated by the gray line.

Their result is shown in Fig.4.3 along two high symmetry lines. A metallic surface state S_1 and two surface resonances named S_2' and S_3' crossing each other at $\bar{K}$ point were observed. A strong p_z character of S_2' band was also suggested from the parity analysis using linearly polarized light. S_1 state was suggested to originate from a partially occupied empty state band which has been already introduced in Fig.4.1(b). This band was also observed in ARIPES measurment[14] as a prominent peak at around 2eV above Fermi level and a weak shoulder at around Fermi level at $\bar{\Gamma}$ point. Recently, high electrical conductance on this surface induced by small amount of additional noble metal atoms such as Ag and Au has attracted much attention[15]-[17]. S_1 state has been suggested to play an important role in the mechanism of such a high conductance[18].

In this chapter, the electronic structure of this surface is investigated by using 2D ARPES, and symmetries of the observed initial state bands are discussed. This is the first time to study surface states by 2D PES except for the pioneering work by Himpsel *et al.*[19].

4.2 Experimental procedure

The experiment was performed at beamline 4 of SOR-RING in ISSP of the University of Tokyo. The base pressure of UHV chamber was 1.3×10^{-10} Torr during the measurement.

The specimen was Si(111) (p-type, 10.5Ωcm) wafer cut into a size of $15\times3\times0.5\text{mm}^3$ which showed clear 7×7 LEED pattern after the cleaning by direct current resistive heating up to 1250C°. Ag was deposited onto the specimen whose temperature was maintained at ∼600C° until a clear $\sqrt{3}\times\sqrt{3}$ LEED pattern was observed.

All the measurements were done at room temperature using a display-type spherical mirror analyzer[20]. The energy resolution was estimated from the Fermi edge of Ta to be ±0.26eV and angle resolution was at most ±2° . The linearly polarized light was incident perpendicular to the surface with the photon energy of 32eV. Figure 4.4 is an angle integrated valence band spectrum which contains contribution from surface states and bulk states around binding energies (E_B) of 1.1eV and 2.6eV from Fermi level, respectively. The spectrum suggests a semiconductive character of this surface, although a very weak intensity is seen at around 0.1eV.

PEAD from valence band was measured at every 0.1eV from Fermi level to 1.7eV below it to cover whole contribution from surface states. The acceptance angle was about ±60° from surface normal, which enables detection of the photoelectron up to third SBZs.

In the measurement, two conditions in relationship between $\sqrt{3}\times\sqrt{3}$ surface Brillouin zone and the electric vector ($\hat{\epsilon}$) of the light were chosen; one is $\hat{\epsilon}$ ∥ $\bar{\Gamma}$ -$\bar{\text{M}}$ ($[01\bar{1}]$) and the other is $\hat{\epsilon}$ ∥ $\bar{\Gamma}$ -$\bar{\text{K}}$, which are called as $\phi = 0°$ and $\phi = 30°$ configurations in this thesis, respectively.

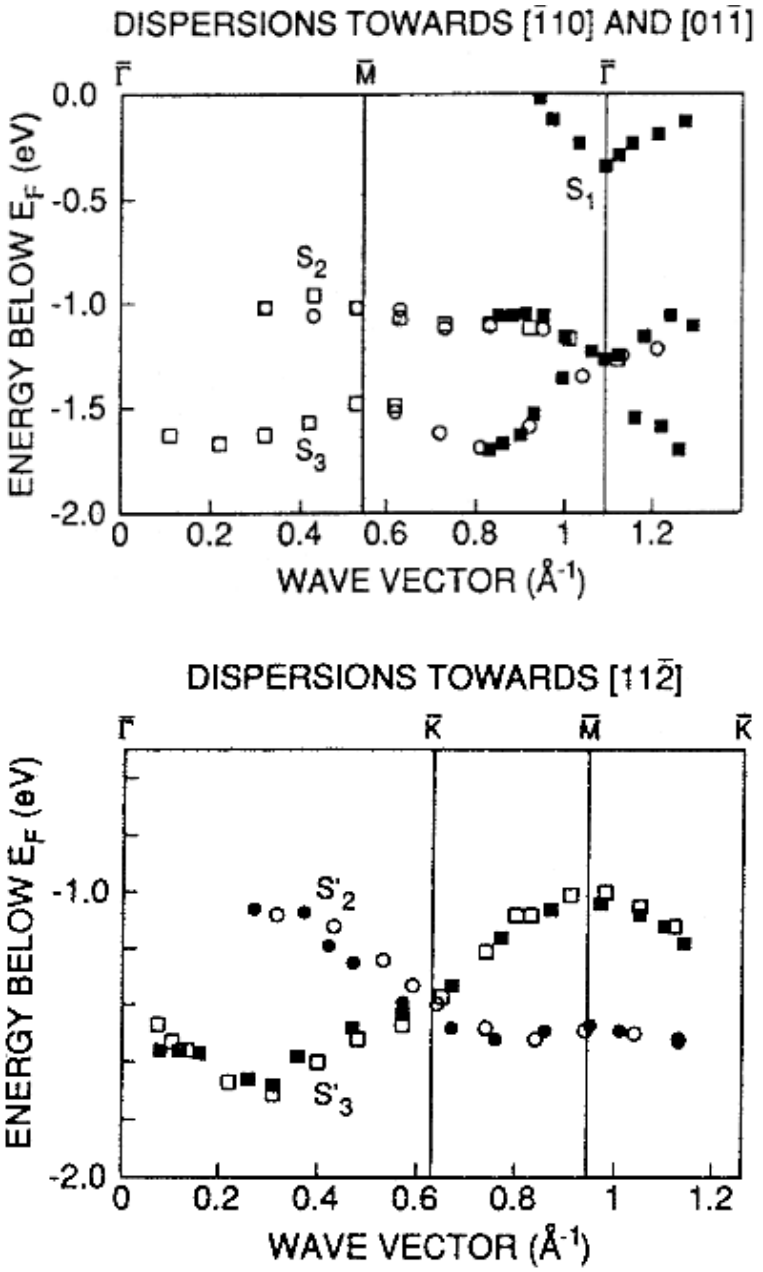

Figure 4.3 Previous work on the dispersion of Si(111)-$\sqrt{3}\times\sqrt{3}$-Ag surface by Johansson *et al.* (ref. [12]). Dispersions along $\overline{\Gamma}$ - $\overline{\mathrm{M}}$ and $\overline{\Gamma}$ - $\overline{\mathrm{K}}$ - $\overline{\mathrm{M}}$ high symmetry lines are presented in upper and lower panels, respectively.

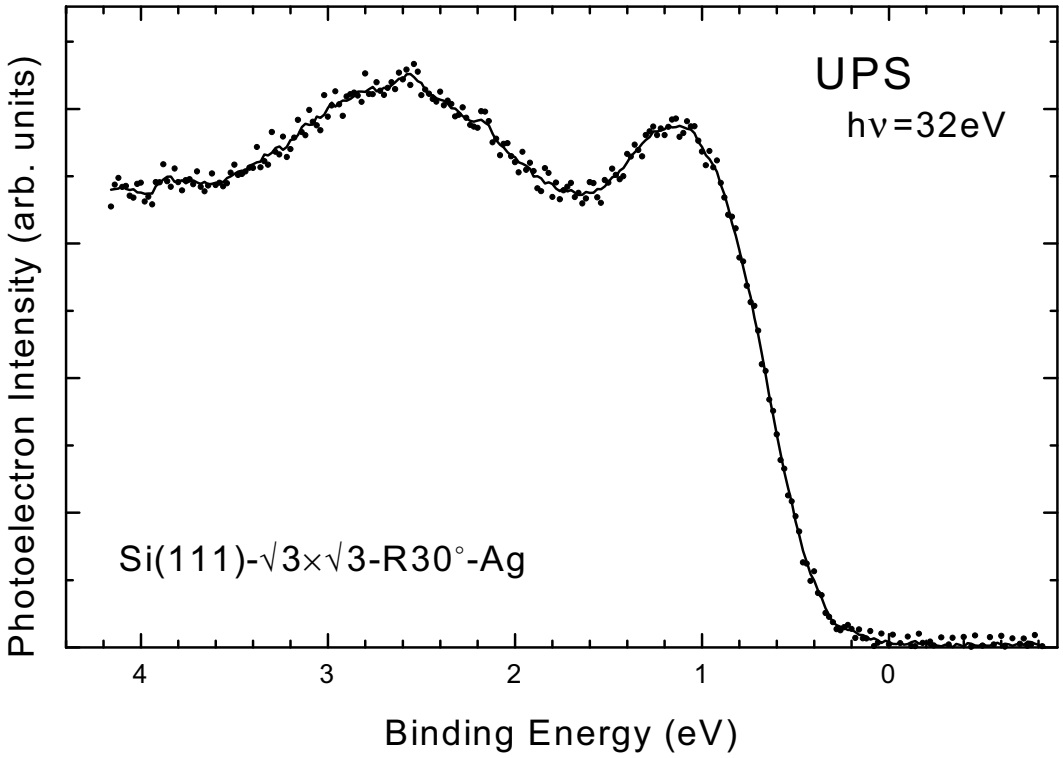

Figure 4.4 Angle integrated spectrum of Si(111)-√3×√3-R30º-Ag surface (hν=32eV). The peaks at around 1.1eV and 2.6eV correspond to bulk and surface components, respectively. Two-dimensional PEAD was obtained at each 0.1eV binding energy from Fermi level to 1.7eV.

4.3 Results and discussion

Figure 4.5 shows typical PEAD images observed at E_B =1.1eV. (a) was obtained in $\phi = 0°$ configuration, while (b) in $\phi = 30°$. The white lines in the figure represent $\sqrt{3} \times \sqrt{3}$ surface Brillouin zone (SBZ). High symmetry points in $\sqrt{3} \times \sqrt{3}$ SBZ are also shown at the bottom of each image, with directions of the polarization vector ($\hat{\epsilon}$) of the incident light.

In these images, one can recognize immediately that there is a mirror symmetry in the intensity distribution. The mirror symmetry is obvious along vertical and horizontal central line in $\phi = 0°$ and $\phi = 30°$ configurations, respectively. These directions include the $\bar{\Gamma}$ -$\bar{\mathrm{K}}$ line in SBZ, which suggests that the electronic states observed in these images have a mirror symmetry with respect to the $\bar{\Gamma}$ -$\bar{\mathrm{K}}$ direction. This feature was commonly observed at binding energies from 0.16 to 1.7eV. The mirror symmetry of the electronic structure is consistent with the atomic structure of HCT model shown in Figs.4.1 and 4.2, since it has a mirror plane including [11$\bar{2}$], i.e., $\bar{\Gamma}$ -$\bar{\mathrm{K}}$ direction.

4.3.1 Band structure

To identify the observed intensity distributions, PEADs were given mirror symmetry operation to obtain more sharp pattern and to facilitate the discussion. The mirror operation was carried out considering the mirror symmetry with respect to the $\bar{\Gamma}$ -$\bar{\mathrm{K}}$ line as well as that of the incident light to maintain the parity information of the initial states.

PEADs at various binding energies after the mirror symmetry operation for $\phi = 0°$ and $\phi = 30°$ are presented in Figs.4.6(a) and (b), respectively. Note that the intensity of each image is normalized to its maximum value.

In Fig.4.6(a), the intensity distribution gradually changes with the binding energy. Rather dim distribution around $\bar{\Gamma}_2$ point of each SBZ at E_B =0.16eV becomes a strong peak at $\bar{\Gamma}_2$ point at E_B =0.3eV. At E_B =0.5eV, "horseshoe"-like distribution appears. It scarcely changes its shape as well as relative intensity distribution inside of it up to E_B =1.0eV. The intensity distribution gradually changes again from E_B =1.1eV to 1.4eV and a drastic change is observed from E_B =1.5eV to 1.7eV to cancel "horseshoe"-like distribution. The changing behavior is almost the same in $\phi = 30°$ configuration as shown in Fig.4.6(b).

The observed characteristic features are summarized in Fig.4.7 which shows PEADs at binding energies of (a)0.3eV and (c)1.6eV in $\phi = 0°$ configuration and of (b)1.0eV and (d)1.6eV in $\phi = 30°$ configuration, respectively. In each image, 1×1 SBZ of ideal Si(111) surface as well as $\sqrt{3} \times \sqrt{3}$ SBZ is represented by orange and white lines, respectively. These SBZs are summarized in the inset. A contour map of the bulk projection is also shown in (e) which is derived from one-dimensional distribution along the high symmetry lines in Ref.[21]. Each contour line represents 0.1eV step from valence band maximum (VBM) at each $\bar{\Gamma}$ points of 1×1 SBZ up to E_B =2.1eV from VBM at $\bar{\mathrm{K}}$ points of the same

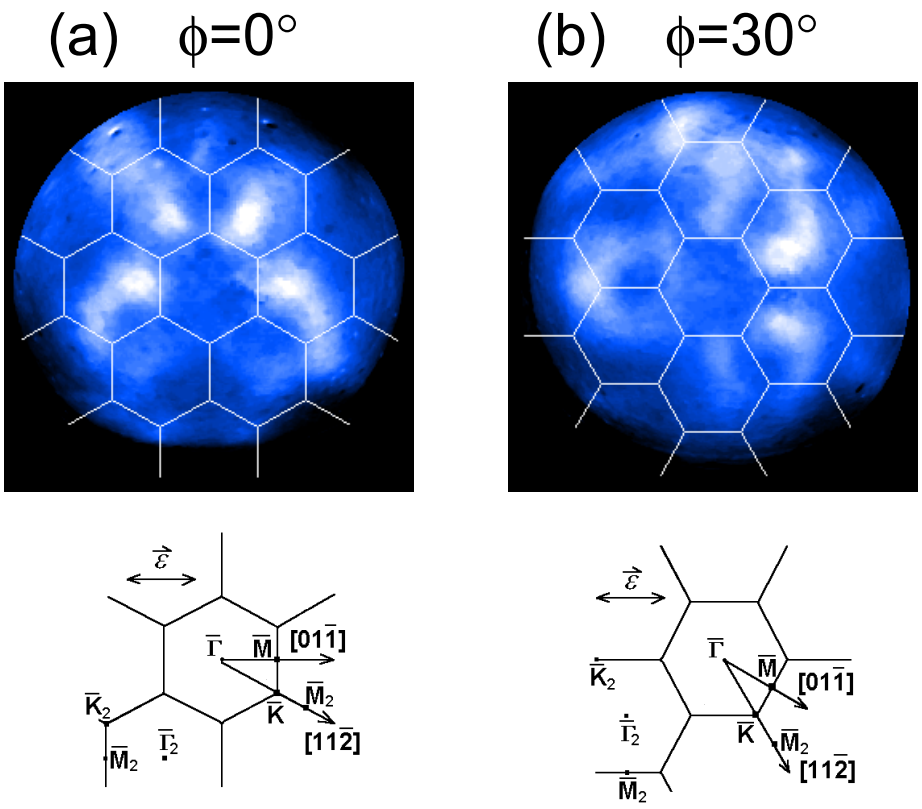

Figure 4.5 PEAD of two experimental configurations at E_B=1.1eV. (a) is PEAD in a configuration ϕ=0° in which the electric vector of incident light is parallel to $\bar{\Gamma}-\bar{M}$ direction of $\sqrt{3}\times\sqrt{3}$ surface Brillouin zone. (b) is in another configuration ϕ=30° which is rotated 30° from ϕ=0°. The intensity distribution in each configuration shows a mirror symmetry whose mirror plane is along $\bar{\Gamma}-\bar{K}$ line.

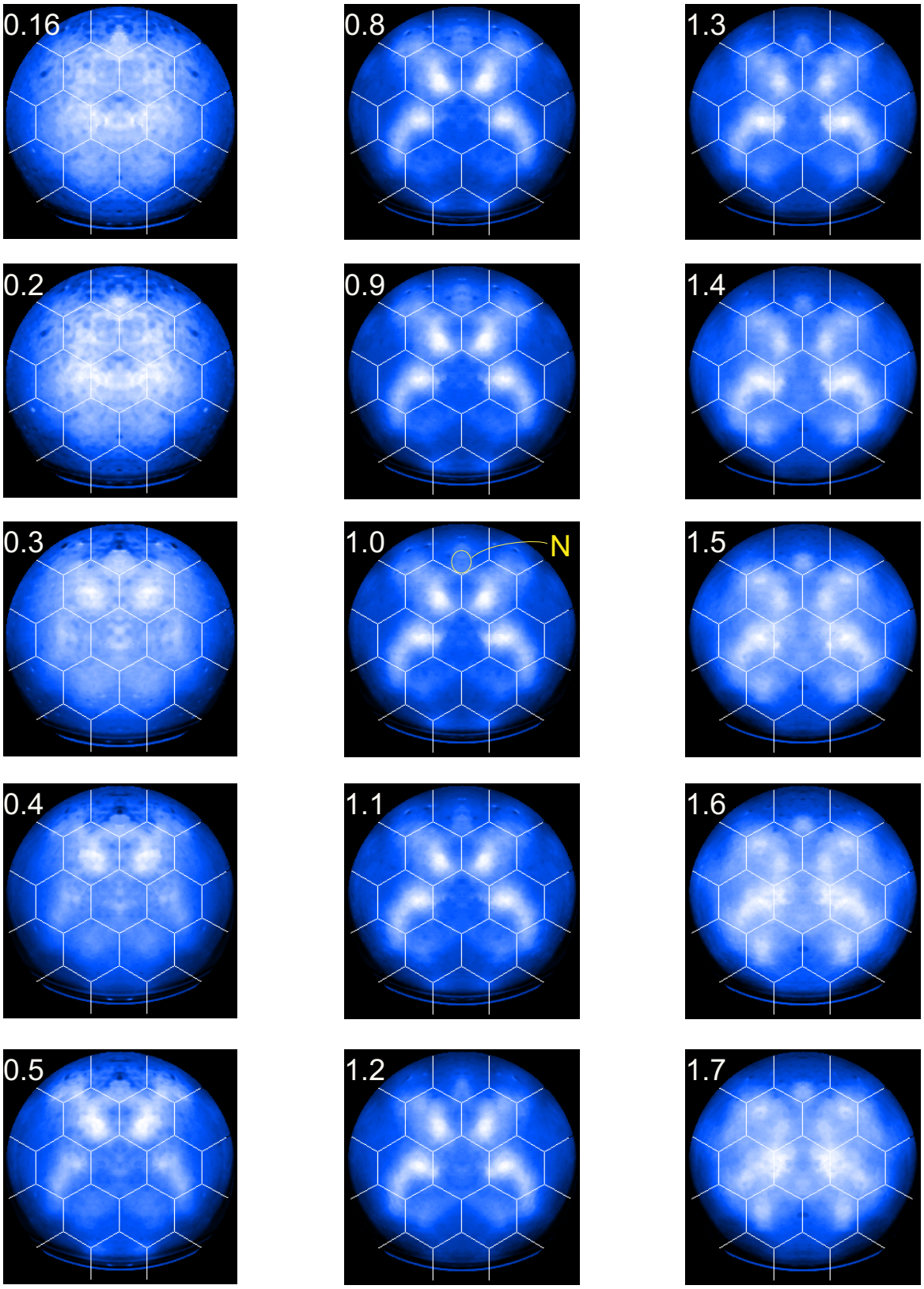

Figure 4.6(a) PEADs at various binding energies in ϕ=0° configuration after the mirror operation. The number in each image represents the binding energy in eV unit. The area denoted as N at 1.0eV represents a noise distribution. See the text in details.

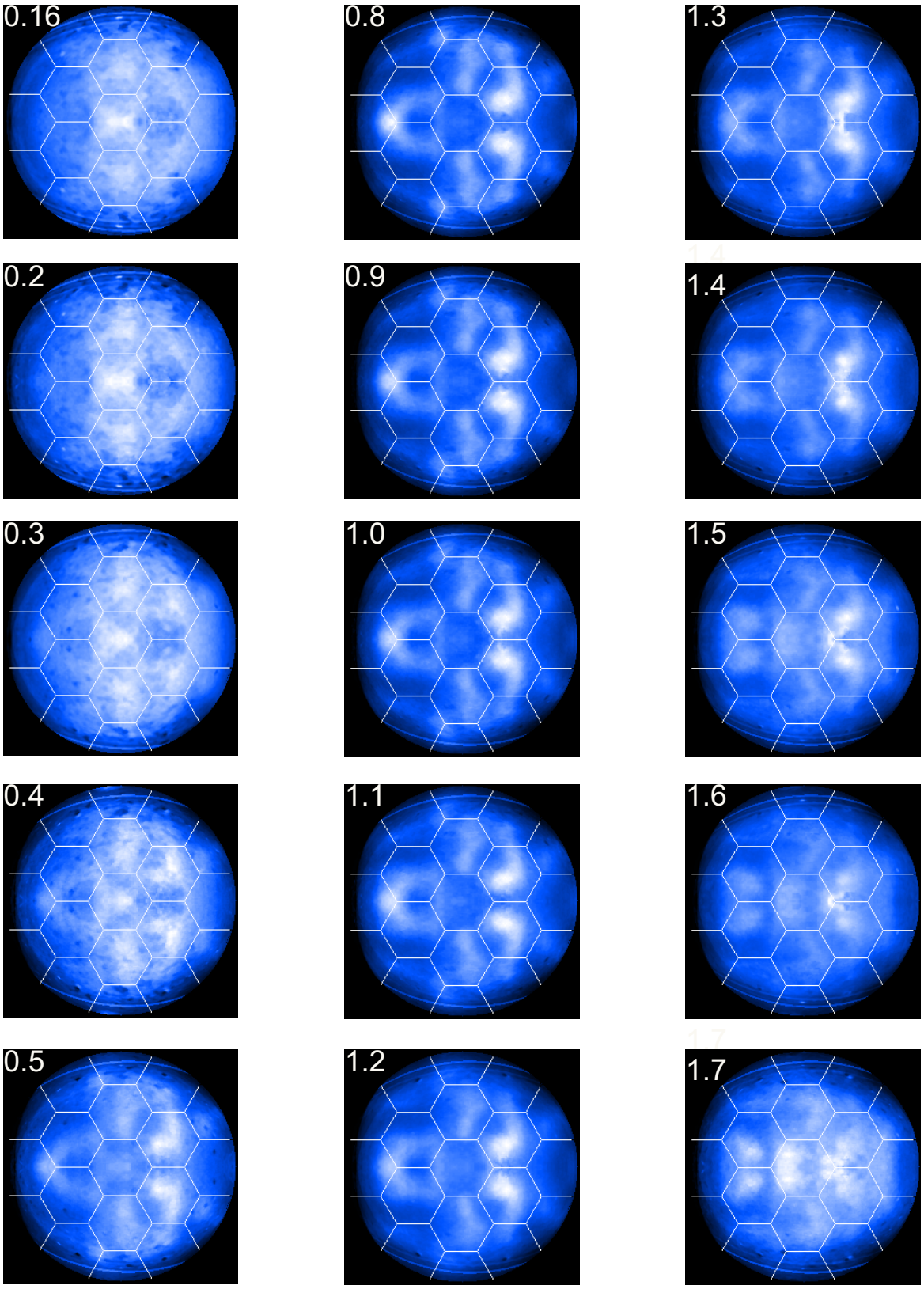

Figure 4.6(b) PEADs at various binding energies in ϕ=30° configuration after the mirror symmetry operation. The number in each image represents the binding energy in eV unit. See the text in details.

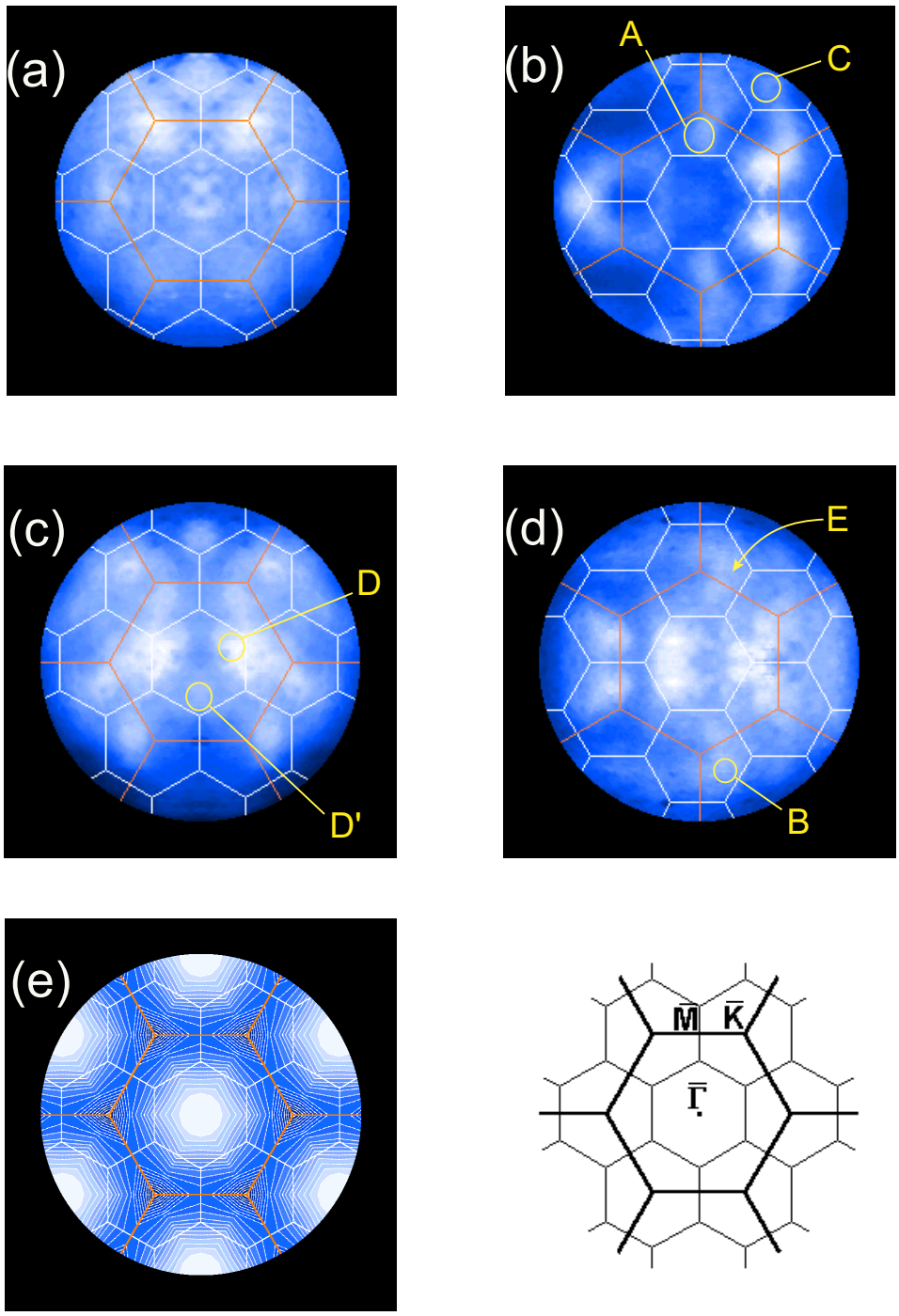

Figure 4.7 Characteristic distributions observed in the PEADs in Fig.4-6 ((a) to (d)) at the binding energies of 0.3, 1.0, 1.6 and 1.6eV, respectively. A contour map of the bulk projection derived from Ref.[21] is also shown in (e) where each contour line represents 0.1eV step and the most intense area around $\bar{\Gamma}$ points of 1×1 Brillouin zones (BZs) correspond to the valence band maximum. $\sqrt{3} \times \sqrt{3}$and 1×1 SBZs are shown in the inset and are represented by white and orange lines in each image. See the text in details.

SBZ. In the present result, VBM is assumed to be $\sim$ 0.16eV below Fermi level, which has been reported on a p-type substrate[23].

In Fig.4.7(a), a strong peak is seen at the $\bar{\Gamma}_2$ point of the second $\sqrt{3} \times \sqrt{3}$ SBZ which corresponds to the $\bar{\mathrm{K}}$ point of 1×1 SBZ. This peak lies well apart from the bulk projection so that it is considered to be a surface state. It moves towards $\bar{\mathrm{M}}_2$ point of $\sqrt{3} \times \sqrt{3}$ SBZ as the binding energy decreases and the observed dispersion is shown in Fig.4.9(a). The bottom of this band is estimated to be about 0.3eV. This band, named S_1 state, is considered to be the same one as recently reported metallic band which was observed in ARPES spectra[12, 17, 23], judging from its dispersion and energetic position.

Other characteristic distributions are shown in Fig.4.7(b), (c) and (d). On the $\bar{\Gamma}$ -$\bar{\mathrm{M}}$ line, apparent distribution denoted as A in (b) and B in (d) are observed. The position of A does not depend on the binding energy and clearly seen between 0.5 and 1.5eV while B moves towards $\bar{\Gamma}_2$ point from E_{B} =1.7 to 1.2eV. This movement is plotted within the reduced zone scheme in Fig.4.9(b) in which the observed peaks inside and outside the bulk projection are represented by open and solid circles. The observed position of B corresponds to the dispersion denoted as B which lies almost outside the bulk projection. Therefore, B is considered to be a surface state or a resonance state.

On the other hand, on the $\bar{\Gamma}$ -$\bar{\mathrm{K}}$ line, the distributions denoted as C in Fig.4.7(b) and D in (c) are observed. C lies between $\bar{\Gamma}_3$ point of the third SBZ and $\bar{\mathrm{K}}_2$ point at around 1.0eV followed by the movement towards $\bar{\mathrm{K}}_2$ point as the binding energy increases. D is seen between $\bar{\Gamma}$ and $\bar{\mathrm{K}}$ point at 1.7eV and moves towards $\bar{\mathrm{K}}$ point as the binding energy decreases. The behavior of another distribution D$'$ in (c) is similar to that of D although its intensity is much weaker than that of D. Hence, D$'$ is considered to be the same band as D. These behaviors of C and D(D$'$) are shown in Fig.4.9(b) by the dispersion denoted as C and D, respectively. Both of them are inside the bulk projection. On the $\bar{\Gamma}$ -$\bar{\mathrm{K}}$ line, another distribution denoted as E in Fig.4.7(d) is observed although it is rather dim and seems to be mixed with the adjacent distribution B. Nevertheless, it has a dispersion towards $\bar{\Gamma}_2$ point as the binding energy decreases from 1.7 to 1.2eV as shown in Fig.4.9(b) denoted as E.

Other changes in the PEAD are also plotted and we could derive some steep dispersions. However, the distinct distribution A has not been plotted. Even if there were bands with flat dispersion, we could not distinguish them from the above analysis in which only the changes in PEAD are noticed, since PEAD is a constant energy surface. Therefore, we have derived angle-resolved energy distribution spectra from the obtained PEADs, which is attributed to the same fashion in the measurement by a conventional one-dimensional ARPES. Fig.4.8 shows angle-resolved spectra along $\bar{\Gamma}$ -$\bar{\mathrm{M}}$ line derived from PEADs. To obtain these spectra, the total count of PEAD was normalized to that of the angle integrated spectrum shown in Fig.4.4 at each corresponding binding energy. Because the energy resolution, $\pm$0.26eV, is not so good, it is hard to distinguish detailed dispersions which have already been mentioned before. However, we can recognize that there are at

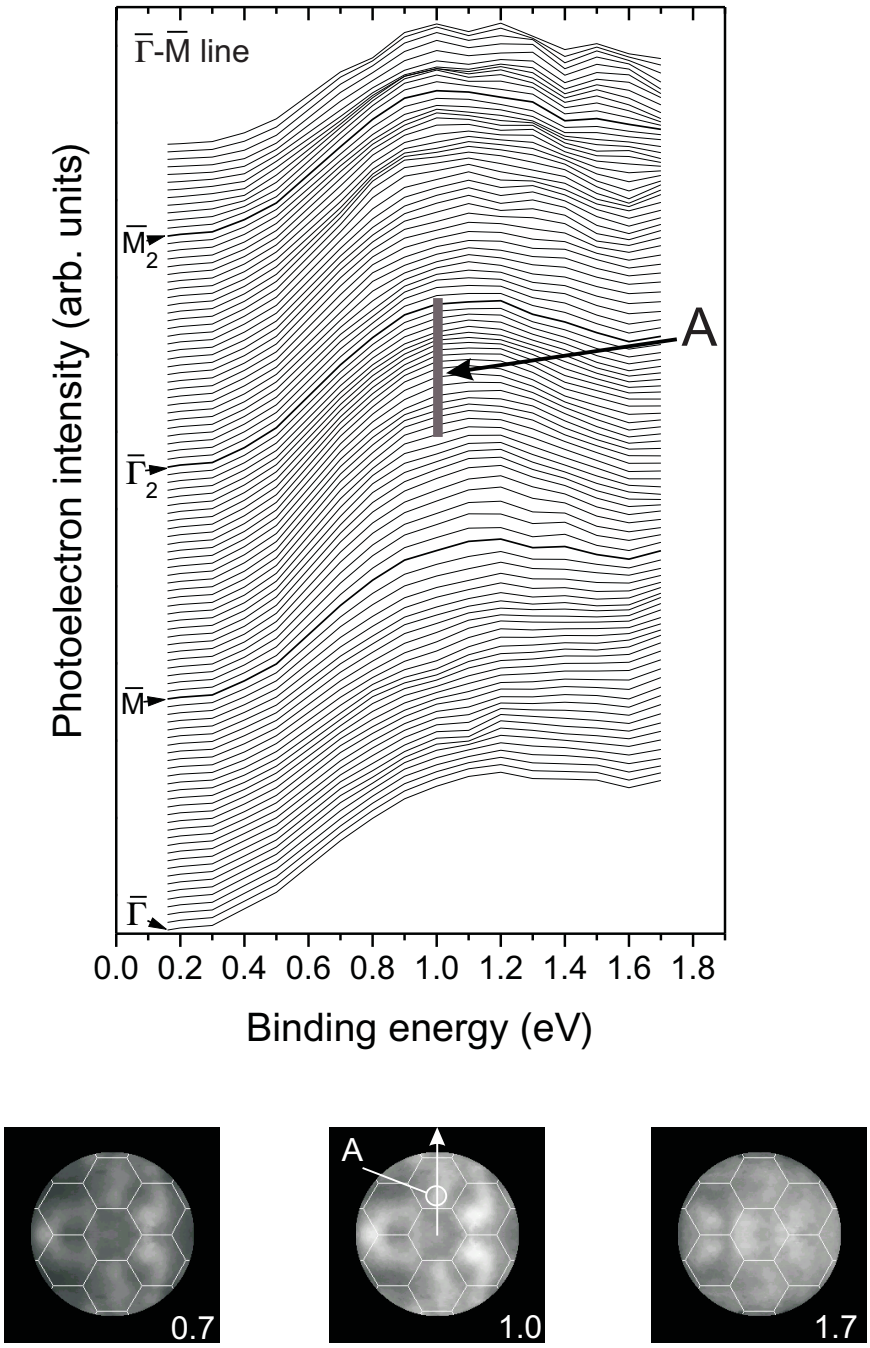

Figure 4.8 ARPES spectra along $\bar{\Gamma}$-$\bar{M}$ line derived from PEAD patterns whose total count are normalized to that of the angle integrated spectrum shown in Fig.4.4. The normalized PEADs are also shown for the binding energies of 0.7, 1.0 and 1.7eV. The $\bar{\Gamma}$-$\bar{M}$ line is represented by a white arrow in 1.0eV image. The intense area denoted as A corresponds to the peaks represented by A in the ARPES spectra which have almost flat dispersion between $\bar{M}$ and $\bar{\Gamma}_2$ points.

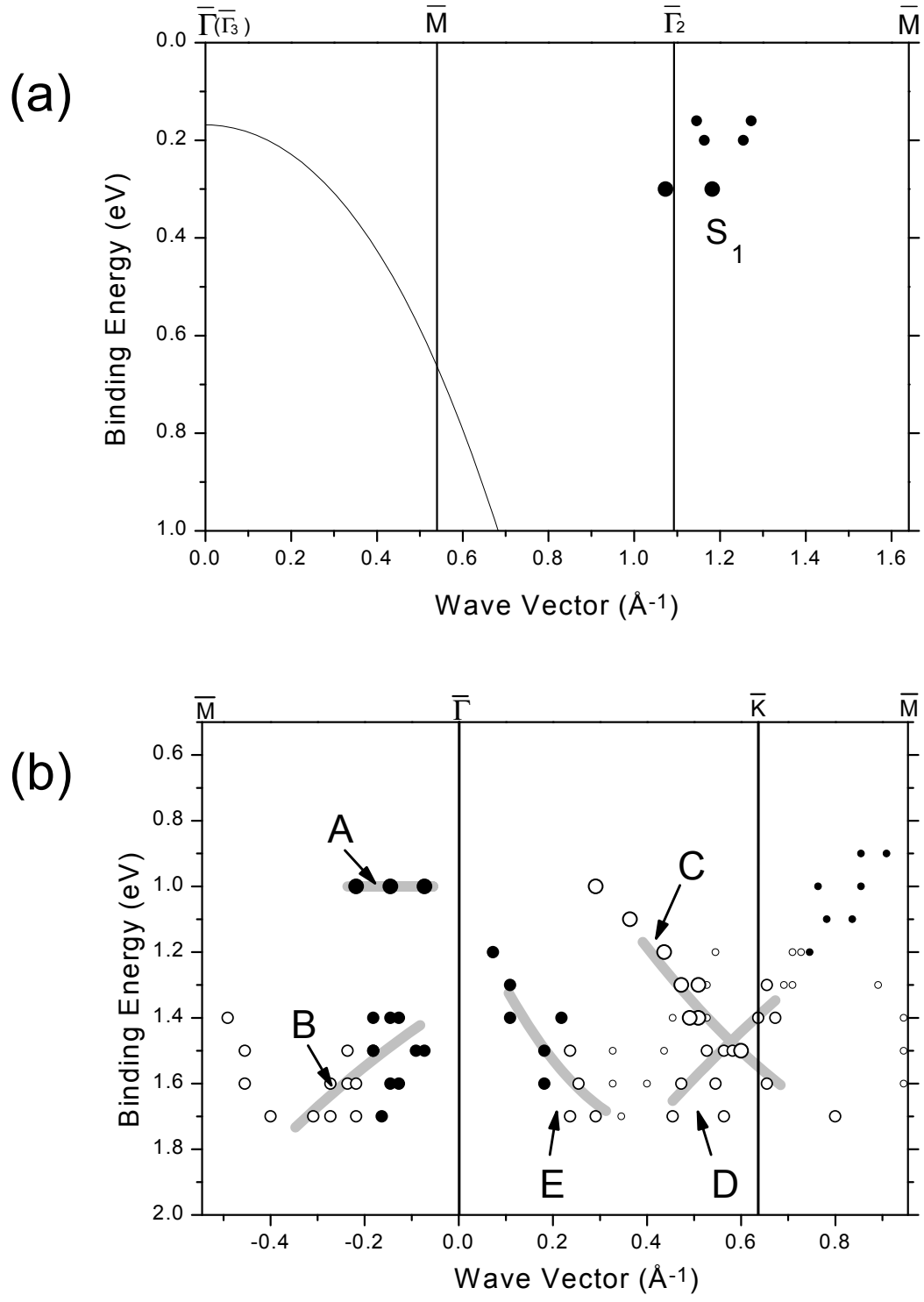

Figure 4.9 Band structure derived from experimental PEAD. (a) is the dispersion along $\bar{\Gamma}$-$\bar{M}$ line which includes S_1 state denoted by filled circles. The solid curve represents the upper edge of the bulk projection. (b) is the dispersions along $\bar{\Gamma}$-$\bar{K}$-$\bar{M}$ line. Filled and open circles denote the states inside and outside the bulk projection, respectively.

least one flat band which lies between $\bar{\mathrm{M}}$ and $\bar{\Gamma}_2$ point denoted as A. Hence, the observed distribution A in Fig.4.7(b) is considered to have a flat dispersion as shown in Fig.4.9(b). The commonly observed "horseshoe"-like distributions from E_{B} =0.5eV to 1.5eV in Fig.4.6 are explained to be extrinsic patterns originated from the tail of the main peak considering a broad lineshape of each spectrum in Fig.4.8.

In this way, the band dispersion along high symmetry lines is derived from PEADs at various binding energies. The obtained dispersions in Fig.4.9(b) are similar to those in the previous reports[11, 12, 23]. The crossing behavior around $\bar{\mathrm{K}}$ point has been seen in the results by Johansson *et al.* in which two surface states or resonances along each high symmetry line, i.e., S_2 and S_3 along $\bar{\Gamma}$ -$\bar{\mathrm{M}}$ line, S_2' and S_3' along $\bar{\Gamma}$ -$\bar{\mathrm{K}}$ line, respectively, are suggested as shown in Fig.4.2.

4.3.2 The origin of observed bands

PEAD consists of three factors as described in chapter 2, which are 1D-DOS, angular distribution of squared transition matrix element from atomic orbital which is the base of the initial state ($|M_A|^2$), and photoemission structure factor which determines the intensity distribution through Brillouin zones ($|M_C|^2$). Therefore, we can investigate the character of the initial state by comparing the angular distribution of experimental result with that of calculated $|M_A|^2$ from each atomic orbital by using linearly polarized incident light[22]. $|M_A|^2$ distributions from s, p_x, p_y and p_z orbitals are shown in Fig.4.10 in the same coordinate system as in the present experiment in which x axis corresponds to the horizontal axis on the page. Here, subscripts x, y, z mean the orbitals along the corresponding axis, which are fixed on the page.

Metallic surface state S_1 Figure 4.11 shows PEADs at E_{B} =0.3eV in $\phi = 0°$ and 30° in which the intense area at $\bar{\Gamma}_2$ point of each second $\sqrt{3} \times \sqrt{3}$ SBZ corresponds to S_1 state. These images are given mirror symmetry operation for vertical and horizontal central lines in (a) and (b), respectively. Note that the polarization vector of incident light is parallel to the horizontal axis.

Comparing these PEADs with $|M_A|^2$ distribution shown in Fig.4.10, s and p_z characters of S_1 state are denied since S_1 is visible in Fig.4.11(b) even around the vertical central line where the photoemission from an initial state with such characters is forbidden. In the present case, however, it is hard to distinguish p_x and p_y orbitals because some bonding orbitals in the system are expected to have three-fold rotational symmetry. Therefore, we can say that this state S_1 has *in-plane* p character which is a mixture of p_x and p_y orbitals with a certain ratio. Considering $|M_A|^2$ distributions in Fig.4.10, a finite transition probability to the area around vertical central line is undoubted even from an initial state with p_x and p_y characters. In the observed PEAD, there seems to exist an asymmetry in the intensity distribution. In $\phi = 0°$ configuration, for example, the intensity of the PEAD in the lower part is smaller than that in the upper part. The origin of this kind of

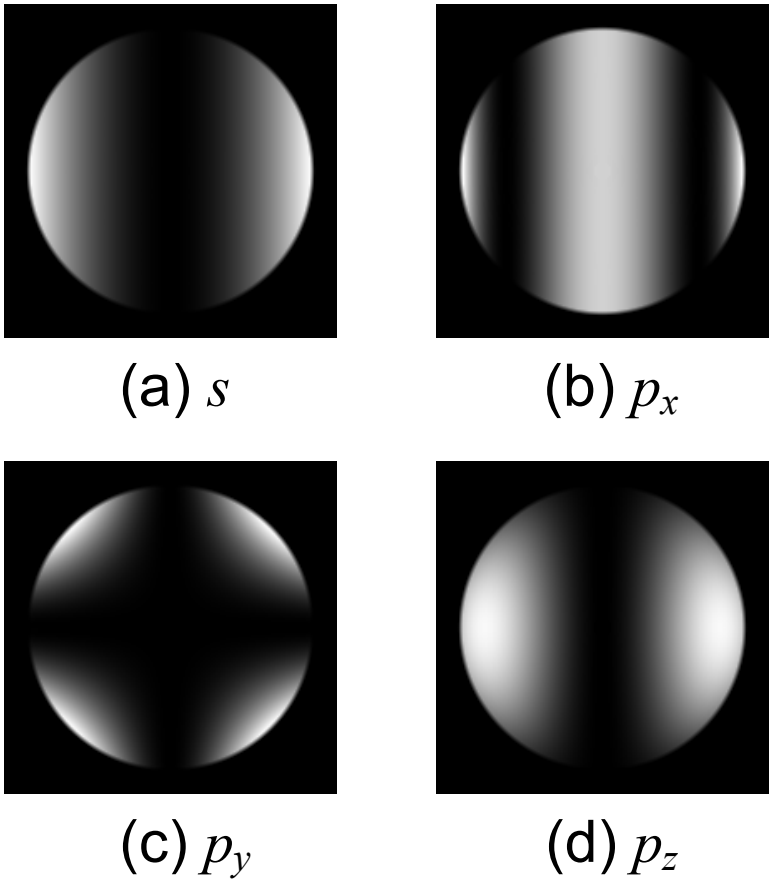

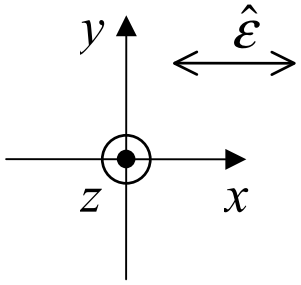

Figure 4.10 Calculated angular distribution of $|M_A|^2$ for the initial state of; (a) s, (b) p_x, (c) p_y and (d) p_z orbital. The circumference of each image corresponds to the polar angle of 60°. The right handed coordinate system and the polarization of the incident light are also shown.

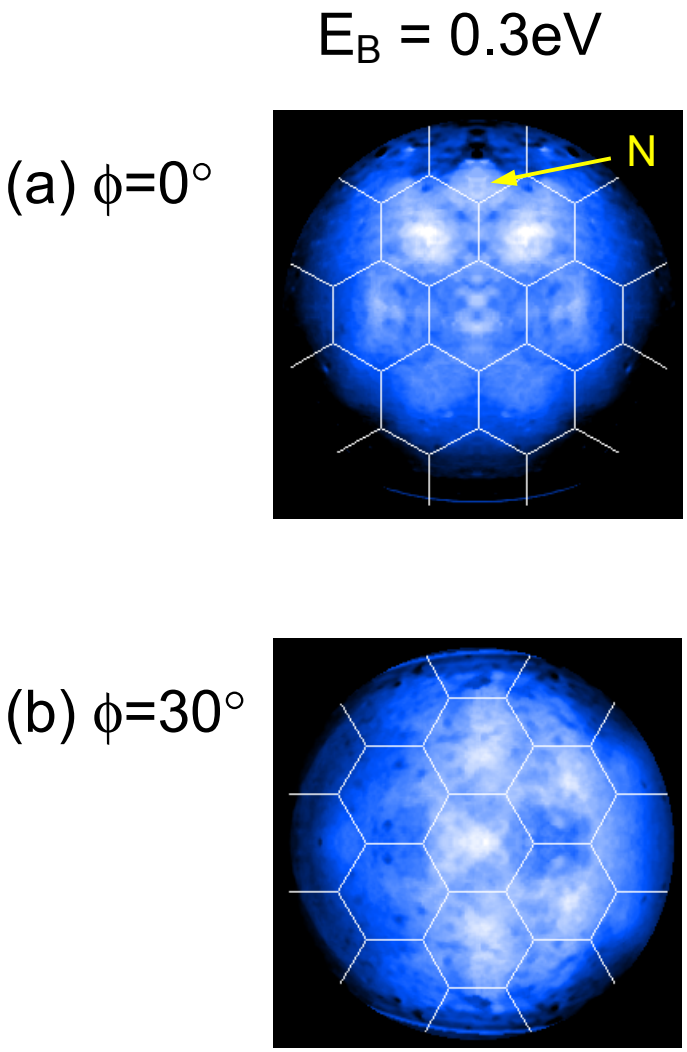

Figure 4.11 PEAD at E_B=0.3eV. (a) and (b) are ϕ=0° and ϕ=30° configurations, respectively. Each image has been modified from the original one by mirror symmetry operation along $\overline{\Gamma}$-$\overline{K}$ line. Bright area around each $\overline{\Gamma}_2$ point of the 2nd surface Brillouin zone (SBZ) as well as that of 1st SBZ correspond to S_1 state. Intensity distribution around $\overline{K}_2$ point denoted as N in (a) is a noise due to the mirror reflection of incident light from the sample, which should be ignored.

assymmetry in PEAD may be related to the hybridization of p_x and p_y orbitals although the details are not discussed in this thesis.

S_1 state has been observed as an occupied state by partial filling of the empty band[12, 18], which is calculated to have its minimum around $\bar{\Gamma}$ point by Watanabe *et al.*[8]. They also revealed that the honeycomb protrusions in the unoccupied state STM image is due to the body center of Ag triangle where the contribution from Ag $5s$ and $5p$ orbitals dominates the density of states. Therefore, the origin of S_1 state is considered to be *in-plane* Ag $5p$ orbital.

The origin of the extra charge constituting to S_1 band has been suggested to be the band bending in the case of high-doped n-type substrate[12], whereas it has not been a dominant factor in the case of p-type substrate[23] although the partial filling of the empty band is intrinsic. In the present experiment, p-type substrate is used and the origin of the charge in S_1 band is still a matter of controversy. However, a small amount of extra Ag atoms on the surface may play an extrinsic role on the partial filling in the present case since there are some inaccuracy in the estimation of Ag saturation coverage. This possibility is supported by somewhat large binding energy of observed bottom of S_1 band ($\sim$0.3eV) which is in good agreement with that of the recent work on p-type surface with extra Au coverage of 0.1ML[23].

Other surface states Figure 4.12 shows PEADs in $\phi = 0°$ and $30°$ at the binding energies of (a)1.1eV and (b)1.7eV which correspond to the top and the bottom of the observed bands. To determine the character of each band, four distinct distributions which belong to each band are discussed. In the figure, A$'$ to D$'$ in $\phi = 0°$ are the equivalent distributions of A to D in $\phi = 30°$, each of which represents each band of A to D in Fig.4.9(b).

In Fig.4.12(a), the band A is observed in both configurations of $\phi = 30°$ and $\phi = 0°$. s or p_z character of this band is denied because the distribution A is observed on the vertical central line where the photoemission from the initial state of such characters are forbidden as shown in Fig.4.10. Therefore, the character of the initial state A is considered to be *in-plane* p orbital.

On the other hand, the angular distribution C is observed in $\phi = 30°$, whereas that at the equivalent position C$'$ is very weak on the central vertical line in $\phi = 0°$. Since the noise distribution exists around here due to the reflection of the incident light from the sample, the band C is considered to be almost invisible when its distribution is on the vertical central line. This behavior is in good agreement with that of the distribution of $|M_A|^2$ from p_z and s orbitals in Fig.4.10 which suggests that the initial state has p_z or s character.

At higher binding energy in Fig.4.12(b), the band B and D are observed in both configurations. As to D, however, it shows a very intense peak in $\phi = 30°$ whereas in $\phi = 0°$, the equivalent distribution denoted as D$'$ has a very weak intensity on the vertical central line. Therefore, the band D has a considerable p_z or s character. On the other hand, B

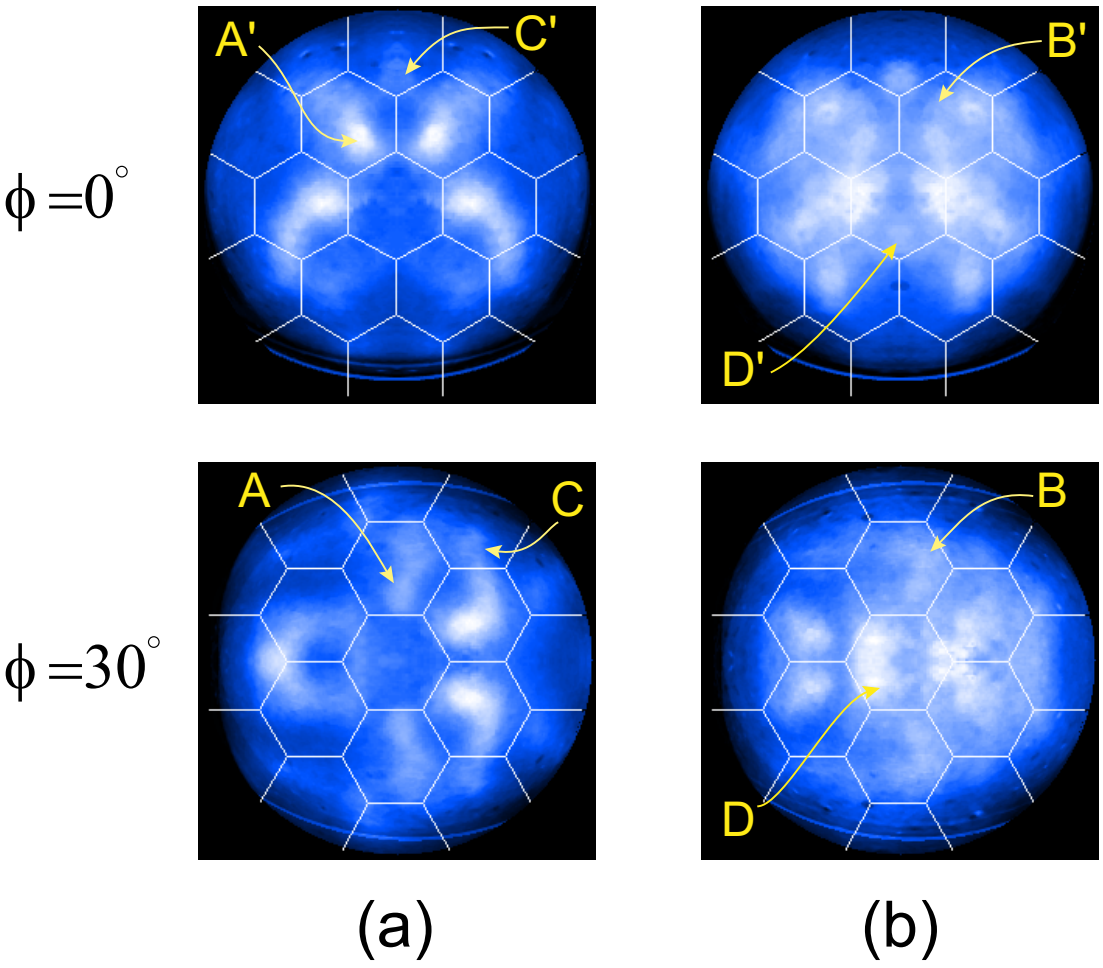

Figure 4.12 PEADs for two configurations. (a) and (b) are the images observed at E_B= 1.1 and 1.7eV, respectively. See the text in details.

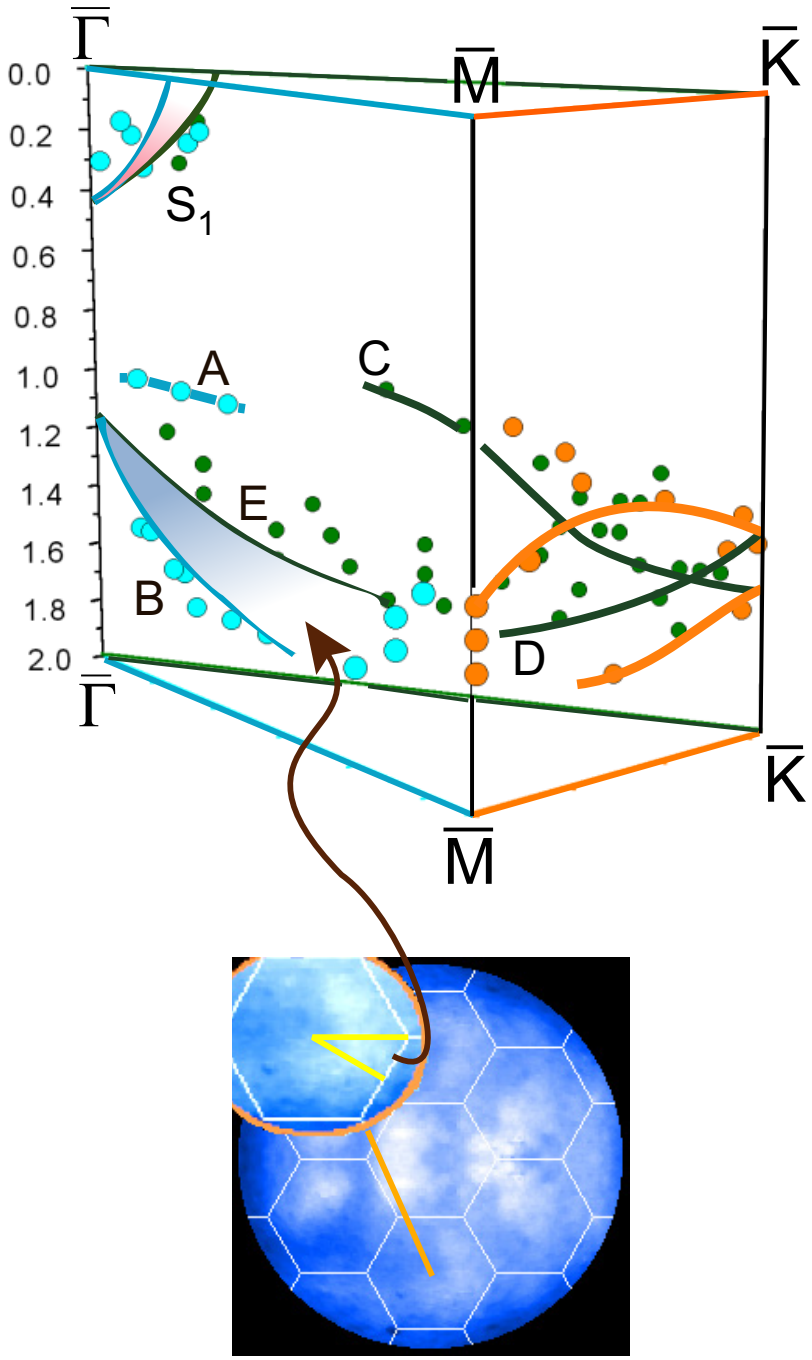

Figure 4.13 3D plot of the observed dispersions (A-E). The area between B and E bands corresponds to the observed distribution indicated below. See the text in details.

is visible in $\phi = 30^\circ$ in spite of its position close to the vertical central line, suggesting *in-plane p* character of the initial state.

From the above discussion, the observed bands A, B, C and D are confirmed to have *in-plane p*, *in-plane p*, p_z or s and considerable p_z or s characters, respectively. These assignments are consistent with those in the previous ARPES measurement by Johansson *et al.*[12] except for the band D. Considering the character of each band, S_2, S_3 and S_2' state in their report correspond to A, B and C band, respectively. Although the observed D band is energetically similar to S_3' state, the initial state has a considerable p_z or s character, which is contradictory to the previously suggested *in-plane p* character of S_3' state.

Three-dimensional expression of the observed bands The observed bands are plotted in a three-dimensional (3D) expression as shown in Fig.4.13. z-axis and x-y plane correspond to the binding energy and a reduced SBZ, respectively. From the figure, one can recognize that the dispersions B and E have similar slope and energetic position. This implies that these bands are located on the same band which is expressed as a curved surface as shown in the figure. Actually, the corresponding intensity distribution in the observed PEAD seems to spread between the $\bar{\Gamma}$ -$\bar{\mathrm{M}}$ and $\bar{\Gamma}$ -$\bar{\mathrm{K}}$ lines. This kind of feature would not be observed except for 2D measurement.

4.4 Summary

Surface states on Si(111)-($\sqrt{3} \times \sqrt{3}$)R30° -Ag surface was investigated using 2D PES. The obtained PEADs at binding energies up to 1.7eV showed mirror symmetry with respect to the $\bar{\Gamma}$ -$\bar{\mathrm{K}}$ line of SBZ which suggests the electronic structure having this symmetry.

From the intensity distribution of PEADs, the existence of some surface states or resonances and their characters have been revealed. A metallic band S_1 was observed at the binding energy of around 0.3eV. The intensity distribution does not show s and p_z character considering that of $|M_A|^2$. This suggests *in-plane p* character of this band originated from Ag 5p orbital. Other surface states or resonances were observed between the binding energy of 1.0eV and 1.7eV. PEADs from S_2' state (C band) showed a character of p_z or s orbital considering $|M_A|^2$ distribution whereas those of S_2 and S_3 states (A and B bands) were assigned to *in-plane p* orbital. The other band D was revealed to have a considerable p_z or s character, which is different from that of the previously reported S_3' state. In this way, the characters of each surface state or resonance has been confirmed by comparing PEAD with the intensity distribution of $|M_A|^2$ from each atomic orbital.

The observed bands were summarized in a 3D expression and it was suggested that the band B and E are the parts of the same band on a curved surface.

References

[1] Y. Terada, T. Yoshizuka, K. Oura and T. Hanawa, Surf. Sci.**114** (1982) 65.

[2] K. Horioka, H. Iwasaki, S. Maruno, S-T. Li and S. Nakamu ra, Surf. Sci.**136** (1984) 121.

[3] S. Kono, K. Higashiyama, T. Kinoshita, T. Miyahara, H. Kato, H. Ohsawa, Y. Enta, F. Maeda and Y. Yaegashi, Phys. Rev. Lett.**58** (1987) 1555.

[4] T. L. Porter, C. S. Chang and I. S. T. Tsong, Phys. Rev. Lett.**60** (1988) 1739.

[5] T. Takahashi, S. Nakatani, N. Okamoto, T. Ishikawa and S. Kikuta, Jpn. J. Appl. Phys. **27** (1988) L753.

[6] M. Katayama, R. S. Williams, M. Kato E. Nomura and M. Aono, Phys. Rev. Lett.**66** (1991) 2762.

[7] Y. G. Ding, C. T. Chan and K. M. Ho, Phys. Rev. Lett.**67** (1991) 1454.

[8] S. Watanabe, M. Aono and M. Tsukada, Phys. Rev.**B44** (1991) 8330.

[9] R. J. Wilson and S. Chiang, Phys. Rev. Lett.**58** (1987) 369.

[10] E. J. van Loenen, J. E. Demuth, R. M. Tromp and R. J. Hamers, Phys. Rev. Lett.**58** (1987) 373.

[11] T. Yokotsuka, S. Kono, S. Suzuki and T. Sagawa, Surf. Sci.**127** (1983) 35.

[12] L. S. O. Johansson, E. Landemark, C. J. Karlsson and R. I. G. Uhrberg, Phys. Rev. Lett.**63** (1989) 2092.

[13] Y. G. Ding, C. T. Chan and K. M. Ho, Phys. Rev. Lett.**69** (1992) 2452.

[14] J. M. Nicholls, F. Salvan and B. Reihl, Surf. Sci.**178** (1986) 10.

[15] S. Heun, J. Bange, R. Schad and M. Henzler, J. Phys.: Condens. Matter**5** (1993) 2913.

[16] S. Hasegawa and S. Ino, Phys. Rev. Lett.**68** (1992) 1192.

[17] Y. Nakajima, G. Uchida, T. Nagao and S. Hasegawa, Phys. Rev.**B54** (1996) 14134.

[18] Y. Nakajima, S. Takeda, T. Nagao, S. Hasegawa and X. Tong, Phys. Rev.**B56** (1997) 6782.

[19] F. J. Himpsel, P. Heimann and D. E. Eastman, Phys. Rev. **B24** (1981) 2003. R. D. Schnell, D. Rieger, A. Bogen, F. J. Himpsel, K. Wandelt and W. Steinmann, Phys. Rev.**B32** (1985) 8057.

[20] H. Daimon and S. Ino, Rev. Sci. Instrum. **61** (1990) 57. H. Nishimoto, H. Daimon, S. Suga, Y. Tezuka, S. Ino, I. Kato, F. Zenitani and H. Soezima, Rev. Sci. Instrum. **64** (1993) 2857.

[21] K. C. Pandey, Phys. Rev.**B14** (1976) 1557.

[22] H. Daimon, S. Imada, H. Nishimoto and S. Suga, J. Electron Spectrosc. Relat. Phenom., **76** (1995) 487.

[23] X. Tong, C. S. Jiang and S. Hasegawa, submitted to Phys. Rev..

Chapter 5

Adsorption and desorption processes of Cl on Si surface studied by electron stimulated desorption (ESD) and LID

5.1 Background

There have been great interests in the chlorine chemisorbed silicon surface because of its potential for the application to dry etching process in VLSI technologies. On the contrary, the formation of a surface dipole layer is expected due to a large electronegativity of chlorine, which is another kind of interest in this system.

The adsorption geometry and the electronic structure of Cl on Si(001)2×1 surface has been investigated by lots of methods. Rowe *et al.* found some Cl induced states using polarization dependent PES[1]. They suggested that 2×1 periodicity remains during Cl adsorption, and Cl-Si covalent bond is tilted with respect to the surface normal. Recent ARPES study revealed that there are 7 Cl induced surface states each of which has narrow dispersion of ∼0.2eV[2]. From the polarization dependent analysis, it is suggested that Cl disociatively adsorbs on both dangling bonds of symmetric Si dimer as illustrated in Fig.5.1(a). This adsorption site is assisted by other groups using such as LEELS (low energy electron loss spectroscopy)[3] and ESDIAD (electron stimulated desorption ion angular distribution) [4, 6]. In ESDIAD and HREELS (high resolution EELS) study, Gao *et al.* proposed the adsorption to the bridge site of symmetric dimer especially in lower coverage as well as dangling bond site, which is shown in Fig.5.1(b). They also revealed that the Cl atom on the bridge site converts to the dangling bond site by annealing to ∼700K. This bridge site configuration is observed in the STM study[5] in which the adsorbed Cl on one side of dangling bond site hops to the another side via the bridge site whose driving force

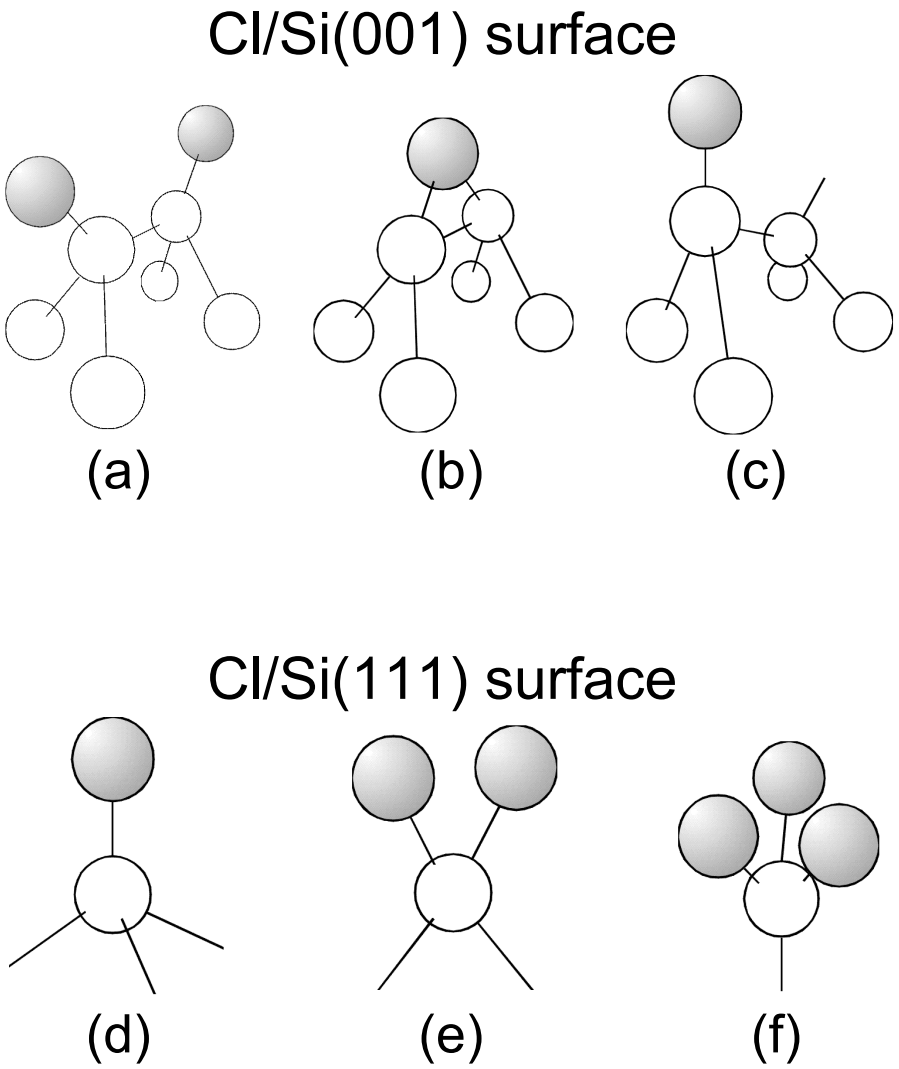

Figure 5.1 Various Cl adsorption sites on Si(001)2×1 ((a)-(c)) and Si(111)7×7 ((d)-(f)) surfaces. Gray-hatched and empty circle denote Cl and Si atoms, respectively. On Cl/Si(001) surface, Cl adsorbs at the on-top site of asymmetric dimer ((c)) or the bridge site of symmetric dimer ((b)) at low coverages, while on the dangling bond site ((a)) at high coverage. On Cl/Si(111) surface, there exists three kinds of adsorption sites. (d), (e) and (f) are SiCl, $SiCl_2$ and $SiCl_3$ species, respectively. At low coverage, only SiCl is found.

is the interaction of probe tip and Si-Cl dipole moment. The on-top site of the asymmetric dimer shown in Fig.5.1(c) in low coverage was found by EXAFS (extended X-ray absorption fine structure)[7] where the bond length of Si-Cl is determined to be 2.00±0.02Å . The other adsorption species, $SiCl_2$ is suggested in ESDIAD study [6]. The ion desorption from the step edge is also suggested [6, 8]. The existence of $SiCl_2$ was confirmed by SCLS (surface core-level shift) studies[9, 10], although the respective amount to SiCl species is small.

The desorption mechanism in PSD on this surface has been proposed by Durbin*et al.* to be initiated by Cl 3*s* core hole excitation[10]. They also suggested the indirect path of desorption around Si 2*p* edge via ESD by inelastically scattered electron.

On Si(111)7×7 surface, Cl adsorbs in the forms of $SiCl_x$ ($x = 1, 2, 3$), which was observed by SCLS measurement[11]. ARPES analysis was also carried out by the same authors and Si-Cl σ bond and Cl-Cl π bond were observed. In the earlier stage of adsorption, preferential adsorption on the on-top site of the adatom, as illustrated in Fig.5.1(d), was observed by STM[12]. It is also suggested that the formation of $SiCl_2$ and $SiCl_3$ shown in Fig.5.1(e) and (f), respectively, occurs by adsorption of Cl one after another on the adatom site with breaking the back bonds between the adatom and the rest atoms.

Regarding to the etching process by thermal desorption, at least two desorption species are reported from both (111) and (001) surfaces[13]; $SiCl_2$ below 850K and above 900K, and $SiCl_4$ below 850K. Cl adsorption on the warm Si(111)7×7 substrate at ∼800K results in 1×1 surface, which is observed by STM[12]. On the other hand, non-thermal etching process using laser irradiation in ultra-violet region has been also reported[14]. In STM and LID combined studies on Cl/Si(111) surface[15, 16, 17, 18], only the desorption of $SiCl_2$ by valence band excitation was observed by laser irradiation, leading to the observation of missing adatoms in STM image (Fig.5.2(a)). Moreover, the rest atom layer, which maintained 7×7 unit cell, appeared after the laser irradiation onto the Cl saturated surface (Fig.5.2(b)).

The understanding of the atomic configuration, electronic structure and desorption phenomena in Cl/Si system seems to be improved considerably by these recent studies. The purpose of the investigation in this chapter is divided into three points as follows. First of all, 2D measurement by using display type analyzer is applied to the positive ion analysis desorbed by the electron irradiation onto Cl/Si(001)2×1 surface. The second is to reveal the mechanism of ESD on this system. Some previous reports proposed the driving force of desorption, while no detailed analysis on kinetic energy of desorbed ions has been done. The adsorption of Cl, which has strong electronegativity, is followed by the creation

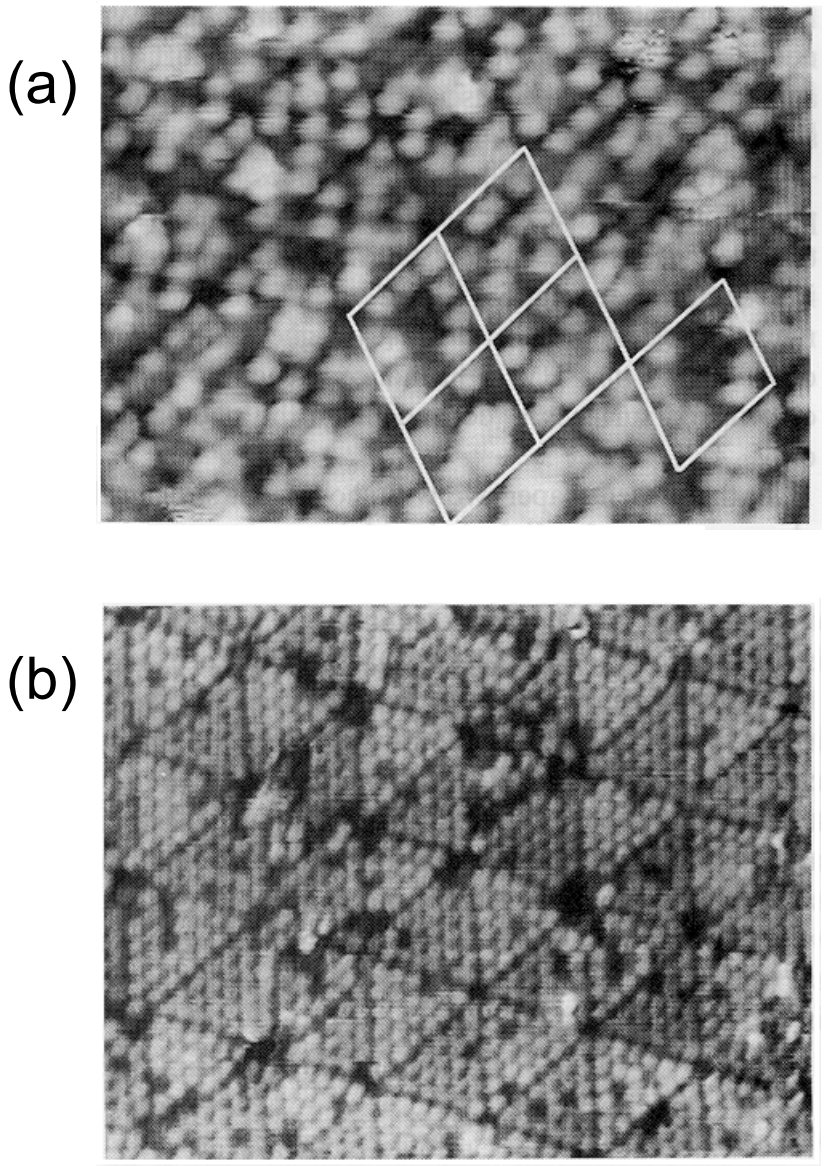

Figure 5.2 STM images of chlorinated Si(111)7×7 surface after irradiation of 4.7eV laser(ref.[17]). (a): Intermediately chlorinated surface after the irradiation (sample bias: +2.5V). Some 7×7 unit cells are indicated. A number of adatoms are missing due to the desorption of $SiCl_2$. (b): Rest-atom surface image obtained by laser induced desorption of $SiCl_2$ from highly chlorinated surface (sample bias: +3.0V).

of surface dipole layer, which will play an important role on the desorption process. The desorbed ion is also expected to pick up the information of this dipole layer due to the outstanding surface sensitivity of ESD. Finally, laser induced ion desorption is studied. Some reports have observed the ion desorption by laser irradiation from the point of view of laser ablation as described in chapter 2, whereas there are few reports about such a phenomenon on adsorbate/semiconductor surface. Whether the ion desorption occurs or not is confirmed and the mechanism of LID is investigated.

In the following arguments, the results of ESD and PSD studies using synchrotron radiation on Cl/Si(111)7×7 surface, which have already carried out by the author as a co-worker[19, 20, 21], will be also presented properly.

5.2 Experimental Procedure

The base pressure of the UHV (ultra high vacuum) chamber was 1-3×10^{-10} Torr. The clean Si(001)2×1 and Si(111)7×7 surface, whose properties will be described later, were exposed to chlorine by the electrolysis of solid AgCl in the UHV[22] at room temperature. The AgCl electrochemical cell which is schematically illustrated in Fig.5.3(a), was mounted 3cm away from the sample, and the amount of chlorine emission could be controlled by the current of the electrolysis which was in the order of 100μA–100mA. The ejected species were measured by the mass spectrometer 20cm away from the cell as shown in Fig.5.3(b). Mass numbers of 35 and 70 correspond to Cl atom and molecule, respectively, while 37 and 74 are the isotopes of them. We have to notice that the intensity ratio of the two spectra shown here does not reflect the real existence ratio since the difference of the sensitivity of these two mass ranges are not clarified. HCl whose hydrogen is presumed to come from the residual gas in the chamber was also observed.

All the measurements of the mass, kinetic energy (E_{K}) and the angular distribution of charged particles were carried out at room temperature (∼290K) using two-dimensional display type spherical mirror analyzer[23].

5.2.1 ESD

In ESD study on Cl/Si(001) surface, a p-type Si wafer cut 4° off the (001) plane towards the [100] direction, and a size of 20×4×0.5 mm^3, was used as a sample. There exist several reports that the single domain 2×1 reconstructed surface is obtained using this kind of vicinal surface[6, 8], but we could not find a proper condition to obtain such a surface. A clean surface was obtained by direct current heating up to 1250C° for 5s about 5.10 times

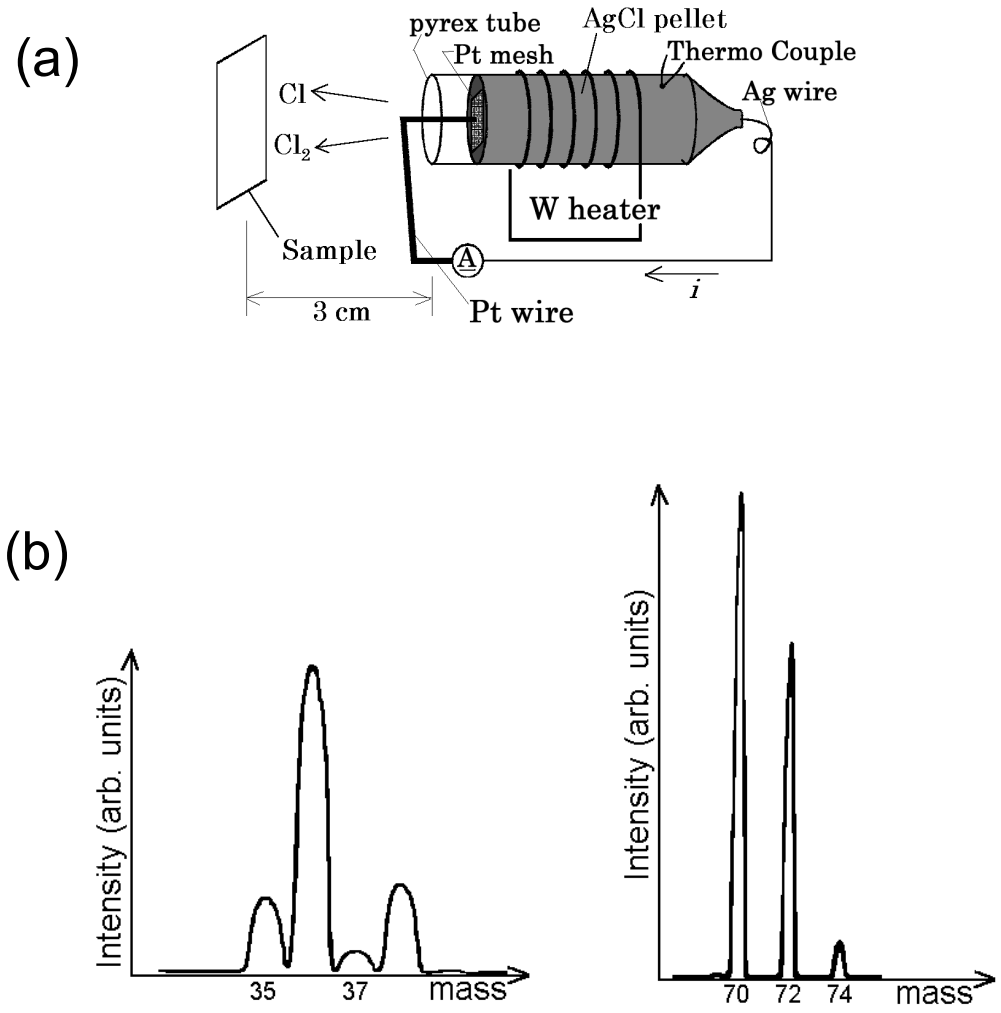

Figure 5.3 (a) Schematic drawing of AgCl electrochemical cell. Cl atoms or molecules fly out through the Pt mesh positive electrode by the electrolysis of solid AgCl in a pyrex glass tube which is kept around 100°C by W heater. The amount of Cl is controlled by the product of current of the electrolysis multiplied by the exposure time, which is typically about 500μA·min. (b) QMS spectra of outgoing species directly detected ~20cm away from AgCl cell. Mass number 35 and 70 correspond to Cl atom and molecule, respectively. 37 and 74 are derived from the isotope. 36 is considered to be HCl due to the residual gas in the chamber with base pressure of $\sim 5\times10^{-9}$ Torr.

in the UHV. The cleanliness was checked by an observation of p(2×2) LEED pattern and negligible carbon, oxygen and chlorine Auger signals. The p(2×2) reconstruction has not been observed in any experimental reports, but it is more stable energetically than 2×1 reconstruction judging from the total energy calculation[24]. The large density of steps on this surface might play an important role to make this reconstruction.

For mass analysis of the desorbed ions, a TOF (time of flight) technique was employed. The incident pulsed electron beam had a width of ∼400ns and intervals of ∼120μs. The change of work function was estimated by the change of low energy cut-off of the secondary electrons. The measurement of the absolute value of the work function has not been made because only the magnitude of its change was necessary for the analysis. The incident electron energy for ESD was 350eV and the sample was biased +15eV. The energy resolution was almost ±0.15eV.

5.2.2 LID

For LID study on Cl/Si(111) surface, a Si(111) wafer (n-type, 2000 Ωcm) with a size of 15×3×0.5mm^3 was used. A cleaning procedure was the same as in the case of Si(001) surface to obtain 7×7 LEED pattern and Auger signals without any contaminants.

Pulsed laser beam from a portable ArF excimer laser (MPB technologies, 193nm, 3.5mJ/pulse, pulse width∼5ns) was incident from outside the chamber to the sample surface with 60° polar angle. The beam was focused on the sample with a spot size of 1-3mm^2 using artificial quartz lens outside the vacuum. The fluence was almost 100mJ/pulse, which was small enough to avoid thermal processes on the surface [16]. In the measurement of laser fluence dependence on the ion desorption, the fluence was controlled by stacking Au coated W meshes, whose transmittance is 81% per mesh, just after the exit hole of laser.

5.3 Results

5.3.1 ESD on Cl/Si(001) surface

The coverage (θ) during chlorine exposure was estimated by the Cl_{LMM}/Si_{LMM} Auger peak intensity ratio as shown in Fig.5.4(a) on Si(111) and (b) on Si(001) surface. The horizontal axis is the chlorine exposure expressed by dosing time multiplied by the current during the electrolysis. The saturation is seen on both surfaces and the coverage is represented as θ/θ_S which is the value normalized by the saturation coverage θ_S. However, the saturation behavior is quite different. On (111) surface, the adsorption behavior follows

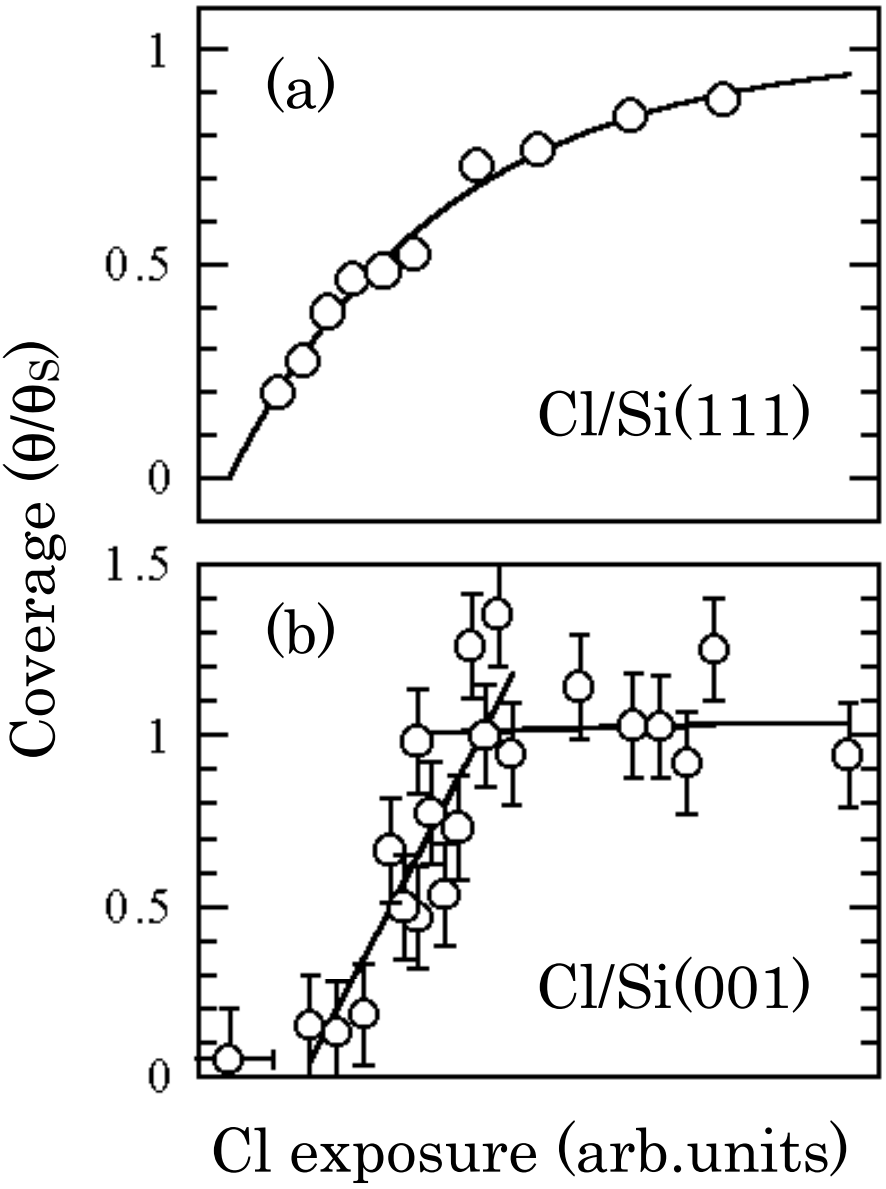

Figure 5.4 Adsorption behavior of Cl on (a): Si(111)7×7 and (b): Si(001)2×1 surfaces. The different adsorption behavior is recognized between the two surfaces.

Langmuir's adsorption equation,

$$\theta(x) = \theta_S[1 - \exp(-\alpha x)] \ , \tag{5.1}$$

where θ_S is the saturation coverage and α is a constant. This equation suggests that the probability of adsorption to the empty site is in proportion to the empty area[20]. On the other hand, the sticking coefficient is constant below the saturation coverage on (001) surface after a delay of some onset.

During the exposure, 7×7 LEED pattern was always observed on (111) surface, whereas p(2×2) pattern on a clean (001) surface gradually changed to 2×1 as the Cl coverage increased between θ/θ_S ∼0.3 and 0.7. At higher coverage, the $(\frac{1}{2}, \frac{1}{2})$ spot vanished. The 2×1 pattern was kept during further exposure. These result represents the fact that the periodicity on the clean surface is maintained even in the Cl saturated surface, and the dimer bond on Si(001) surface does not break.

Figure 5.5 shows a typical E_K distribution of the desorbed ions obtained in the ESD study. Since the sample was biased +15V to accelerate desorbed ions, the horizontal axis has already been shifted so that E_K =+15eV corresponds to 0eV. The reason for the existence of ions with negative E_K is that E_K was measured with respect to the vacuum level of the analyzer. Neither the incident electron energy nor the Cl coverage dependence were observed in the line shape of the distribution whose peak position was around 0eV and FWHM was ∼1eV. These features are very similar to that on Cl/Si(111)7×7 surface [20]. We can also see a slight asymmetry in the spectrum. Considering its profile, we ascribed this asymmetry to the cut-off in the low energy region which derives from the potential barrier for the desorbing ions caused by the image potential of itself. A schematic energy diagram of the system is shown in Fig.5.6.

The lower panel of Fig.5.5 is a typical TOF spectrum. Preferential desorption of Cl^+ at any coverage and E_K at around 55μs was observed except for very weak contribution from H^+ at around 15μs which has its maximum at around E_K =4eV. The origin of hydrogen on the surface would be residual H_2 or H_2O gas in the UHV. A slight H^+ signal in spite of the large ionization cross-section of hydrogen suggests that the quantity of adsorbed hydrogen is negligible. It is known that $SiCl_2$ desorbs as a neutral by laser irradiation onto Cl/Si(111) surface[16] whereas higher order chlorides such as $SiCl_x (x = 1,\ 2,\ 3)$ were not observed as positive ion species. This result is in good agreement with the TOF spectra obtained on Cl/Si(111)[20].

The angular distribution of desorbed Cl^+ (ESDIAD) from nearly saturated surface is presented in Fig.5.7(a) where the horizontal axis corresponds to [110] direction. This

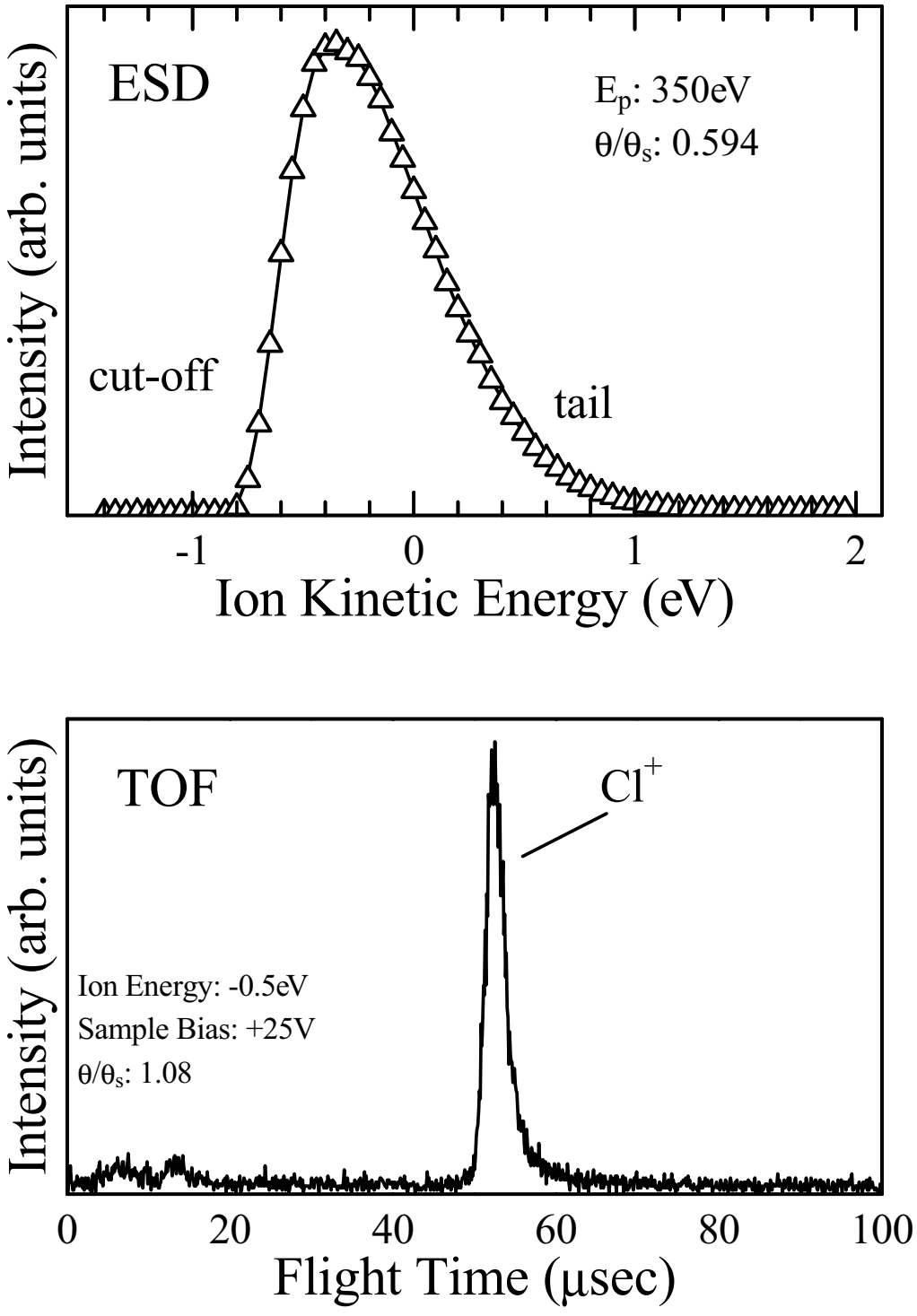

Figure 5.5 Upper: E_K distribution of the ion. Negative E_K value is due to the difference between the vacuum level of the sample and the analyzer. Below: TOF spectrum. Only Cl^+ is observed.

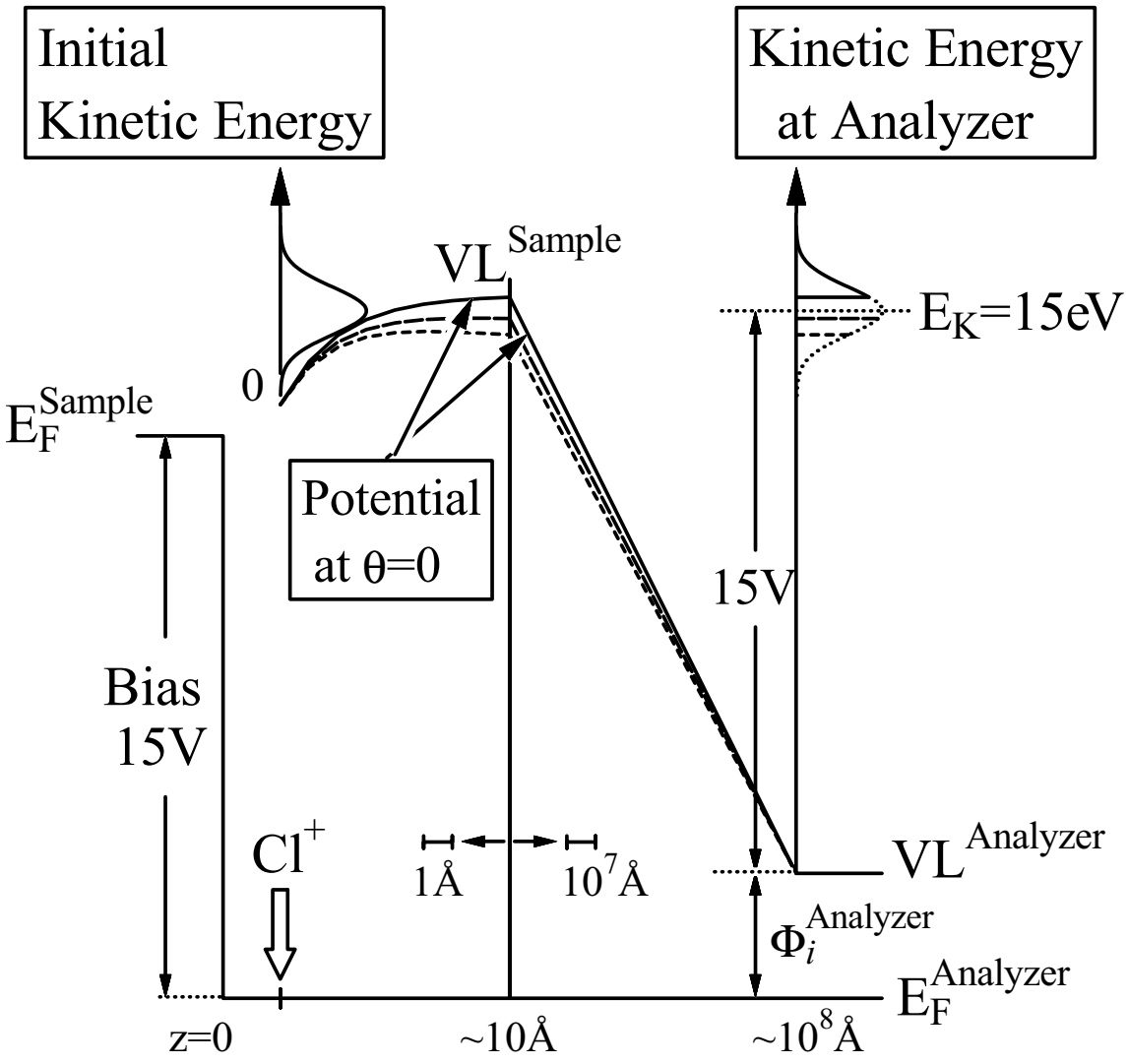

Figure 5.6 Schematic energy diagram of the present experiment. The origin of the negative kinetic energy of the ion is the vacuum level of the sample (VL^{Sample}) lower than the level 15eV higher than that of the analyzer($VL^{Analyzer}$).

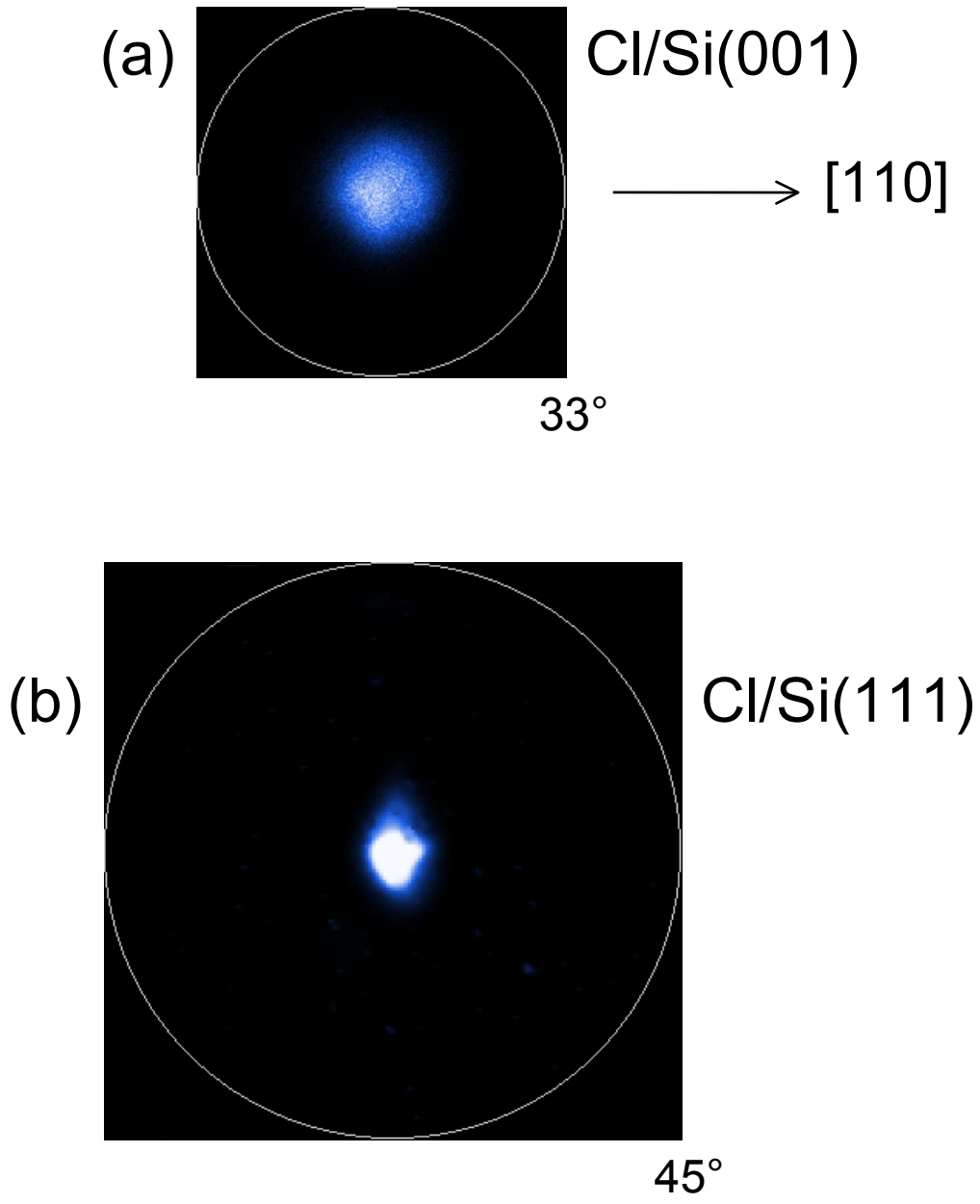

Figure 5.7 Observed ESDIAD patterns. (a): Cl^+ ions from nearly saturated Cl/Si(001) surface with sample bias of +15V. (b): Cl^+ ions from saturated Cl/Si(111) surface with sample bias of +70V. The angular distribution was almost the same in the case of LID. The circumference of each pattern corresponds to the acceptance angle of the analyzer estimated to be 33° and 45°, respectively.

pattern was obtained at the peak position of the E_K distribution. The desorbed ion was observed within the emission angle of $\sim 20^\circ$ which is a little bit wider than that in Cl/Si(111) case[20]. One can immediately recognize the normal emission of the ion but there seems to exist weak aprons towards [110] and [$\bar{1}$10] directions. This kind of feature has been already reported by some previous works [4, 6] in which the normal and off-normal distributions are assigned to the emission from the bridge or on-top site and the dangling bond site, respectively. We have to notice here that the relative intensity of the two different emissions does not directly give the practical existence ratio of the two adsorption sites because the cross section of the ionization would be different between them. Actually Gao *et al.*[4] suggest that the cross section is larger at the bridge site than at the dangling bond site.

The yield spectra of Cl^+ ion against the energy of the incident electron beam are shown in Fig.5.8; (a) on (111) and (b) on (001) surfaces. The Cl^+ yield are normalized by the sample current which increased with the incident electron energy. For both surfaces, a threshold is clearly seen between 10 and 20eV, which is more clearly seen in the PSD spectrum on (111) surface shown in the upper panel of Fig.5.9 to be 17eV. This excitation energy corresponds to the binding energy of Cl 3*s* core level as indicated in the UPS spectrum shown in the lower panel of Fig.5.9. From these results, it is considered that the excitation of Cl 3*s* core level to the conduction band triggers the Cl^+ desorption.

On (111) surface, the uptake behavior more than 20eV seems to saturate around 100eV which is near the Si 2*p* core level. There is another desorption threshold at around 200eV, which is considered to be due to Cl 2*p* core hole excitation.

The coverage dependence of the E_K distribution is shown in Fig.5.10. Each spectrum in the figure has been normalized at its peak maximum. The coverage dependence of the total yield was not measured quantitatively because the sensitivity of the detector had to be changed to obtain a good energy resolution. It is clearly seen that the cut-off position in lower E_K of each spectrum shifts to lower energies as the coverage increases. The tail of the higher energy region in the E_K distribution also shifts towards the same direction, although its magnitude is smaller than that of the shift of low energy cut-off. Figure 5.11 shows these energy shifts against the coverage where $\Delta\Phi^i$ and $\Delta\Phi^i$(tail) represent the magnitude of the shift of cut-off and tail, respectively. The increase of the work function $\Delta\Phi^e$ is also plotted.

The magnitude of cut-off shift $|\Delta\Phi^i|$ and that of work function $\Delta\Phi^e$ agrees very well. This agreement implies that there is an intimate relationship between the barrier height for the ion desorption and the surface dipole layer. In the case of Cl/Si(111) surface, $|\Delta\Phi^i|$

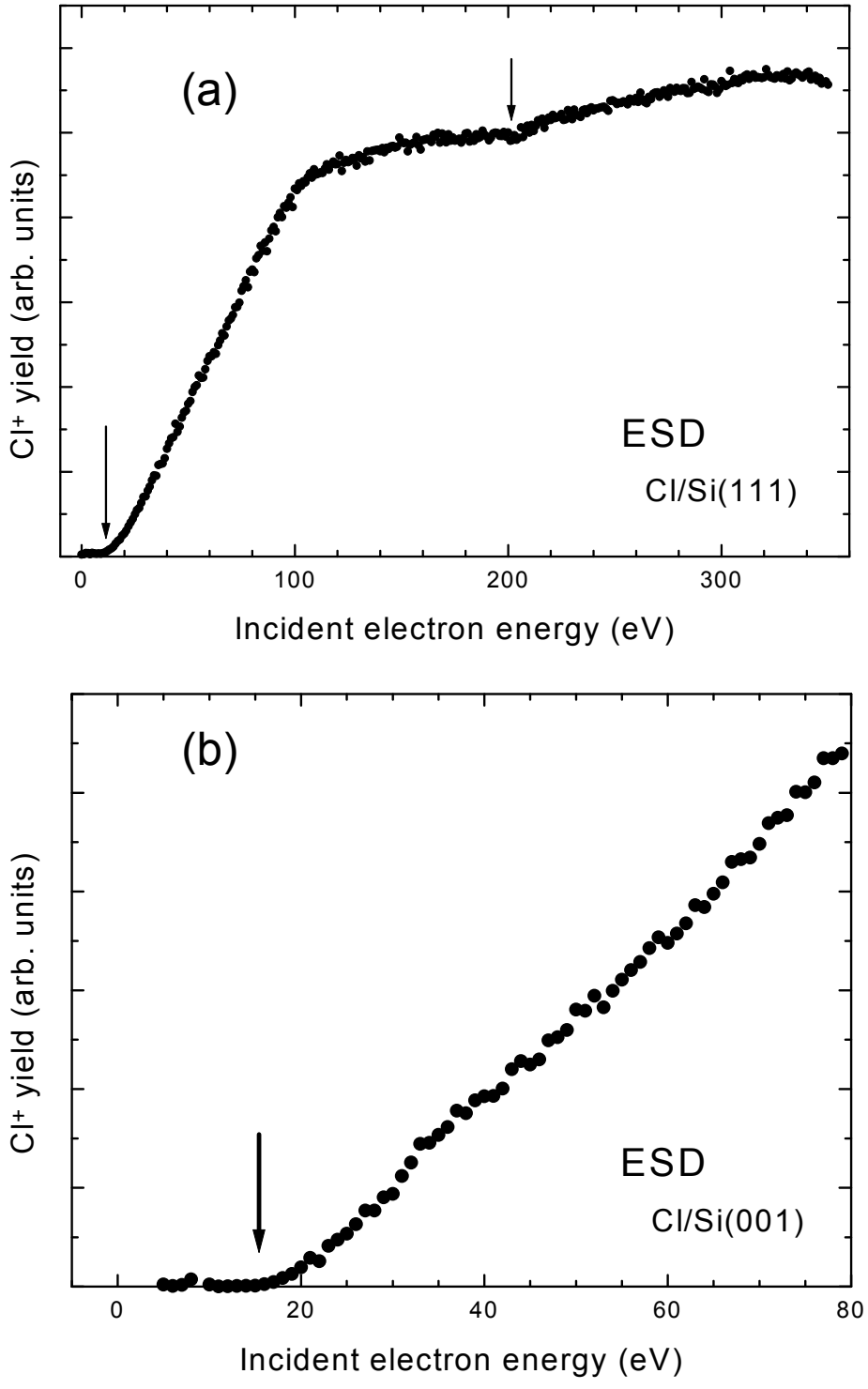

Figure 5.8 Incident electron energy dependence on Cl^+ yield from (a): Cl/Si(111) and (b): Cl/Si(001) surface. On Si(111), two stages of desorption are clearly distinguished which have thresholds at around 15eV and 200eV as indicated by arrows. A threshold at around 15eV is also observed on Si(001) surface.

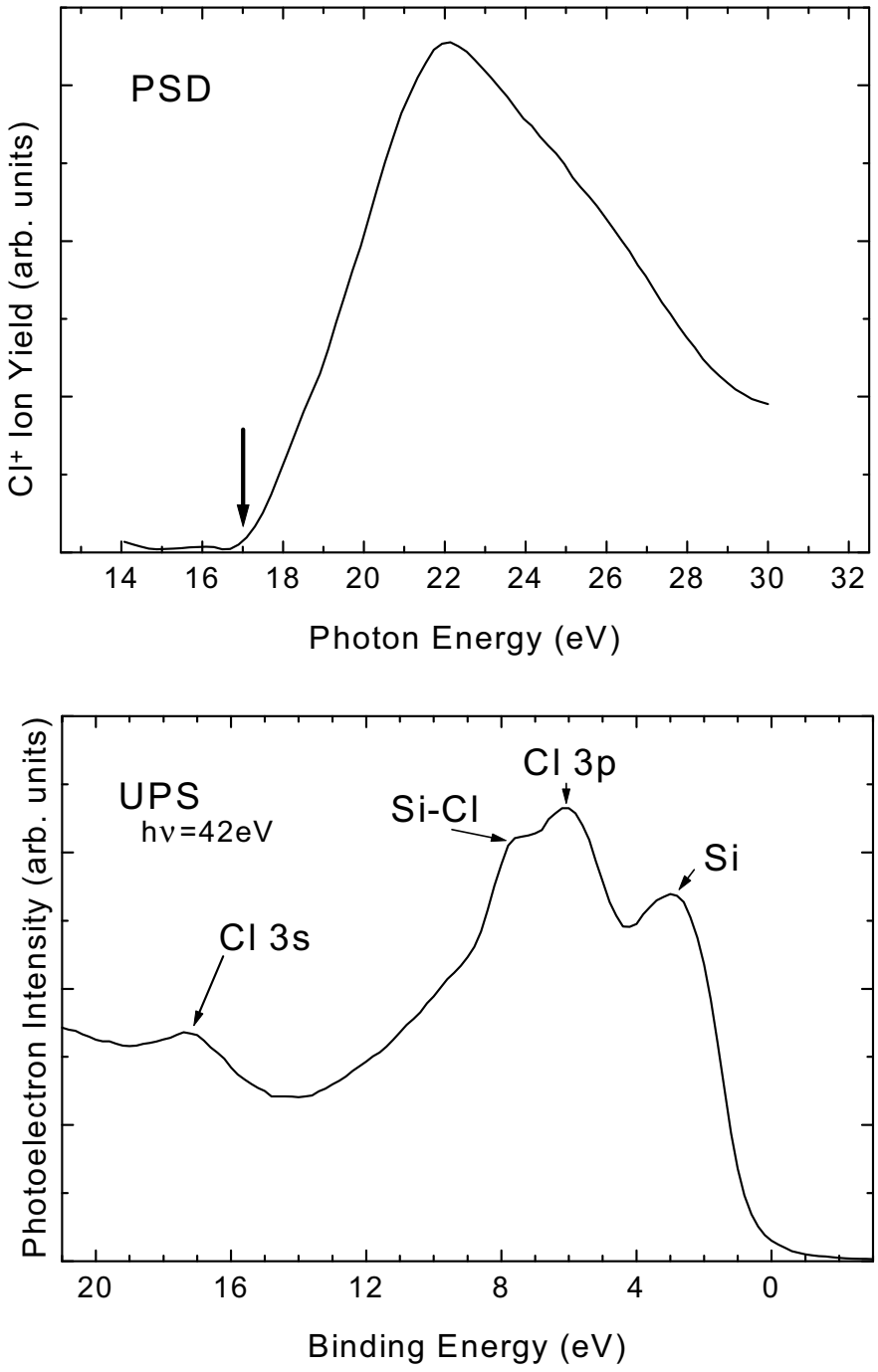

Figure 5.9 PSD and UPS spectra obtained by irradiation of synchrotron radiation onto Cl/Si(111) surface. Upper: Photon energy dependence of Cl^+ ion yield. A threshold at 17eV is clearly observed. Lower: UPS spectrum. The contribution from Cl 3s core level is around 17eV which corresponds to the excitation threshold of PSD.

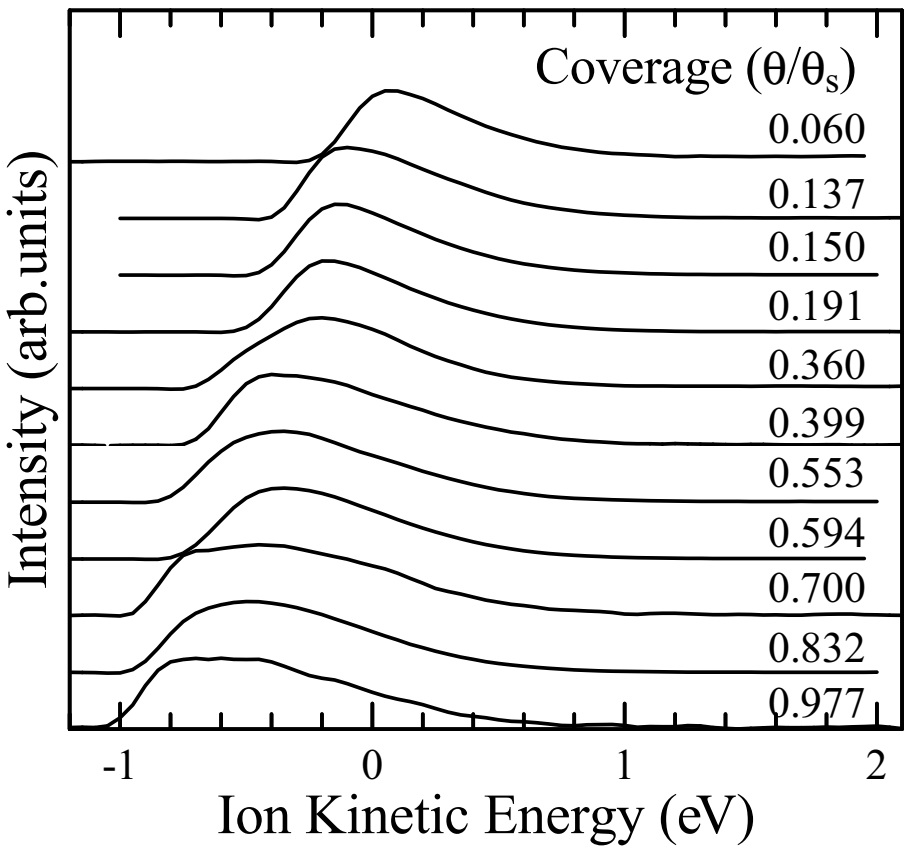

Figure 5.10 Coverage dependence of E_K distribution. Each spectrum has been normalized at its peak maximum.

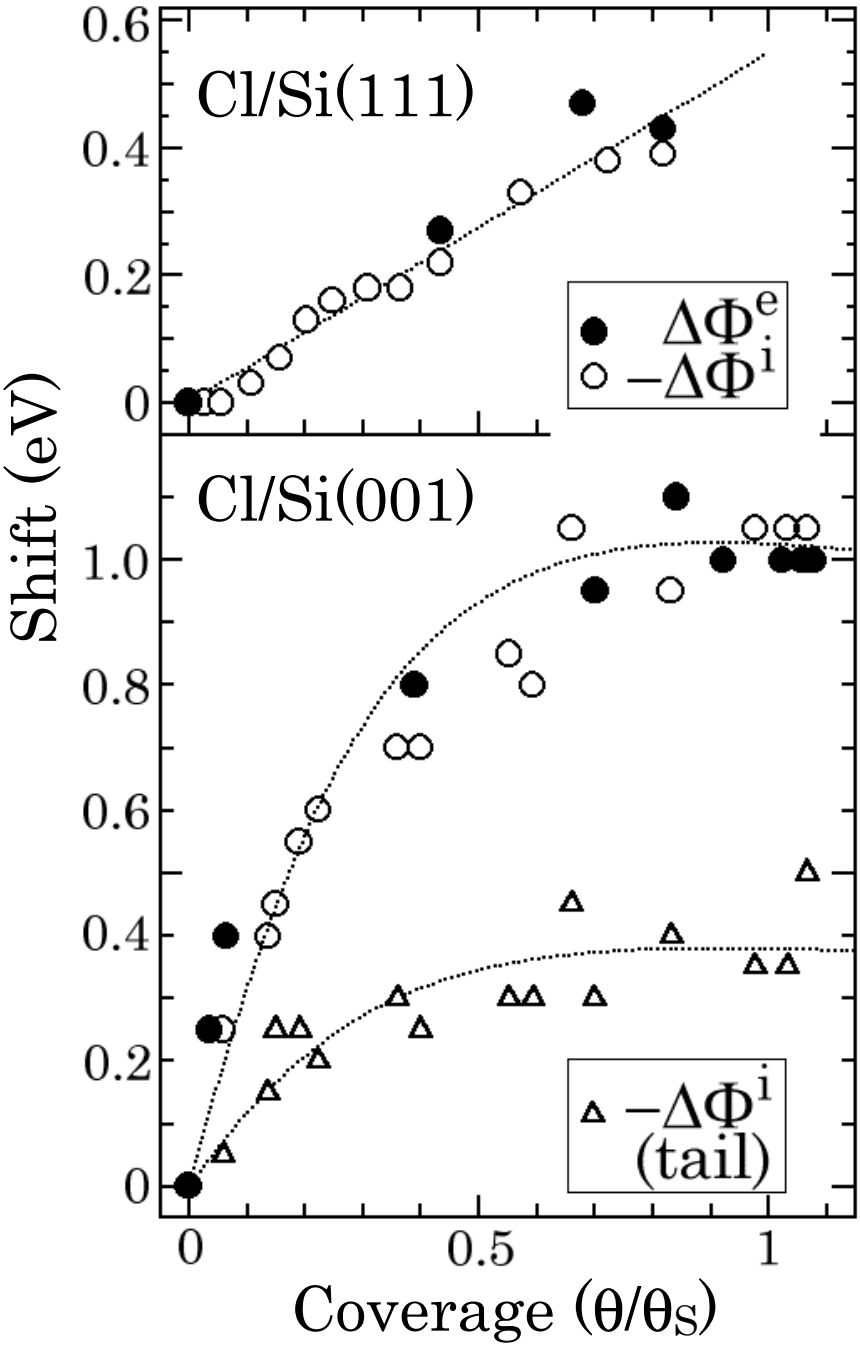

Figure 5.11 Coverage dependence of the change in E_K distribution of the ion and work function. Open and Solid circles denote the shift of cut-off and work function, respectively, although their signs are opposite. The shift of tail energy is also plotted in the case of (001) surface.

and $\Delta\Phi^{e}$ also show a good correspondence as shown in the same figure, although the tail energy hardly changed[19]. Comparing the results on these two surfaces, there are two interesting differences between them; one is the behavior of $\Delta\Phi^{i}$(tail) and another is the increasing lineshape. They will be discussed in detail in the following section, 5.4.3.

5.3.2 LID on Cl/Si(111) surface

The E_{K} distribution of the desorbed ions from Cl saturated Si(111) surface is presented in Fig.5.12 for the irradiation of laser and electrons. Laser fluence was estimated to be 100mJ/cm^2. The E_{K} distributions which are normalized at their peak height show comparatively good agreement about the cut-off position, peak position and FWHM. No other desorption peaks were observed up to 10eV except for the main peak at around 0eV . Figure 5.7(b) is the ESDIAD pattern of desorbed ion at the peak position. The acceptance angle at the circumference is almost 45° . Almost the same angular distribution was observed in the case of laser excitation in which the ion is distributed within a cone of $\sim$10° in the normal direction.

Taking into account the similarities in the E_{K} distribution and the angular distribution, the desorption species in LID is considered to be the same as in ESD, namely, Cl^{+} , although the mass analysis was not carried out. Moreover, it could be supposed that at least the final state of the desorption processes are very similar because the final E_{K} distribution is similar.

To obtain information about the desorption mechanism, laser fluence dependence of the yield of the ion was measured. The E_{K} distributions for four different fluences are shown in Fig.5.13. The intensity decreases with the decrease of fluence. The integrated intensity of these spectra are plotted logarithmically in Fig.5.14 against the fluence. Considering the uncertainty of both values of fluence and ion yield, the fitted line gives a minimum slope of 3 and maximum value of 4.3, which indicates the desorption of Cl^{+} occurs following 3- or 4-photon process.

5.4 Discussion

5.4.1 Adsorption process

The saturation coverage ($\theta/\theta_{\mathrm{S}}$) on (001) surface is still a matter of controversy. The increasing behavior of the coverage is similar to the report by Szabó *et al.* in which they suggest that the saturation coverage is larger under exposure of Cl atoms rather than

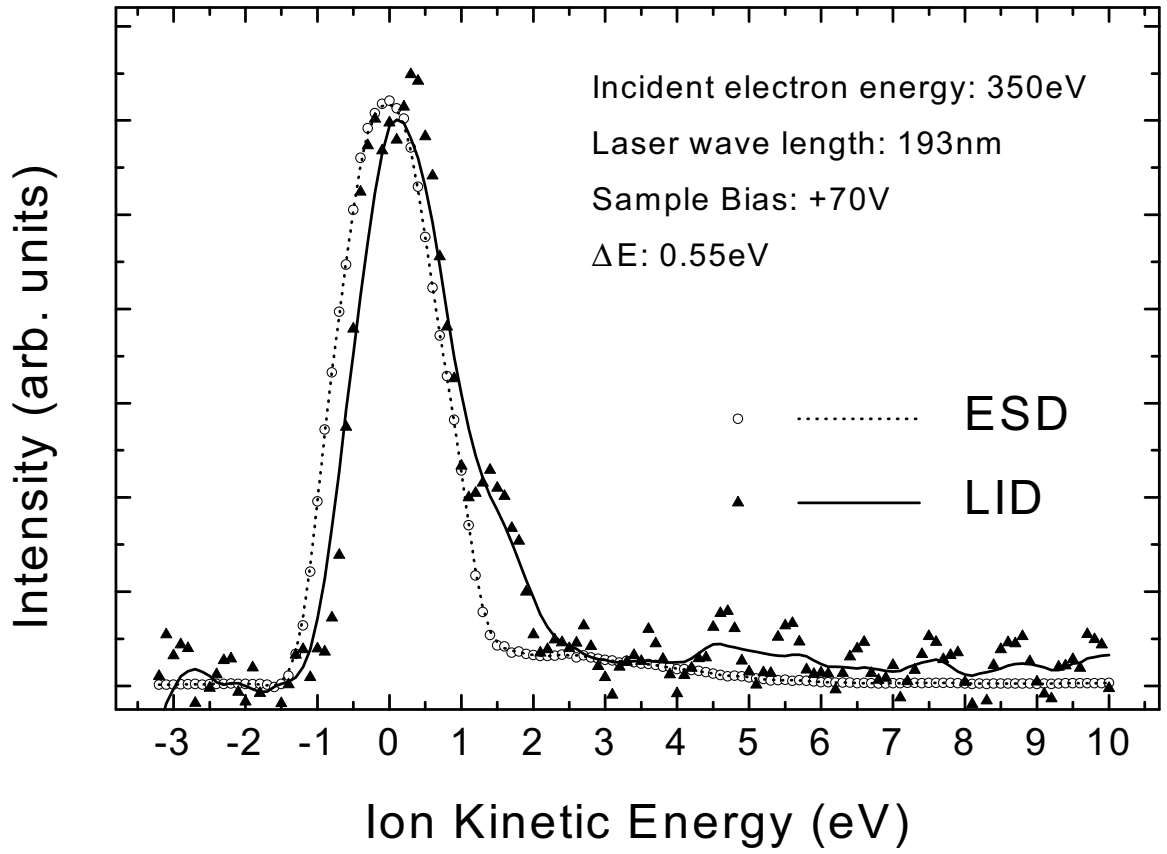

Figure 5.12 Comparison of the E_K distribution of ESD and LID. Each of them is normalized by its peak height. Two distributions are very similar in the line shape, peak position and FWHM.

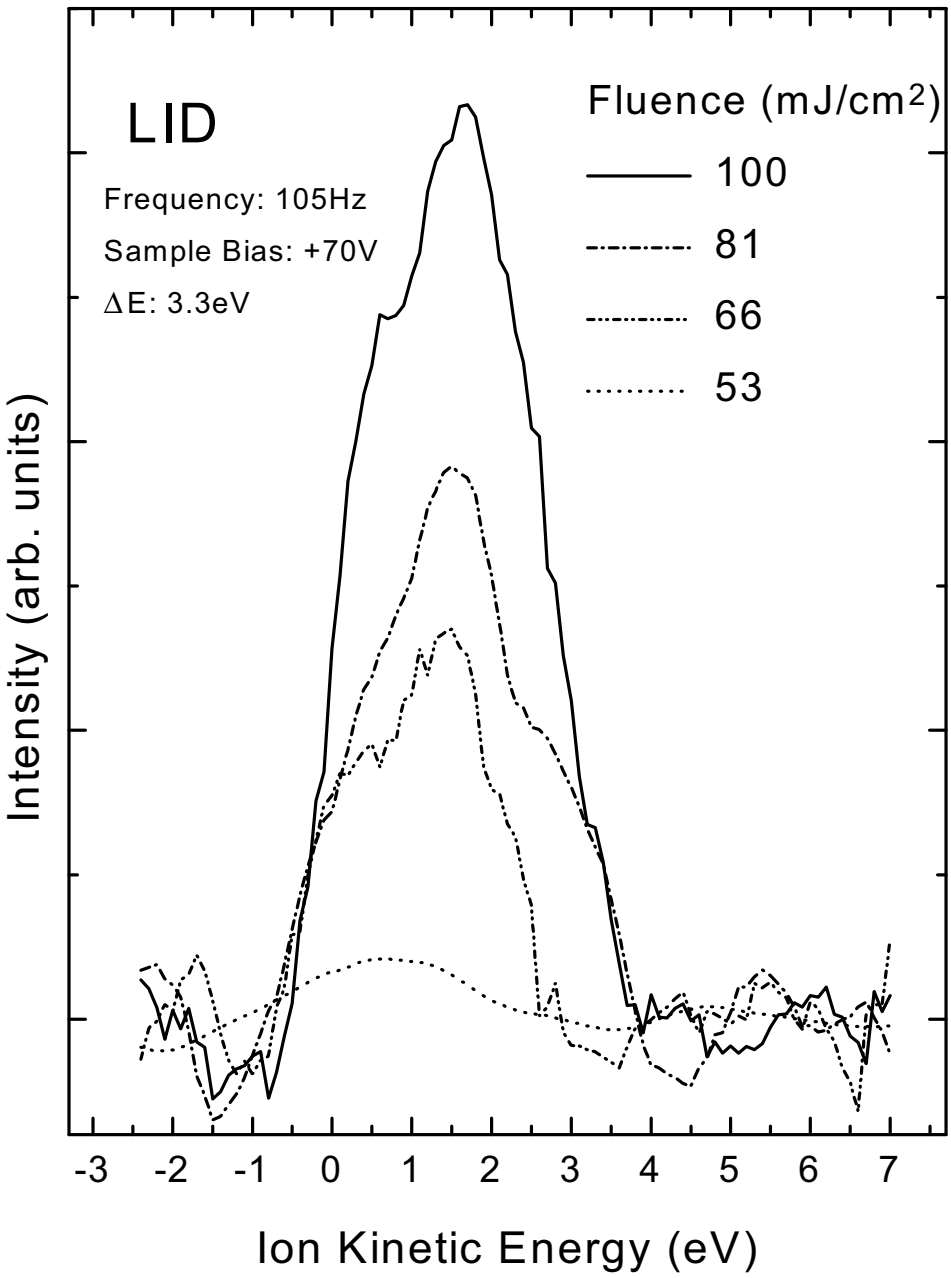

Figure 5.13 Laser fluence dependence of the E_K distribution. Total intensity attenuates with decreasing fluence.

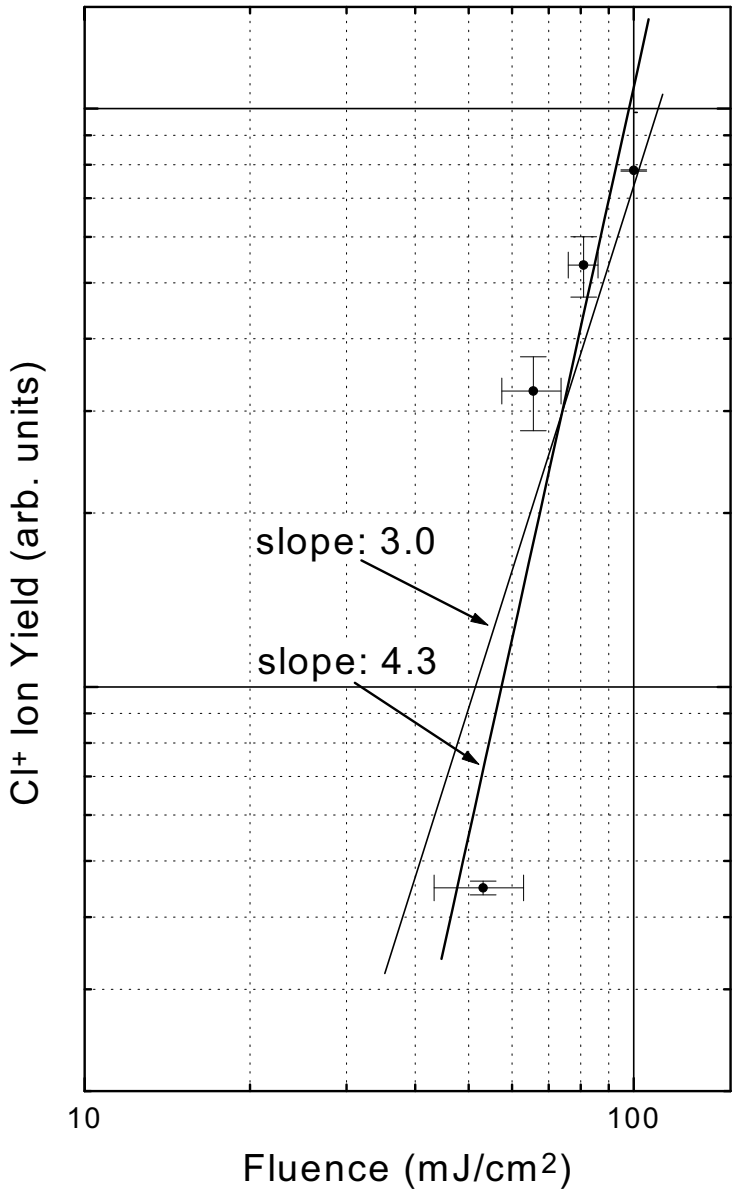

Figure 5.14 logarithmic plot of laser fluence dependence of Cl^+ ion yield. Experimental data are fitted to a line by the least squares method. The slope of the line 4.3 is the best fit suggesting a desorption mechanism with 4-photon process.

Cl_2 molecules[13]. In the present case, the ejected species from AgCl cell contain atomic chlorine as well as molecular one as shown in Fig.5.3. Therefore, we assume that the saturation coverage is 1ML considering the data on Cl atom adsorption in the Ref.[13].

As for (111) surface, the saturation coverage is estimated to be $\sim$ 1.5ML from the STM study[18]. At the saturation coverage, the existence of $SiCl_x$ ($x = 1, 2, 3$) has been reported[18].

The normal and some off-normal ion emission observed in ESDIAD pattern on (001) surface suggests the Cl adsorption at the dangling bond, bridge and on-top sites. The LEED pattern conversion from p(2×2) into 2×1 around 0.7ML suggests the extinction of periodic arrangement of the asymmetric dimer in the higher coverage region, and supports the Cl adsorption on the dangling bond and bridge sites of the symmetric dimer, whose total energy is calculated to be rather small[25]. The existence of $SiCl_2$, which has been suggested by core level PES study[10], is not denied considering the off-normal emission in the ESDIAD pattern.

The increasing behavior of the work function is different between (111) and (001) surfaces as shown in Fig.5.11. $\Delta\Phi^{\mathrm{e}}$ increases almost linearly to the coverage on (111) whereas it exhibits saturation behavior on (001) in the higher coverage larger than 0.7ML.

As to (001) surface, the saturation behavior is considered to be related to the interaction between Si-Cl dipoles. The dashed line in Fig.5.11 is fitted by a simple assumption that the dipole layer is described in terms of a uniformly charged planes like a parallel plate capacitor as

$$|\Delta\Phi| = \frac{p n_{\mathrm{dip}}}{\epsilon_0}\left[1 + \frac{9\alpha n_{\mathrm{dip}}^{3/2}}{4\pi\epsilon_0}\right]^{-1}, \tag{5.2}$$

where n_{dip}, p and α are the density of dipoles, the dipole moment and the polarizability of the dipole, respectively[26]. This equation contains the interaction between the dipoles suggesting that the observed saturation behavior of $\Delta\Phi^{\mathrm{e}}$ would owe to the reduction of each dipole moment.

On the other hand, there is also a difference in the adsorption behavior between the cases of (001) and (111) surface as shown in Fig.5.4. On (001) surface, the adsorption rate is constant under the saturation, whereas it gradually decreases on (111) surface.

These differences would be explained by considering the total energy of the system which will increase with the coverage by the interaction between the surface dipoles. On (111) surface, the dipole moment is presumed to be constant so that the adsorption rate decreases to prevent the increase of the total energy. On the other hand, the constant adsorption rate on (001) surface is reasonable, considering the reduction of the dipole

moment with increasing coverage. This could be occur by a charge reconstruction in the same fashion as seen in alkali-metal adsorbed Si surface[27].

5.4.2 Desorption mechanism

In Fig.5.8 and Fig.5.9, there exist thresholds in Cl^+ yield at 17eV, which corresponds to the excitation energy from Cl 3s core level to the Fermi level or upper lying conduction bands. Since the excitation of the core hole is considered to trigger the desorption of the positive ion, ASID model[28] would be sufficient to describe this desorption mechanism, namely, (1) Cl 3s core hole excitation, (2) intra-atomic Auger decay, (3) creation of two holes in the Si–Cl bonding orbital such as σ-bond which lies 8.2eV below Fermi level[2], leading to Cl^+ ion desorption due to Coulomb repulsion. This interpretation is also suggested by recent reports [10, 29]. Although the measured E_K of at most 1eV seems to be contradictory to the estimated E_K of 7.2eV derived from Coulomb repulsion force, the image potential of Cl^+ itself or the fast screening effects of the created hole could reduce the observed E_K . Another threshold on (111) surface at 200eV corresponding to Cl 2p edge is also assigned to the desorption via ASID process[20].

Some papers presented the evidence of indirect desorption process[9, 10], XESD, following the excitation of Si 2p hole in their PSD study. In the present results, no prominent threshold was observed at Si core level related energies. Comparing the line shape in the case of ESD with PSD, shown in Fig.5.9, the latter has its maximum at around 22eV, while the former gradually increases up to around 100eV. The maximum in PSD was ascribed to the absorption from Cl 3s to Cl antibonding orbitals[10]. The gradual increase in ESD would possibly have its origin in either the Cl 3s excitation by secondary electrons of incident electron or the increase of the cross section of Cl 3s excitation. Guo *et al.* supported the latter from their measurement of secondary electron yield[29].

In LID study, laser fluence dependence showed that the desorption mechanism is 3- or 4-photon process. Since the one-photon energy is 6.4eV, 3-photon (19.2eV) and 4-photon (25.6eV) processes imply that the desorption initiates from Cl 3s core hole excitation as in the case of ESD and PSD. However, one has to be careful whether such nonresonant multiphoton ionization is possible or not.

Generally, n-photon absorption cross section $\sigma[\mathrm{W}^{-n}\mathrm{cm}^{2n}\mathrm{s}^{-1}]$ is described as

$$\frac{dx_\mathrm{e}}{dt} = -\sigma I^n x_\mathrm{g} \ , \tag{5.3}$$

where x_e and $x_\mathrm{g}[\mathrm{atoms/cm}^3]$ are the number of atom in excited and ground state, respectively, and $I[\mathrm{Wcm}^{-2}]$ is the laser intensity. Using the values of laser duration $t_\mathrm{d} = 5$ns and

$x_g = 10^{13}$[atoms] which is the number of atom within spot area of the incident laser, the practical cross section ($\sigma I^n t_d$) and x_e per pulse ($\sigma I^n t_d x_g$) are tabulated in Table 5.1. For comparison, the values for PSD experiment are also tabulated using pulse width of synchrotron radiation $t_d = 1$ns. Here, σ is for Xe atom which was evaluated from Refs.[30, 32],

n	σ	I	$\sigma I^n t_d$	$\sigma I^n t_d x_g$	2 hole
1	1	10^7	10^{-1}	10^{12}	10^6
2	10^{-10}		10^{-4}	10^9	1
3	10^{-23}		10^{-10}	10^3	10^{-12}
4	10^{-36}		10^{-16}	10^{-3}	10^{-24}
1 (SR)	10^1	10^{-7}	10^{-16}	10^{-3}	10^{-24}
2 (SR)	10^{-10}		10^{-32}	10^{-19}	10^{-56}

Table 5.1: n-photon absorption cross section of Xe atom

because the value for Cl is not so different within the order of magnitude shown in the table.

From the table, one can immediately recognize that even if the process is 3-photon absorption, lots of ions in the order of 3 is created. However, we have to notice that the tabulated values are considered to be for the excitation of Xe $5p$ orbital. In the case of $5s$ orbital, σ is smaller at the photon energy around 20eV as shown in Fig.5.15[31]. Nevertheless, the desorption induced by Cl $3s$ core hole is not denied since σ for Cl $3s$ orbital is smaller than that of $3p$ in the order of 3[32] resulting in one excited atom. Therefore, ASID model initiated by Cl 3s core hole excitation by 3-photon absorption is also applicable to Cl^+ desorption in LID.

On the other hand, a possibility of the valence band excitation[29] cannot be denied. Considering a requirement that the final state of the process must be similar to that of ESD from E_K distribution analysis, one possibility is the double 2-photon absorption from Si–Cl bonding level to the conduction band resulting in a localized two hole state. The number of atoms excited by such a process is also evaluated in table 5.1, assuming the life time of the created hole to be $\sim 10^{-14}$s. From the table, the double 2-photon absorption process is recognized to be a possible path of the ion desorption. The desorption via this process cannot occur in the PSD study since the cross section is too small. 2-photon absorption which has a threshold at 12.8eV is also impossible in PSD because the cross section is almost negligible as shown in Table 5.1.

Possible desorption processes in the present results are summarized in Fig.5.16.

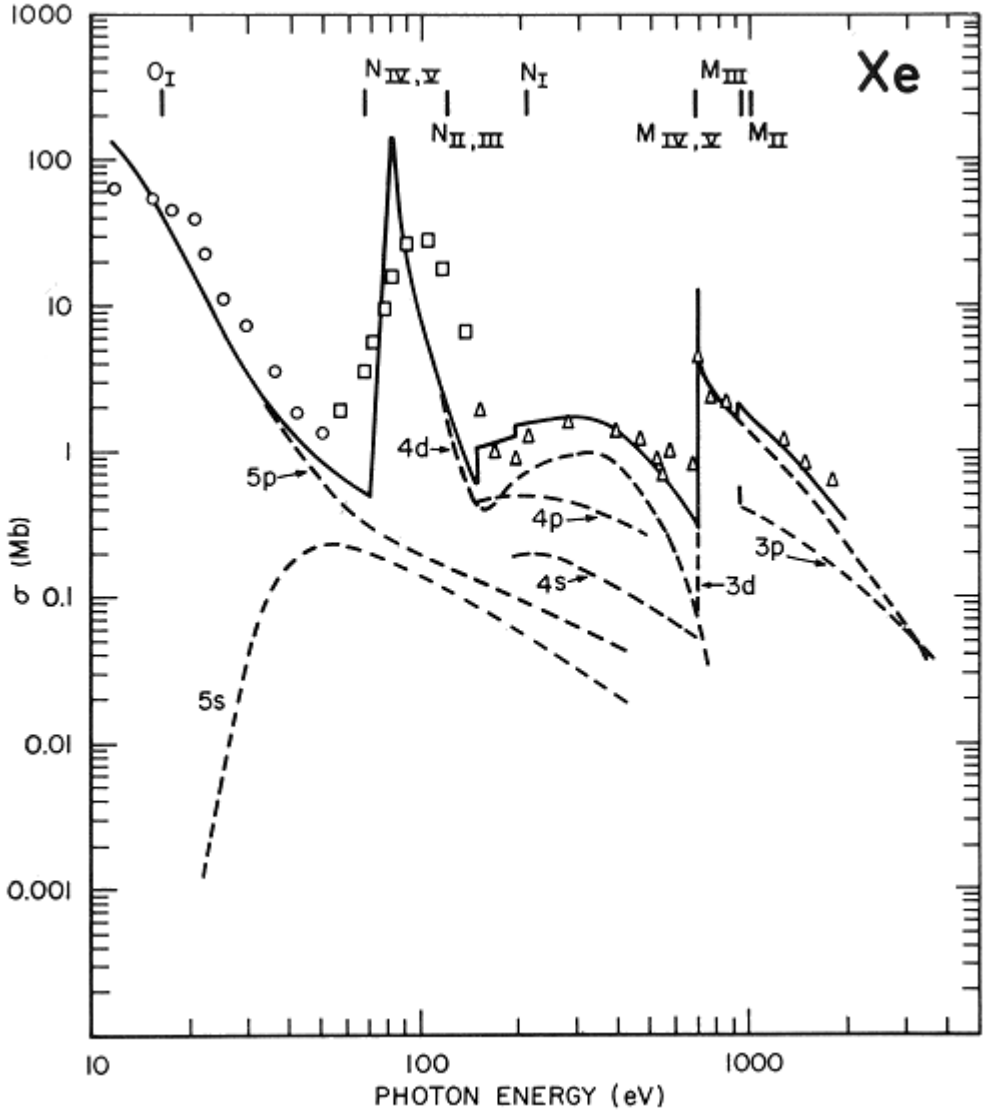

Figure 5.15 Photoionization cross section of Xe atom (Ref.[31]).

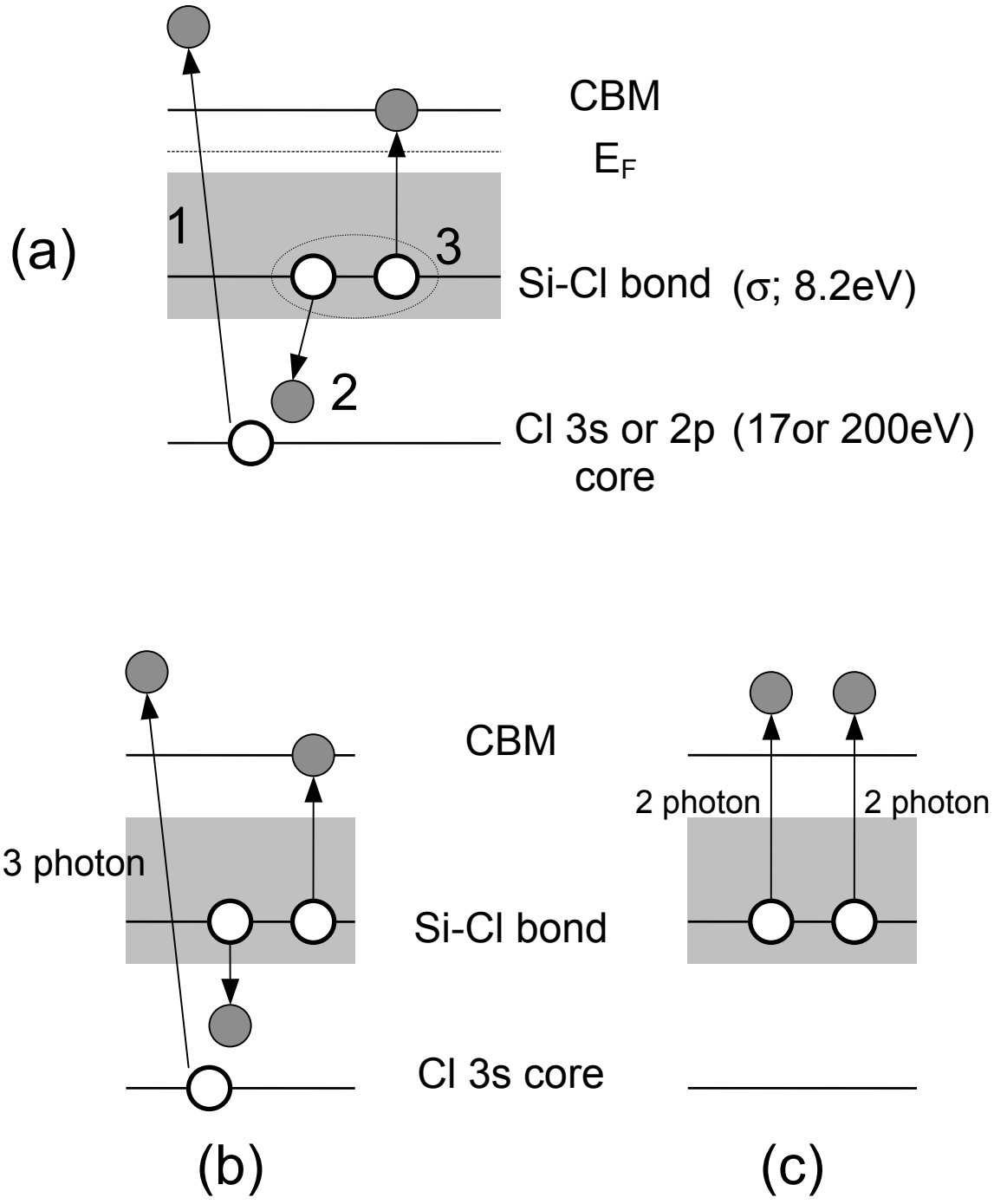

Figure 5.16 Schematic energy diagrams of possible DIET processes in the present results. (a): ASID process observed in ESD and PSD. 1.Cl core hole excitation, 2.intra-atomic Auger decay, 3.consequent localized two holes in Si-Cl bond resulting in Cl^+ desorption by Coulomb repulsion. (b): The same mechanism in LID via 3 photon process. (c): One possible process in LID including direct two hole excitation in Si-Cl bond by double 2-photon process.

5.4.3 Influence of surface dipole layer on ion desorption

The characteristic behavior observed in the coverage dependence of cut-off and tail of E_{K} distribution as well as work function shown in Fig.5.11 indicates an important correlation between the barrier height of the ion desorption and the dipole layer induced by electronegative Cl adsorption. The image potential barrier for the desorbing ion would be reduced by dipole creation. Regarding cut-off shift, the same behavior has been reported recently by Simpson *et al.*[33] in which they give the explanation using eq.(5.2). However, the assumption of uniformly charged planes as the dipole layer in eq.(5.2) cannot explain the coverage dependence of the tail position.

To solve this problem, two types of dipole layer are considered. One is a pair of uniformly charged planes, while another consists of individual, discrete dipoles. Although the latter idea of discrete dipole has been presented by Gomer[34] to explain the work function change in field emission, it is applied to the positive ion desorption utilizing its local character.

In Fig.5.17, calculated potentials for the desorbing ion from these two types of dipole layers are presented. The dashed line shows the potential change in the uniformly-charged-planes model. The solid lines are those in the discrete dipole model for four d/ℓ values where d and 2ℓ are the mean lateral distance between adjacent dipoles and the dipole length, respectively.

The calculated potential for the discrete dipole model is a simple sum of Coulomb potential from surrounding 40,000 dipoles consist of $\delta+$ and $\delta-$ point charges. Only the potential on emitted Cl^+ along normal direction was employed considering the result of ESDIAD pattern. The dipoles were arranged on the triangle and square lattice of ideal (111) and (001) surface, respectively. The potential on Cl^+ from formerly bound $Si^{\delta+}$ atom was ignored because Coulombic repulsive potential is included in the E_{K} . In the figure, only the potential curves for (111) surface are presented, but those for (001) surface are very similar.

In the case of uniformly-charged-planes model, the potential change has completed at Cl adsorption site ($z/\ell = 2$), while in the discrete dipole model, it is negligible or very small compared to that at far from the surface. The potential for the desorbing ion is considered to be a simple sum of the image potential of itself and the potential from surface dipoles. The whole energy diagram is schematically shown in Fig.5.18.

Figure 5.18(a) shows the potential curve at very low coverage and is reproduced in (b) and (c) by dashed lines. Figure 5.18(b) and (c) show the potentials in the uniformly-

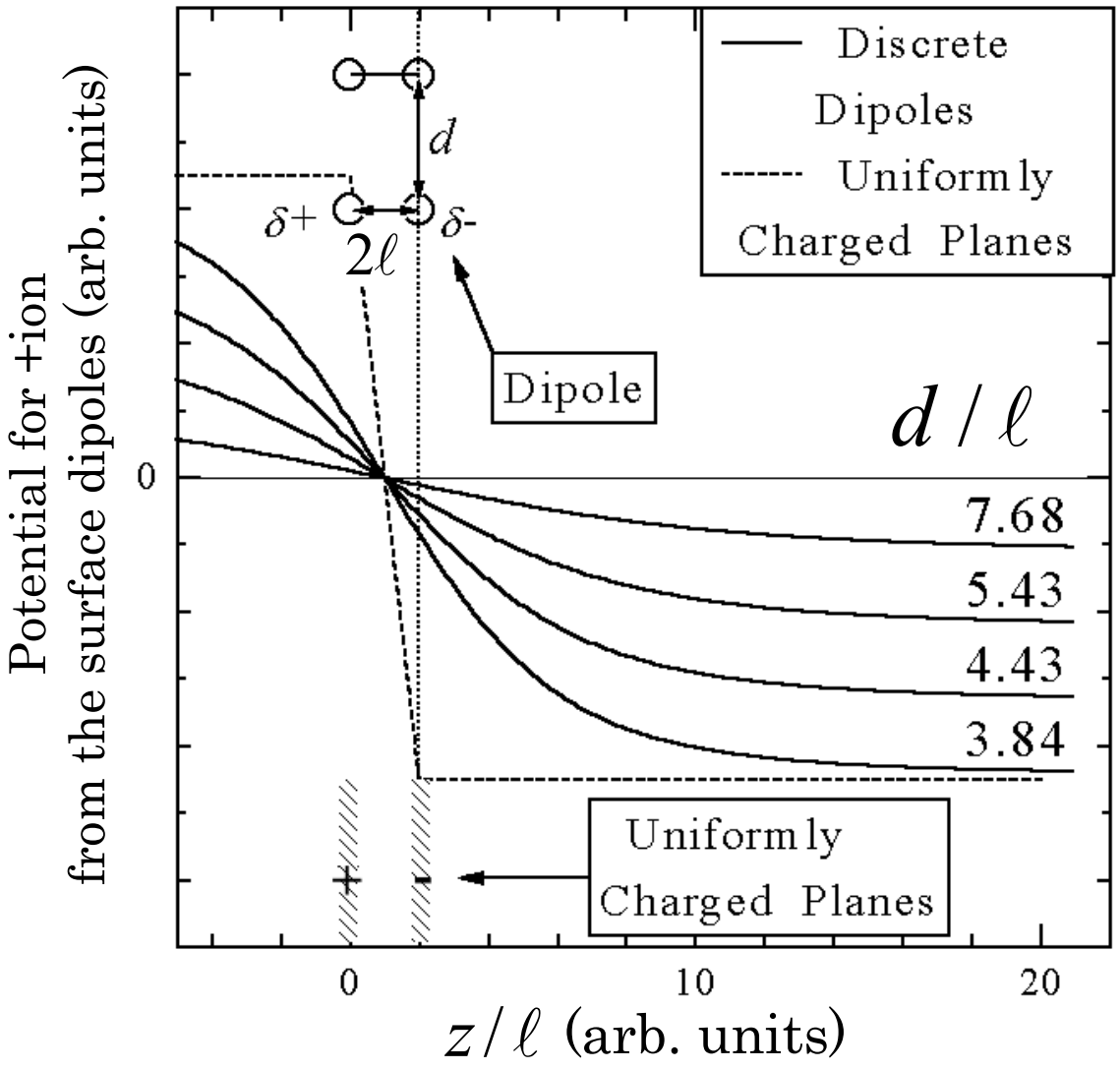

Figure 5.17 Calculated potential for desorbing positive ion from dipole layer. Horizontal axis is the distance from the surface in ℓ unit. The values 2ℓ and d represent the dipole length and the mean lateral distance between adjacent dipoles, respectively. Calculated potential for uniformly charged planes model and discrete dipole model are denoted by dashed line and solid lines, respectively.

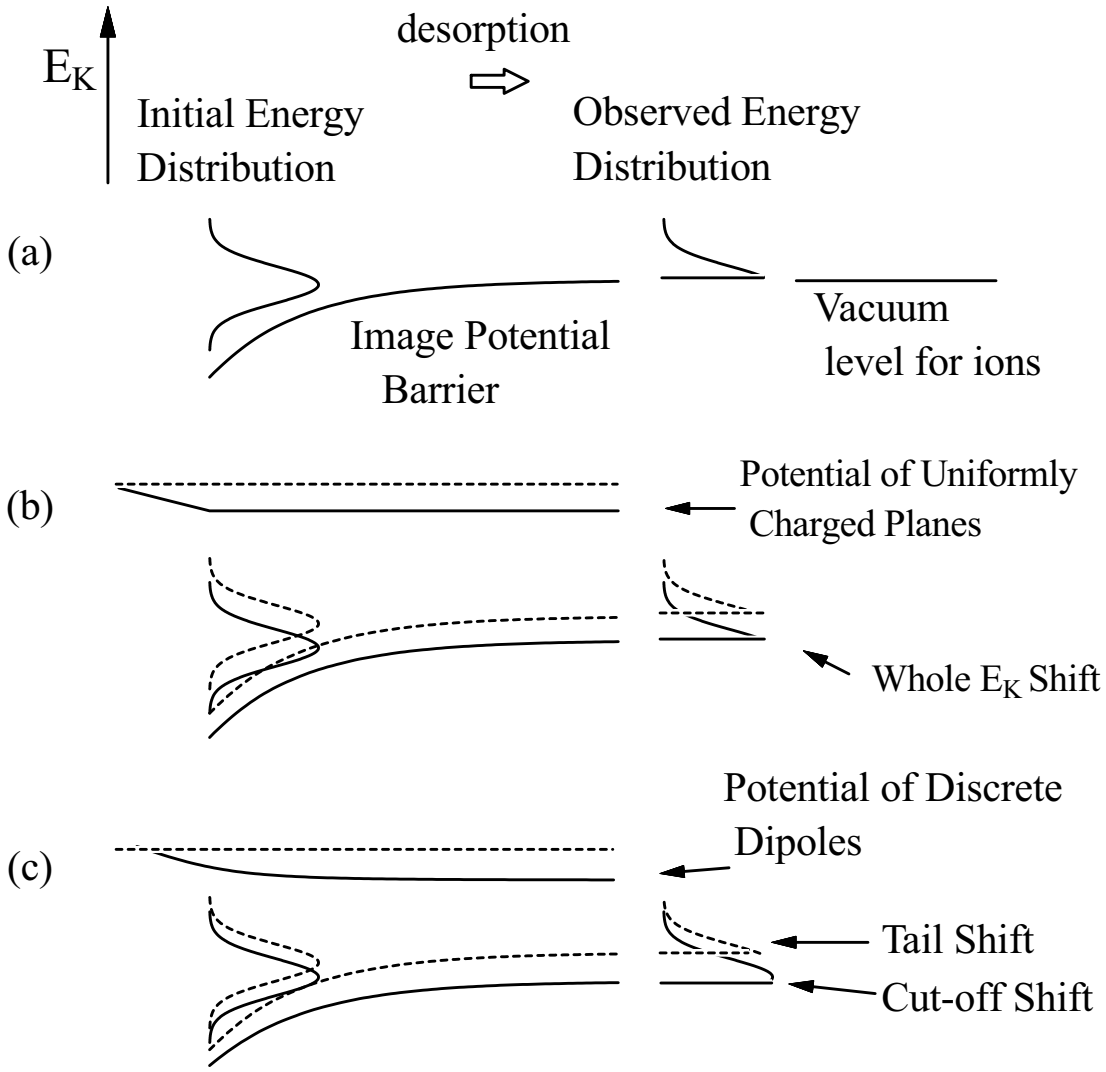

Figure 5.18 Schematic view of the dipole potential effect. (a) is the potential at very low coverage. (b) and (c) are the potential at saturation coverage in uniformly charged planes model and discrete dipole model, respectively. The cut-off energy shift equals to the tail energy shift in (b), which is not in agreement with experimental result. In contrast, the tail shift is sufficiently smaller than the cut-off shift in (c), which is adequate.

charged- planes model and the discrete dipole model, respectively. For each case, the image potential barrier is lowered by the dipole potential, and the cut-off energy shifts towards lower energy. Therefore, the magnitude of the cut-off shift corresponds to the potential change due to the dipole layer at far from the surface, and is equal in both models. On the other hand, the magnitude of the tail shift is the same as the potential change at Cl adsorption site. In the uniformly-charged-planes model, the cut-off shift and the tail shift have the same value as shown in (b), which is contradictory to the experimental result. In Fig.5.18(c), the tail shift has a small value compared to the cut-off shift, and the experimental result can be well explained. Hence, the discrete dipole model is the adequate nature.

We can estimate the dipole length from the measured ratio of the tail shift to the cut-off shift in Fig.5.11. This ratio is about 0.38/1.03 on (001) surface and almost negligible on (111) surface. Considering the calculated potential curves in Fig.5.17 and the experimental uncertainty of the tail shift energy of 0.3eV in the case of (001) surface, d/ℓ is greater than 4.43 for (111) and is around 1.72 (not shown) for (001) surface. Assuming the saturation coverage on both surfaces to be 1ML, the value d is 3.84Å . Consequently, the dipole length 2ℓ on the two surfaces are estimated to be less than 1.73Å and approximately 4.5Å for (111) and (001) surfaces, respectively.

The origin of the dipole is discussed as follows. Considering the potential curve in Fig.5.17, if the dipole consisted of $Cl^{\delta-}$ and $Si^{\delta+}$, the magnitude of the change of the work function would be as twice as that of cut-off since electrons had to be emitted from inside the bulk along the potential curve. This is inconsistent with the experimental result. The dipole of $Cl^{\delta-}$ and its image charge $\delta+$ is able to solve the problem because there exists no potential change inside the image plane, $z/\ell = 1$. Such a situation takes place for a system with a large dielectric constant.

Since the bond-length of Si-Cl is 2.0Å determined by EXAFS [35], the evaluated dipole length on (111) surface of 1.73Å seems to be natural. On the contrary, on (001) surface, 4.5Å seems to be too long as a dipole length compared to the bond-length. One possibility is an over-estimation of the length, because the change of the surface band bending by Cl adsorption has not been considered. The energy diagram of the band bending and the potential for the discrete dipole model is schematized in Fig.5.19. Here, we assume that the band bending is lowered by Cl adsorption and the reduction of it is equal to ΔV_S on both p- and n-type substrates. On p-type (n-type) surface, one has to get rid of (add) this value (ΔV_S) from (to) the measured variation of the work function ($\Delta\phi^i$) to estimate

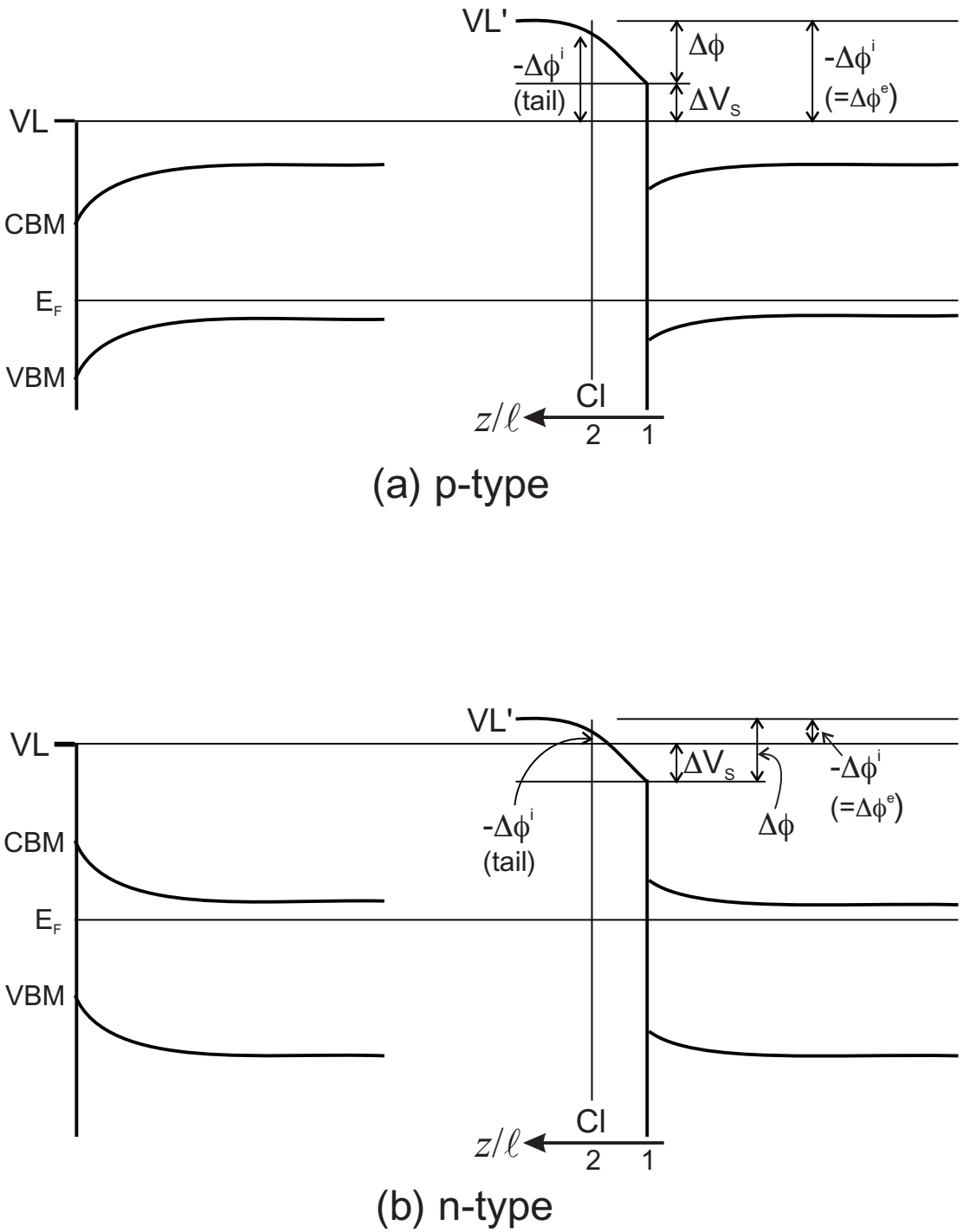

Figure 5.19 The influence of the change of the band bending (ΔV_S) to the measured values of the chage of the work function ($\Delta\phi^e$). (a) is for p-type substrate while (b) is for n-type. The energy diagrams at the left and right side represent those for the clean and chlorinated surfaces. To estimate the correct value of the potential induced by the surface dipole layer ($\Delta\phi$), one has to get rid of (add) ΔV_S from (to) $\Delta\phi^e$ in the case of p-(n-)type substrate.

the correct value of the potential of the surface dipole layer on the Cl saturated surface ($\Delta\phi$). The experimental result on n-type Si(001) surface presented the tail/cut-off ratio of 0.17/0.76 at most. Assuming $\Delta\phi$ on the p-type substrate is equivalent to that on the n-type one, the reduction of the band bending is evaluated to be 0.14eV, (0.5eV[2]). Accordingly, the intrinsic values of tail/cut-off ratio on p- and n-type surfaces are estimated to be 0.27 and 0.34 and the dipole length on (001) surface results in 3.2-4.1Å from discrete dipole model. This value is still longer than the bond length. The difference between (111) and (001) surfaces may have the origin in a different electronic properties of the clean surfaces, i.e., metallic and semiconductive, respectively, or in a different local charge distributions.

5.5 Summary

The adsorption and desorption processes of ESD and LID on chlorinated silicon surface was investigated. The ESD data for Cl/Si(001) surface was compared to our previous results on Cl/Si(111) surface.

In the adsorption process, constant sticking coefficient up to the saturation coverage ($\sim$1ML) was observed by AES on (001) surface, whereas that on (111) surface gradually decreased until the saturation according to Langmuir's equation. On the other hand, the increasing behavior of the work function due to Cl adsorption was almost linear to the coverage on (111), while non-linear behavior of saturation was observed on (001). From these characteristic differences in (001) and (111) surface, it is indicated that the increasing interaction between the created dipoles reduces the adsorption probability on (111) surface, whereas the reduction mechanism of each dipole moment maintains the constant adsorption rate on (001) surface. The previously reported Cl adsorption on the dangling bond and bridge sites were supported by LEED and ESDIAD analysis.

A preferential desorption of Cl^+ either by electron or laser irradiation was revealed. Its mechanism is described by ASID model including the excitation of Cl $3s$ and $2p$ core hole and successive intra-atomic Auger decay. The desorption initiated by valence band excitation is not denied in LID process, within the condition that the final state of two hole localization in Si–Cl bond should be contained.

The E_{K} distribution of desorbed ion and the work function showed a characteristic dependence on Cl coverage both on (111) and (001) surfaces in which the magnitude of the shift of high energy tail in the E_{K} distribution is much smaller than that of low energy cut-off and the work function. This feature is not explained by assuming general dipole layer like a flat plane condenser, but by the discrete dipole model which treats the dipole

as individual charge distribution. Although more precise measurement in higher energy and angular resolution is needed to completely establish this picture, the discrete dipole model emphasizes one of the aspects of ESD method as an atomic scale probe of the charge distribution on the solid surface.

References

[1] J. E. Rowe, G. Margaritondo and S. B. Christman, Phys. Rev.**B16** (1977) 1581.

[2] L. S. O. Johansson, R. I. G. Uhrberg, R. Lindsay, P. L. Wincott and G. Thornton, Phys. Rev.**B42** (1990) 9534.

[3] N. Aoto, E. Ikawa and Y. Kurogi, Surf. Sci.**199** (1988) 408.

[4] Q. Gao, C. C. Cheng, P. J. Choyke and J. T. Yates,Jr., J. Chem. Phys. **98** (1993) 8308.

[5] J. J. Boland, Science **262** (1993) 1703.

[6] S. L. Bennett, C. L. Greenwood and E. M. Williams, Surf. Sci.**290** (1993) 267.

[7] D. Purdie, N. S. Prakash, K. G. Purcell, P. L. Wincott and G. Thornton, Phys. Rev.**B48** (1993) 2275.

[8] Z. Dohnálek, Q. Gao, W. J. Choyke and J. T. Yates, Jr., Surf. Sci.**320** (1994) 238.

[9] D. Sterratt, C. L. Greenwood, E. M. Williams, C. A. Muryn, P. L. Wincott, G. Thornton and E. Román, Surf. Sci.**307-309** (1994) 269.

[10] T. D. Durbin, W. C. Simpson, V. Chakarian, D. K. Shuh, P. R. Varekamp, C. W. Lo and J. A. Yarmoff, Surf. Sci.**316** (1994) 257.

[11] R. D. Schnell, D. Rieger, A. Bogen, F. J. Himpsel, K. Wandelt and W. Steinmann, Phys. Rev.**B32** (1985) 8057.

[12] J. J. Boland and J. S. Villarrubia, Science **248** (1990) 838. J. J. Boland and J. S. Villarrubia, Phys. Rev.**B41** (1990) 9865.

[13] A. Szabó, P. D. Farrall and T. Engel, Surf. Sci.**312** (1994) 284, and references therein.

[14] T. N. Rhodin, C. Paulsen-Boaz and W. L. O'Brien, Surf. Sci.**283** (1993) 109.

[15] M. Suguri, T. Hashizume, Y. Hasegawa, T. Sakurai and Y. Murata, J. Phys.: Condens. Matter**4** (1992) 8435. M. Suguri, K. Shudo, F. Komori and Y. Murata, J. Phys.: Condens. Matter**5** (1993) 6607.

[16] K. Hattori, K. Shudo, T. Iimori, F. Komori and Y. Murata, J. Phys.: Condens. Matter **8** (1996) 6543.

[17] K. Shudo, F. Komori, K. Hattori and Y. Murata, Surf. Sci.**320** (1994) 161.

[18] F. Komori and K. Hattori, Proc. SPIE Int. Soc. Opt. Eng., **2547** (1995) 285.

[19] T. Yonezawa, H. Daimon, K. Nakatsuji, K. Sakamoto, S. Suga, H. Namba and T. Ohta, Jpn. J. Appl. Phys. **33** (1994) 2248.

[20] T. Yonezawa, H. Daimon, K. Nakatsuji, K. Sakamoto and S. Suga, Appl. Surf. Sci. **79/80** (1994) 95.

[21] T. Yonezawa, H. Daimon, K. Nakatsuji, K. Sakamoto and S. Suga, Surf. Sci.**365** (1996) 489.

[22] N. D. Spencer, P. J. Goddard, P. W. Davies, M. Kitson and R. M. Lambert, J. Vac. Sci. Technol. **A1** (1983) 1554.

[23] H. Daimon, Rev. Sci. Instr. **59** (1988) 545; **61** (1990) 205. H. Daimon and S. Ino, J. Vac. Soc. Jpn. **31** (1988) 954. H. Daimon and S. Ino, Rev. Sci. Instr. **61** (1990) 57. H. Daimon and S. Ino, Vacuum **41** (1990) 215.

[24] N. Roberts and R. J. Needs, Surf. Sci.**236** (1990) 112.

[25] L.-Q. Lee and P.-L. Cao, J. Phys.: Condens. Matter **6** (1994) 6169.

[26] H. Lüth, *Surfaces and Interfaces of Solids* (Springer-Verlag, Berlin, 1993) p.440.

[27] K. Sakamoto, T. Okuda, H. Nishimoto, H. Daimon, S. Suga, T. Kinoshita and A. Kakizaki, Phys. Rev.**B50** (1994) 1725, and references therein.

[28] R. Franchy and D. Menzel, Phys. Rev. Lett.**43** (1979) 865.

[29] Q. Guo, D. Sterratt and E. M. Williams, J. Electron Spectrosc. Relat. Phenom. **72** (1995) 31. Q. Guo, D. Sterratt and E. M. Williams, Surf. Sci.**356** (1996) 75.

[30] A. l'Huillier, L. A. Lompre, G. Mainfray and C. Manus, Phys. Rev.**A27** (1983) 2503.

[31] *Photoemission in Solids I*, Springer-Verlag (1978) 145.

[32] J. J. Yeh and I. Lindau, Atomic data and Nuclear data tables **32** (1985) 1.

[33] W. C. Simpson and J. A. Yarmoff, Phys. Rev.**B52** (1995) 2038.

[34] R. Gomer, J. Chem. Phys. **21** (1953) 1869.

[35] R. McGrath, I. T. McGovern, D. R. Warburton, D. Purdie, C. A. Muryn, N. S. Prakash, P. L. Wincott, G. Thornton, D. S-L. Law and D. Norman, Phys. Rev.**B45** (1992) 9327.

Chapter 6

Concluding remarks

In this thesis, three topics on "two-dimensional measurements of electronic and ionic processes on silicon surface" have been discussed. In these topics, the measurement was performed with using a display-type spherical mirror analyzer in order to two-dimensionally obtain the angular distribution of photoelectrons or ions. Significant information obtained in each topics is summarized as follows.

In chapter 3, circular dichroism in angular distribution (CDAD) of the photoelectron from the valence band of Si(001) surface was studied experimentally. The experiment was performed with using circularly-polarized synchrotron radiation at final state energies of 40, 80 and 250eV. All of the obtained photoelectron angular distributions (PEAD) showed apparent CDAD. The PEAD patterns strongly depend on the final state energy, indicating that the photoelectron diffraction effect becomes apparent as the kinetic energy of the photoelectron increases.

At the final state energy of 40eV, the observed PEAD showed a reasonable agreement with the 1D-DOS. Therefore, PEAD can be understood according to its general expression including contributions from one-dimensional density of states (1D-DOS), photoemission structure factor ($|M_C|^2$) and matrix element of the direct transition from initial state atomic orbital to free electron-like final state ($|M_A|^2$). At lower binding energies, the origin of the observed CDAD can be attributed to the interference of the final state waves. That is, in the case of the initial state with the angular momentum l, the final state waves of $l-1$ and $l+1$ interfere without surface effect. Comparing the obtained PEAD with the distribution of $|M_A|^2$, which includes the interference, contributions from the $3p_x$ and $3p_y$ orbitals were distinguished. The calculation by highly accurate one-step model, which completely contains photoelectron diffraction effect, reproduced the experimental results well, with some inconsistency in relative intensity among intense areas. The agreement may be improved by considering the 2×1 reconstruction in the calculation.

In the CDAD pattern at the final state energy of 80eV, significant reflection of 1D-DOS was still observed. The forward focusing effect becomes dominant at the final state energy of 250eV. The origin of CDAD was explained by the rotation of forward focusing peaks,

which is equivalent to those in the case of core level emission, with some contribution from the 1D-DOS.

In chapter 4, surface states on the Si(111)-($\sqrt{3}\times\sqrt{3}$)R30° -Ag surface were investigated. The obtained PEADs showed the mirror symmetry with respect to the $\bar{\Gamma}$ -$\bar{\mathrm{K}}$ line of the $\sqrt{3} \times \sqrt{3}$ surface Brillouin zone, which corresponds to the surface atomic structure of well known honeycomb chained trimer (HCT) model. This suggests that two dimensional PEAD directly gives information about symmetry of the atomic or electronic structure.

The contributions from some surface states were distinguished from the analysis of the intensity profile along high symmetry lines of the observed PEAD taken at various binding energies. Reasonable correspondence with previous report of one-dimensional ARPES was obtained in the derived dispersion, and the existence of some surface states or resonances was confirmed. Comparing the intensity distribution of obtained PEAD with that of $|M_A|^2$ excited by linearly polarized light, we discussed the initial state character of these surface states. One is a metallic surface state, which was revealed to consist of *in plane* Ag $5p$ orbitals. Other surface resonances are suggested to have p_z or s and *in-plane* p character.

These two kinds of studies of two-dimensional PES suggest the effectiveness of two-dimensional measurement as a powerful tool to investigate the electronic structure of semiconductor surface, especially in determination of symmetry of the initial states.

In CDAD study of the valence band photoelectron, a possibility of CDAD measurement as a new way to determine the initial state symmetry was suggested, which is based on a different selection rule in its transition from that in the excitation by linearly polarized light.

In the case of excitation by linearly polarized light, numerous information included in a PEAD enables us to distinguish the character of the surface states as well as their band structure as mentioned in the PEAD study of Ag adsorbed silicon surface.

In chapter 5, the adsorption and desorption processes of Cl on Si(001) and (111) surface was investigated by electron stimulated desorption (ESD) and laser induced ion desorption (LID). The adsorption process studied by the change of work function and AES showed an influence of interaction among the created surface dipoles, especially on (001) surface. The angular distribution of the desorbed ion indicated the adsorption site as previously reported dangling bond and bridge sites on (001) surface.

A preferential desorption of Cl^+ in either ESD or LID via the mechanism described by ASID model was revealed. It includes the excitation of Cl $3s$ and $2p$ core holes and successive intra-atomic Auger decay. The desorption from solid surface initiated by the excitation of core hole is an attractive topic in these days from the point of view of the selective desorption. In the case of LID, the desorption by valence band excitation via double 2-photon process was also suggested.

A strong influence from the potential in the vicinity of the surface was found in the

kinetic energy distribution of desorbed ions. The characteristic coverage dependence observed on both (111) and (001) surfaces was clearly explained by a proposed discrete surface dipole model.

For the future investigation in two-dimensional measurement, an improvement of energy and angular resolution of the display-type analyzer is essential. For example, in the present 2D ARPES measurement, the observed intensity distribution is broadened by energy and angular resolution so that it is hard to obtain the precise band structure directly from PEAD. The improvement of resolution will make it possible to distinguish each band included in PEAD at a glance.

Moreover, although the measurement of time (coverage) dependence on PEAD has not been carried out so far, this is the very superior point compared to the measurement using the other analyzers, so that future works are hopeful.

Acknowledgments

Most of the work in this thesis would not been possible without contributions from many people in various way. I would like to express my sincere gratitude to;

Professor Shigemasa Suga, my principal supervisor, for his advice and useful suggestions to my work, usual encouragement and giving me many chances to have scientific experience.

Professor Hiroshi Daimon as direct mentor, for his usual careful lead and encouragement to my work with his surprising insight and inspiration in surface physics.

All the staff in Suga laboratory;
Dr. S. Imada and Dr. A. Sekiyama for their usual encouragement and useful discussions on physical topics and computer.
Dr. K. S. An for useful discussion on surface science.
Ms. T. Ukawa for her helpful support to my research life.

All the people related to Suga laboratory, graduate and under-graduate students;
Dr. K. Sakamoto, Dr. T. Okuda and Mr. T. Yonezawa for their collaboration, helpful advice and discussion.
Dr. T. Matsushita and Dr. T. Nakatani for their useful programs for data analysis.
Mr. T. Muro, Mr. S. Ueda, Ms. K. Matsuda, Mr. H. Oki, Mr. T. Furuhata, Mr. M. Kotsugi, Mr. H. Takagi and Mr. M. Fujikawa for their cooperation in my work, useful discussion and joyful daily life in the laboratory.

Prof. T. Miyahara, Prof. A. Yagishita and Dr. Y. Kagoshima for arrangement of the experiment at AR NE1B and PF BL28A.
Prof. S. Shin and Prof. Y. Tezuka for arrangement of the experiment at SOR-RING BL4, proper help and encouragement.
Prof. W. Schattke and Dr. C.-H. Soterbeck for their collaboration, fruitful discussion and wonderful calculation on CDAD.
Prof. F. Komori and Dr. K. Hattori for their collaboration in LID experiment, fruitful discussion and encouragement.
Dr. H. Tabata for lending us a portable excimer laser.
Dr. H. W. Yeom for arrangement of the experiment at PF BL7B which was my first work on Ag/Si(111) surface.
Dr. M. Aono, Dr. T. Nakayama and all the researchers in surface and interface laboratory in RIKEN for giving me information on HCT model as well as exciting experiments and life there.

All of my friends for their friendship in daily life.

My parents for their constant sympathy with my course, support and encouragement.

List of publications

1. "Adsoption and desorption processes of Cl on a Si(111)7×7 surface"
   T. Yonezawa, H. Daimon, K. Nakatsuji, K. Sakamoto and S. Suga
   Surf. Sci. **79/80** (1994) 95.

2. "PSD mechanism of Cl^+ ions from Cl/Si(111) surface"
   T. Yonezawa, H. Daimon, K. Nakatsuji, K. Sakamoto, S. Suga, H. Namba and T. Ohta
   Jpn. J. Appl. Phys. **33** (1994) 2248.

3. "Electron stimulated desorption (ESD) of O_2/Si(111) surface"
   K. Sakamoto, K. Nakatsuji, H. Daimon, T. Yonezawa, and S. Suga
   Surf. Sci. **306** (1994) 93.

4. "Electron- and photon-stimulated desorption of the NO/Si(111) surface"
   K. Sakamoto, K. Nakatsuji, H. Daimon, T. Yonezawa, S. Suga, H. Namba and T. Ohta
   Surf. Sci. **359** (1996) 147.

5. "Adsorption and desorption processes of Cl on Si(100) surface"
   K. Nakatsuji, K. Matsuda, T. Yonezawa, H. Daimon, and S. Suga
   Surf. Sci. **363** (1996) 321.

6. "Photon-stimulated desorption study of the NO/Si(111) surface"
   K. Sakamoto, K. Nakatsuji, H. Daimon, T. Yonezawa, S. Suga, H. Namba and T. Ohta
   J. Electron Spectrosc. Relat. Phenom. **80** (1996) 125.

7. "Energy barrier for ion desorption due to discrete surface dipoles"
   T. Yonezawa, H. Daimon, K. Nakatsuji, K. Sakamoto and S. Suga
   Surf. Sci. **365** (1996) 489.

8. "Dichroism in core photoelectron diffraction spectra of Si(001) in dependence on the photon polarization"
   P. Rennert, A. Chasse, T. Nakatani, K. Nakatsuji, H. Daimon and S. Suga
   J. Phys. Soc. Jpn. **66** (2) (1997) 396.

9. "Observation of circular dichroism in angular distribution of the valence band photoelectron from Si(001) in UPS region"
   K. Nakatsuji, H. Daimon, T. Furuhata, H. Takagi, M. Fujikawa, S. Suga, T. Miyahara, A. Yagishita, C.-H. Solterbeck and W. Schattke
   J. Electron Spectrosc. Relat. Phenom., in press.

10. "Fermi surface of Sr_2RuO_4 studied by two-dimensional angle resolved photoelectron spectroscopy"
    T. Okuda, H. Daimon, K. Nakatsuji, M. Kotsugi, M. Fujikawa, S. Suga, Y. Tezuka, S. Shin, M. Kasai and Y. Tokura
    J. Electron Spectrosc. Relat. Phenom., in press.

11. "Two-dimensional angle resolved resonance photoelectron spectroscopy of 1T-TaS_2"
T. Okuda, H. Daimon, K. Nakatsuji, M. Kotsugi, S. Suga, Y. Tezuka, S. Shin, T. Hasegawa and K. Kitazawa
J. Electron Spectrosc. Relat. Phenom., in press.

12. "Symmetry analysis of the Fermi surface of Sr_2RuO_4 by display type photoelectron spectroscopy"
T. Okuda, M. Kotsugi, K. Nakatsuji, M. Fujikawa, S. Suga, H. Daimon, Y. Tezuka, S. Shin, M. Kasai and Y. Tokura
submitted to Phys. Rev. Lett..

13. "Symmetry analysis of the Fermi surface of $Bi_2Sr_2CaCu_2O_8$ by display analyzer"
M. Kotsugi, K. Nakatsuji, T. Okuda, T. Furuhata, M. Fujikawa, H. Takagi, Y. Tezuka, S. Shin, S. Suga, H. Daimon
J. Electron Spectrosc. Relat. Phenom., in press.

Revision of "List of publications"

10. "Fermi surface of Sr_2RuO_4 studied by two-dimensional angle resolved photoelectron spectroscopy"
    T. Okuda, H. Daimon, M. Kotsugi, K. Nakatsuji, M. Fujikawa, S. Suga, Y. Tezuka, S. Shin, M. Kasai and Y. Tokura
    J. Electron Spectrosc. Relat. Phenom. **88-91** (1998) 473.

11. "Two-dimensional angle resolved resonance photoelectron spectroscopy of 1*T*-TaS_2"
    T. Okuda, H. Daimon, K. Nakatsuji, M. Kotsugi, S. Suga, Y. Tezuka, S. Shin, T. Hasegawa and K. Kitazawa
    J. Electron Spectrosc. Relat. Phenom. **88-91** (1998) 287.

12. "Symmetry analysis of the Fermi surface of Sr_2RuO_4 by display type photoelectron spectroscopy"
    T. Okuda, M. Kotsugi, K. Nakatsuji, M. Fujikawa, S. Suga, H. Daimon, Y. Tezuka, S. Shin, M. Kasai and Y. Tokura
    submitted to Phys. Rev..

13. "Symmetry analysis of the Fermi surface of $Bi_2Sr_2CaCu_2O_8$ by display analyzer"
    M. Kotsugi, H. Daimon, K. Nakatsuji, T. Okuda, T. Furuhata, M. Fujikawa, H. Takagi, Y. Tezuka, S. Shin, K. Kitahama, T. Kawai and S. Suga
    J. Electron Spectrosc. Relat. Phenom. **88-91** (1998) 489.